TRABAJO FINAL DE MÁSTER

TÍTULO

THERMO-MECHANICAL ANALYSIS OF THE STABILITY OF A ROCK-CLIFF UNDER CLIMATIC ACTIONS.

AUTOR

DANIEL FELIPE RUIZ RESTREPO

TUTOR

JEAN VAUNAT

ESPECIALIDAD

GEOTECHNICAL ENGINEERING

FECHA

10 JANUARY 2013

Dep. de Ingeniería del Terreno, Cartográfica y Geofísica
E.T.S. Ingenieros de Caminos, Canales y Puertos
UNIVERSIDAD POLITÉCNICA DE CATALUÑA

Departament d'Enginyeria
del Terreny, Cartogràfica i Geofísica
UNIVERSITAT POLITÈCNICA DE CATALUNYA

THERMO-MECHANICAL ANALISYS OF THE STABILITY OF A ROCK-CLIFF UNDER CLIMATIC ACTIONS.

MASTER THESIS

by

DANIEL F. RUIZ RESTREPO

Supervisor:
Dr. JEAN VAUNAT

Barcelona
2013

ABSTRACT

This master thesis deals with the numerical analysis of the response of a rock cliff that presents recurrent instabilities as the results of the effect the climatic actions. Because the cliff is located above an important historic and touristic village, named *La Roque Gageac*, it has been recently instrumented by the French Service of Civil Works in order to detect possible forthcoming failures.

At geological level, the cliff is composed by a calcareous rock created in a marine environment and with a large number of discontinuities families induced by a strong tectonic activity. The cliff studied has an approximated height of 100 meters and as principal characteristic it has a cavern that was used as a refuge during the wars, whereby there is a great interest in evaluate the risk.

After the recent failure that took place in January 2010, a number of studies and field investigations were initiated with the aim to determinate the relationship between the atmospheric actions and the cliff stability. An instrumentation system was installed in the rock massif that allows to determinate the relationship between the main atmospheric actions and the cliff thermal deformations.

In this work, a numerical model has been developed to aid the measurement interpretation and analyze the coupled thermo-mechanical response of the slope under the climatic action. It is based on an adequate theoretical framework to cope with the thermo-hydro-mechanical response of geological media, further enhanced by a special boundary conditions to include mass and energy fluxes between the ground and the atmosphere.

Several numerical simulations of the response of the cliff have been realized to get insights into the cliff stability. They indicate the importance of considering solar radiation to capture the temperatures measured in the massif and the strong relation existing between the temperatures and deformation. They also show that the cliff above the cavity has a reversible behaviour for the period under consideration (July 2010 – June 2011) but that some irreversible deformation occurs at the two vertical discontinuities that bound roof of the cavity.

REFERENCES

Blight, G. E., 1997. Interactions between the atmosphere and the earth. *Géotechniqu*e 47, No. 4, 713-767. 37_{th} Rankine Lecture

Blight, G. E., 2009. Solar heating of the soil and evaporation from a soil surface. *Géotechniqu*e 59, No. 4, 355-363.

Cui, Y. J., Lu, Y. J., Delage, P. & Riffard, M., 2005. Field simulation of in situ water content and temperature change due to ground-atmospheric interactions. *Géotechniqu*e 59, No. 4, 355-363.

Cui, Y. J. & Zornberg, J. G. Y. J., 2008. Water balance and evapotranspiration monitoring in geotechnical and geoenvironmental engineering. *Geotechnical and Gelogical Engineering*, Vol 26, Issues 6. 4, 783-798.

Gens A., Carol I. & Alonso E.E.1990. A constitutive model for rock joints; formulation and numerical implementation. *Computers and Geotechnics*, 9:3–20.

Gens, A., Vaunat, J., Garitte, B. & Wileveau, Y. 2007. In situ behaviour of a stiff layered clay subject to thermal loading: observations and interpretation. *Géotechnique* 57, No. 2, 207–228

Hoek, E. & Brown, T. 1980. Empirical strength criterion for rock masses. *Journal of the Geotechnical Engineering Division*, Vol. 106, No. 9. 1013-1035.

Hoek, E. & Brown, T. 1997. Practical estimates or rock mass strength. *Int. J. Rock Mech. & Mining Sci. & Geomechanics Abstracts. 34 (8), 1165–1186.*

Hudson, J. & Harrison, J. 1997. Engineering Rock Mechanics. *Elsevier Ltd.*

Laboratoire Régional des Ponts et Chaussées de Toulouse., 2011. La Roque Gageac - Endommagement de la roche sous l'effet des cycles thermiques. *Report Project DOSMS*

Laboratoire Régional des Ponts et Chaussées de Toulouse., 2011. La Roque Gageac – Note Technique Système d'Instrumentation. *Report Project DOSMS*

Noilhan, J., & Planton, S., 1988. A simple parameterization of land surface processes for metereological models. *Monthly Weather Review*, Vol 117, 536-589.

Olivella, S., Carrera, J., Gens A. & Alonso, E.E. 1994. Non-isothermal Multiphase Flow of Brine and Gas through Saline media. *Transport in Porous Media*, 15: 271-293.

Olivella, S; Gens, A; Carrera, J; Alonso, E. (1996). *Numerical Formulation for a Simulator (CODE_BRIGHT) for The Coupled Analysis of Saline Media*. Engineering Computations, Vol. 13, No 7, pp. 87-112.

Pineda, J., Romero, E., Gómez, S., Alonso, E. 2011. Degradation effects at microstructural scale and their consequences on macroscopic behaviour of a slightly weathered silstone. *Geomechanics and Geotechnics, From Micro to Macro – Jiang et al. (eds)*, 73-78.

Ruiz, D., Vaunat, J., Samat, S. & Virely, D. 2012. Thermo-mechanical modelling of an aerial cavern under climatic actions. *4_{th} Workshop CODE_BRIGHT*, Barcelona.

Saaltink, M., Pereira, J.M. & Samat, S. 2012.. Atmospheric Boundary Conditions Module in *CODE_BRIGHT.*

Sofianos, A. 1996. Analysis and desing of an underground hard rock voussoir beam roof. *Int. J. Rock Mech. & Mining Sci. & Geomechanics Abstracts. 33 (2), 153–166.*

Vaunat, J., Samat, S., Alonso, E., Ruiz, D., Martin, E., Saillard, M., Virely, D. & Darrozes, J. 2012. Slope responses under climatic actions. Model and case interpretation. *In preparation*.

Zandarin, M. T. 2010. Thermo-Hydro-Mechanical analysis of joints-A theoretical and experimental study. *PhD Thesis, Universitat Politècnica de Cataluna.*

RESUMEN

Este trabajo final de master aborda el análisis numérico de la respuesta de un acantilado que presenta recurrentes inestabilidades como resultado de las acciones climáticas. Debido a que el acantilado está localizado por encima de un importante lugar histórico y turístico, llamado *La Roque Gageac*, se ha instalado recientemente un sistema de instrumentación con el fin de detectar próximas inestabilidades.

A nivel geológico el acantilado está compuesto una roca calcárea formada en un ambiente marino y con un gran número de familia de discontinuidades provenientes de una actividad tectónica fuerte. El acantilado estudiado presenta una altura aproximada de 100 metros y como característica principal presenta una caverna que sirvió en tiempos pasados como refugio de guerras, por lo que existe un gran interés de evaluar el riesgo.

Después del fallo que tuvo lugar en Enero de 2010, una serie de estudios e investigaciones de campo fueron iniciadas con el objetivo de determinar la relación entre las acciones atmosféricas y la estabilidad del acantilado. Un sistema de instrumentación fue instalado en el macizo, el cual permite determinar la relación entre las principales acciones atmosféricas y loas deformaciones térmicas del macizo.

El reto de este trabajo investigativo es encontrar un marco conceptual adecuado para el análisis del problema, por medio del cual se puedan evaluar los principales factores que intervienen en el problema. La modelación Termo-Hidro-Mecánica en medios porosos y la modelación de los fenómenos atmosféricos como condiciones de contorno en problemas numéricos fueron usados para este trabajo.

In este trabajo se ha desarrollado un modelo numérico con el fin de facilitar la interpretación de la instrumentación y analizar la respuesta termo-mecánica de la ladera bajo las acciones climáticas. Dicho modelo está basado en un marco conceptual adecuado, el cual contempla la respuesta Termo-Hidro-Mecánica de materiales geológicos; además de contemplar unas condiciones de frontera especial que tiene en cuenta los flujos de masa y energía entre el suelo y la atmosfera.

Fueron desarrolladas varias modelaciones numéricas para tratar de evaluar la estabilidad del acantilado, obteniendo como resultado que la radiación solar debe de ser considerada para capturar las medidas de temperaturas en el macizo de roca y estudiar la marcada relación entre las temperaturas y la deformación. Igualmente, fue observado que la parte del acantilado por encima de la caverna presenta un comportamiento reversible en el periodo modelado (Julio 2010 – Junio 2011), pero deformaciones irreversibles ocurren en las dos discontinuidades verticales que limitan el techo de la misma.

ACKNOWNLEDGMENTS

I would like to express my sincere gratitude to my supervisor Professor Jean Vaunat, for his valuable guidance, for trusting in my abilities and my work, for his patience and academic support during my Master Science in Geotechnical Engineering at the Department of Geotechnical Engineering and Geosciences of the Universitat Politècnica de Catalunya (UPC).

I am grateful to the Professors at Department of Geotechnical Engineering and Geosciences of the Universitat Politècnica de Catalunya (UPC) for convey their knowledge and experience in geotechnical engineering.

I am gratefully with Didier Virely (GERM-Géotechnique, Enviroment, Risques naturels, Mécanique des sols et des roches) for propose this interesting case study and to provide all field data, also I acknowledge the support of the European Commission through the project SUDOE DO_SMS.

Undoubtedly, I want to express my gratitude to Sergio Samat and Nubia Gonzales, for his dedication and important explanations of numerical issues and the interactions between the ground and the atmosphere.

Finally, I am especially grateful to my family and Claudia for their continuous support, patience and encouragement during this time.

NOTATION

a	Opening of the element
A_d	Dry albedo
A_w	Wet albedo
A_l	Albedo
a_{min}	Minimum opening of the element
b_s	Linear thermal expansion coefficient for the medium
C_a	Specific heat of the gas
D	Disturbance factor
$d\varepsilon_{kl}^{M}$	The strains corresponding to the clay matrix deformation
$d\varepsilon_{kl}^{P}$	Plastic strains of the clay matrix
d_a	Duration of the year
$\frac{De}{Dt}$	Material derivate of energy
d_d	Duration of a day (86400 s)
D_{ijkl}^{eM}	Mechanical elastic stiffness matrix of the clay
d_s	Time span between sunrise and sunset
E	Evaporation
E(Gpa)	Yong´s modulus
f_e	Source/skin term of energy
g	Gravidity
GSI	Geological strength index
G^p	Plastic potential
H_c	Convective or latent heat flux
h_{la}	Free energy of water
h_{a0}	Free energy of air
H_s	Sensible heat flux
h_v	Free energy of vapour

i_c	Conductivity heat
I_n	Cloud index
j_a	Flux of air
j_e	Total energy flux
J^M	Second invariant deviatory stress tensor
j_w^g	Flux of water, gas phase
j_w^l	Flux of water, liquid phase
$k^{é}$	Von Karman´s constant
K_{MT}	Coefficient setting the decrease of uniaxial compressive strength with temperature
K_n	Normal stiffness
K_s	Tangential stiffness
K_s^M	Bulk modulus against suction changes
F^p	Yield function
m	Parameter of the model
m^M	Parameter that defines the shape of the parabolic yield criterion
P	Rainfall
P^M	First invariant stress tensor
P_t^M	Tensile strength
R_a	Long wave atmospheric radiation
R_A	Daily solar radiation in absence of atmosphere
R_c^M	Uniaxial compressive strength
R_{c0}^M	Intact strength
R_g	Direct solar short wave radiation
R_G	Daily solar radiation
r^M	Coefficient setting the change in cohesion with suction
R_n	Solar radiation
r_s	Relation between the average distance between the earth and the sun for a given moment

s	Suction
S_l	Liquid saturation
S_0	Solar constant
t	Current time
T	Temperature
T_a	Atmospheric temperature
t_m	Time at noon
t_0	The time of January first
t_s	The time when autumn starts
T_{ref}	Reference temperature
U_n	Normal displacement of the joint
U_s	Tangential displacement of the joint
v_a	Wind velocity
z_0	Roughness length
z_a	Screen height at which v_a and ρ_{va} are measured

Greek symbols

α^M	Brittleness parameter
β^M	Coefficient setting the change in cohesion with suction
δ	The declination of the sun
δ_{kl}	Kronecker delta
δ_{max}	Maximum declination of the sun
ε	Emissivity
ε_1^{pM}	Mayor principal plastic strain
ε_r^M	Accumulated major principal plastic strain at which the residual strenght is reached
ε_v	Linear expansion induced by temperature and suction changes
θ^M	Lode´s angle
λ	Thermal conductivity
λ_l	Latitude

ρ	Density
ρ_{ga}	Atmospheric gas pressure
ρ_{va}	Absolute humidity of the atmosphere
σ	Tensions tensor
σ'	Normal effective stress
σ_{ij}^{M}	Stresses prevailing at clay particles contact
σ_s	Stefan-Boltzman constant
σ_c	Uniaxial compression stress
τ	Tangential stress
ϕ	Stability factor

TABLE OF CONTENTS

ABSTRACT i

REFERENCES i

RESUMEN iv

ACKNOWNLEDGMENTS v

NOTATION vi

TABLE OF CONTENTS x

LIST OF FIGURES xii

LIST OF TABLES xvii

CHAPTER 1 - INTRODUCTION ..... - 1 -

1.1 REFERENCES ..... - 2 -

CHAPTER 2 – CASE DESCRIPTION: *LA ROQUE GAGEAC* ..... - 4 -

2.1 INTRODUCTION ..... - 4 -
2.2 SITE LOCATION ..... - 4 -
2.3 GEOLOGICAL CONTEXT ..... - 6 -
2.4 HISTORICAL ROCKFALLS AND CURRENT RISK ..... - 7 -
2.4.1 Historical Rockfalls ..... - 8 -
2.4.2 Current Risk ..... - 10 -
2.5 RELATION BETWEEN ROCK-CLIFF BEHAVIOUR AND CLIMATIC ACTIONS ..... - 14 -
2.5.1Climate ..... - 14 -
2.6 REFERENCES ..... - 14 -

CHAPTER 3 – FIELD INSTRUMENTATION AND LABORATORY TESTING ..... - 15 -

3.1 FIELD INSTRUMENTATION ..... - 15 -
3.1.1 Instrumentation lay-out ..... - 15 -
3.1.2 Basic interpretation of measurements ..... - 18 -
3.2 LABORATORY TESTING ..... - 31 -
3.3 REFERENCES ..... - 35 -

CHAPTER 4 – CONCEPTUAL FRAMEWORK OF ANALYSIS ..... - 37 -

4.1 MODELLING CLIMATIC ACTIONS ..... - 38 -

4.1.1 Total Energy Flux ..... - 40 -
4.2 THERMO-HYDRO-MECHANICAL COUPLING IN SOILS AND ROCKS ..... - 44 -
4.3 REFERENCES ..... - 49 -

CHAPTER 5 – NUMERICAL ANALYSIS ..... - 50 -

5.1 NUMERICAL MODELS ..... - 51 -
5.1.1 Elastic model 2D with net radiation flux ..... - 51 -
5.1.2 Elastic model 2D without net radiation flux ..... - 63 -
5.1.3 Elastoplastic model 2D (Hoek-Brown) with net radiation flux ..... - 66 -
5.1.4 Elastic model 3D with net radiation flux ..... - 74 -
5.1.5 Roof of the cavern model (Residual Beam) ..... - 80 -
5.2 REFERENCES ..... - 86 -

CHAPTER 6 – CONCLUSIONS AND FUTURE WOKS ..... - 87 -

6.1 CONCLUDING REMARKS ..... - 87 -
6.2 FUTURE DEVELOPMENTS ..... - 88 -

LIST OF FIGURES

CHAPTER 2

Figure 2-1. Location of La Roque Gageac; a) Location of Dordogne department in France; b) Location of La Roque Gageac in Dordogne department. - 4 -
Figure 2-2. Orthophotograph of the site under study - 5 -
Figure 2-3. Site under study; a) Rock-cliff above the village; b) Aerial troglodyte cavern - 5 -
Figure 2-4. Geological scheme Sarlat-La-Cadena. - 6 -
Figure 2-5. Example of hydraulic deposits with different shapes. - 7 -
Figure 2-6. Rockfall in 1920 - 8 -
Figure 2-7. Rockfall in January 1957 - 8 -
Figure 2-8. Rockfall in January 2010; a) Residual rock beam and damage within the cavern; b) Location of the Rockfall in the aerial troglodyte cavern - 9 -
Figure 2-9. General location of the instability events. *Technical Report, 2011*. - 9 -
Figure 2-10. Flaking on the surface rock-cliff - 10 -
Figure 2-11. Small block from rock-cliff surface - 11 -
Figure 2-12. Mesh for smalls to medium rockfalls - 11 -
Figure 2-13. Main families of discontinuities - 12 -
Figure 2-14. Residual rock beam within the troglodyte cavern - 13 -
Figure 2-15. Open fracture limiting with the rock beam - 13 -
Figure 2-16. Open fractures and decompressed zones of another cliff near to site of study. - 13 -

CHAPTER 3

Figure 3-1. Data of the Meteorological station Sarlat_La Canéda - 16 -
Figure 3-2. Comparison between temperatures registered at the meteorological station and measured within the cavern. - 16 -
Figure 3-3. Localization of the instrumentation system. - 17 -
Figure 3-4. Cross section through troglodyte cavern. Measurements in meters - 18 -
Figure 3-5. Time evolution of temperature _ Distometer D1 - 19 -
Figure 3-6. Time evolution of temperature _ Distometer D2 - 19 -
Figure 3-7. Time evolution of displacement _ Distometer D1; a) Displacement at 2m, 4m and 6m; b) Relationship Temperature-Displacement - 20 -
Figure 3-8. Time evolution of displacement _ Distometer D2; a) Displacement at 2m, 4m and 6m; b) Relationship Temperature-Displacement - 21 -

Figure 3-9. Time evolution of Strain _ Distometer D1 ..... - 22 -
Figure 3-10. Time evolution of Strain _ Distometer D2 ..... - 22 -
Figure 3-11. Discontinuity plane across distometers site; a) Location of the plain discontinuity; b) Cross section through troglodyte cavern ..... - 23 -
Figure 3-12. Time evolution of displacement _ Jointmeters J1, J2, J3; J4 and J5; a) Time evolution of displacement; b) Relation Temperature-Displacement ..... - 24 -
Figure 3-13. Mechanism of discontinuities against low temperature values; a) Horizontal discontinuity; b) Vertical diaclases ..... - 25 -
Figure 3-14. Different orientation of the Jointmeter J-1; a) July 2010 to December 2010; b) December 2010 until the present time ..... - 26 -
Figure 3-15. Time evolution of displacement _ Jointmeters J-1 and J-2 ..... - 26 -
Figure 3-16. Irreversible displacement Jointmeter J-1 ..... - 27 -
Figure 3-17. Irreversible displacement Jointmeter J-2 ..... - 27 -
Figure 3-18. Movement of the beam against low temperature ..... - 28 -
Figure 3-19. Displacement components Jointmeter J-2 ..... - 28 -
Figure 3-20. Displacement comparison between distometers and jointmeters; a) Jointmeters vs Distometer D1; b) Jointmeters vs Distometer D2 ..... - 29 -
Figure 3-21. Convergence Measurements; a) Superficial spots located on one vertical line at top of the cavern; b) Within the cavern ..... - 30 -
Figure 3-22. Displacements of Decompressed Zone; a) Comparison with Jointmeters and Distometer D1; b) Comparison with Jointmeters and Distometer D2 ..... - 30 -
Figure 3-23. Deformations of the cavern against thermic cycles; a) High temperatures; b) Low temperatures ..... - 31 -
Figure 3-24. Uniaxial compression test. ..... - 32 -
Figure 3-25. Brazilian tensile strength test. ..... - 32 -
Figure 3-26. Brittle – ductile behavior of the rock. ..... - 33 -
Figure 3-27. Tensile strength variation as a function of specimen volume and type of test. Hudson & Harrison 1997. ..... - 34 -
Figure 3-28. Normalized failure Envelope for Sandstone. Hoek & Brown 1980 ..... - 34 -

CHAPTER 4

Figure 4-1. Scheme of mass and energy interactions between ground, vegetation and atmosphere. Blight 1997 ..... - 37 -
Figure 4-2. Components of the radiation balance at a soil surface; a) Incoming and outgoing radiation; b) Radiation interchange during the day; c) Radiation interchange at night day. Blight 1997 ..... - 40 -

Figure 4-3. Apparatus for automatic measurements and logging of energy balance components . Blight 1997 ..... - 41 -
Figure 4-4. External temperature and solar radiation measurements at Boissy-le-Châtel, France, during April 1999. Cui *et al.* 2005 ..... - 43 -
Figure 4-5. External temperature and solar radiation measurements at Boissy-le-Châtel, France, during 2003. Cui *et al.* 2008 ..... - 43 -
Figure 4-6. Net radiation in *La Roque Gageac* computed from meteorological data of Sarlat-La Canéda ..... - 44 -
Figure 4-7. Overall THM coupling in soils and rocks (secondary couplings are in italic). ..... - 47 -

CHAPTER 5

Figure 5-1. Elastic two dimensional model; a) Dimensions and mesh; b) Boundary and initial conditions ..... - 52 -
Figure 5-2. Dimensions of troglodyte cavern and output points of the model. ..... - 52 -
Figure 5-3. Collated worldwide in situ stress data: mean horizontal stress component (After Hoek & Brown, 1980). Reported by Hudson & Harrison ..... - 53 -
Figure 5-4. Temperature calculated in thirty thermal cycles (30 years); a) Distometer D1 at 6m; b) Distometer D1 at 2m; c) Distometer D2 at 6m; d) Distometer D2 at 2m. ..... - 55 -
Figure 5-5. Temperatures at distometer D1 - Elastic model 2D with net radiation flux; a) 6 meters into the rock; b) 2 meters into the rock ..... - 56 -
Figure 5-6. Temperatures at distometer D2 - Elastic model 2D with net radiation flux; a) 6 meters into the rock; b) 2 meters into the rock ..... - 57 -
Figure 5-7. Graphical result of temperature - Elastic model 2D with net radiation flux ..... - 58 -
Figure 5-8. Displacement calculated in thirty thermal cycles (30 years); a) Distometer D1 at 6m; b) Distometer D1 at 2m; c) Distometer D2 at 6m; d) Distometer D2 at 2m. ..... - 60 -
Figure 5-9. Displacements at distometer D1 - Elastic model 2D with net radiation flux; a) 6 meters into the rock; b) 4 meters into the rock; c) 2 meters into the rock. ..... - 61 -
Figure 5-10. Displacements at distometer D2 - Elastic model 2D with net radiation flux; a) 6 meters into the rock; b) 4 meters into the rock; c) 2 meters into the rock. ..... - 62 -
Figure 5-11. Measuring points at decompressed zone ..... - 62 -
Figure 5-12. Displacements at decompressed zone - Elastic model 2D with net radiation flux ..... - 63 -
Figure 5-13. Elastic two dimensional model without radiation flux - Boundary and initial conditions . - 63 -
Figure 5-14. Temperatures at distometer D1- Elastic model 2D with net radiation flux vs Elastic model 2D without net radiation flux ; a) 6 meters into the rock; b) 2 meters into the rock. ..... - 64 -

Figure 5-15. Temperatures at distometer D2- Elastic model 2D with net radiation flux vs Elastic model 2D without net radiation flux ; a) 6 meters into the rock; b) 2 meters into the rock. ..... - 65 -
Figure 5-16. Graphical result of temperature - Elastic model 2D without net radiation flux ..... - 66 -
Figure 5-17. Mesh of the elastoplastic two dimensional model ..... - 67 -
Figure 5-18. Temperatures at distometer D1 - Elastoplastic model 2D with net radiation flux; a) 6 meters into the rock; b) 2 meters into the rock. ..... - 68 -
Figure 5-19. Temperatures at distometer D2 - Elastoplastic model 2D with net radiation flux; a) 6 meters into the rock; b) 2 meters into the rock ..... - 69 -
Figure 5-20. Displacements at distometer D1 - Elastoplastic model 2D with net radiation flux; a) 4 meters into the rock; b) 2 meters into the rock ..... - 69 -
Figure 5-21. Displacements at distometer D2 - Elastoplastic model 2D with net radiation flux; a) 4 meters into the rock; b) 2 meters into the rock ..... - 70 -
Figure 5-22. Plastic Multiplier - Elastoplastic model 2D with net radiation flux; a) case *La Roque Gageac*; b) Finite Element model with high discretization; c) Finite Element model with low discretization ..... - 71 -
Figure 5-23. Plastic Multiplier along the sections ..... - 71 -
Figure 5-24. Graphical result of Invariant J - Elastoplastic model 2D ..... - 72 -
Figure 5-25. Invariant J calculated in stationary thermal cycles; a) Distometer D1 at surface; b) Distometer D1 at 2m; c) Distometer D2 at 6m; d) Distometer D2 at 6m. ..... - 73 -
Figure 5-26. Real shape of the troglodyte cavern. ..... - 74 -
Figure 5-27. Mesh of elastic model 3D. ..... - 75 -
Figure 5-28. Temperatures at distometer D1- Elastic model 3D vs Elastic model 2D; a) 6 meters into the rock; b) 2 meters into the rock ..... - 76 -
Figure 5-29. Temperatures at distometer D2- Elastic model 3D vs Elastic model 2D; a) 6 meters into the rock; b) 2 meters into the rock ..... - 76 -
Figure 5-30. Graphical result of temperature - Elastic model 3D with net radiation flux ..... - 77 -
Figure 5-31. Displacements at distometer D1- Elastic model 3D vs Elastic model 2D; a) 6 meters into the rock; b) 2 meters into the rock ..... - 78 -
Figure 5-32. Displacements at distometer D1- Elastic model 3D vs Elastic model 2D; a) 6 meters into the rock; b) 2 meters into the rock ..... - 78 -
Figure 5-33. Location of the sections a, b, c and d ..... - 79 -
Figure 5-34. Vertical stress (Syy) at sections a, b, c and d. ..... - 79 -
Figure 5-35. Shear stress (Syz) at sections a, b, c and d. ..... - 79 -
Figure 5-36. Elastic constitutive law of the joint element. Normal stiffness depends on joint opening. Zandarin 2010 ..... - 81 -
Figure 5-37. Elastic constitutive law. Normal stress vs. aperture for first loading, unloading and reloading respectively (Gens et al., 1990). ..... - 81 -

Figure 5-38. Horizontal joint at the roof of the cavern ..... - 82 -
Figure 5-39. Residual beam arrangement..... - 82 -
Figure 5-40. Finite element model of roof of the cavern; a) Geometry and joint elements modelled; b) Boundary and initial conditions ..... - 82 -
Figure 5-41. Temperature imposed at upper and lower limits of the model ..... - 83 -
Figure 5-42. Graphical result of temperature - Elastic model of the roof ..... - 84 -
Figure 5-43. Apertures computed in joints; a) Jointmeter J-1; b) Jointmeter J-2; c) Jointmeter J-3. - 85 -
Figure 5-44. Normal stress computed; a) Jointmeter J-1; b) Jointmeter J-2 ..... - 86 -

LIST OF TABLES

CHAPTER 2

Table 2-1. Main instability events in *La Roque Gageac . Technical Report, 2011*. ..... - 8 -

CHAPTER 3

Table 3-1. Results of test. ..... - 33 -
Table 3-2. RMR qualification..... - 35 -

CHAPTER 4

Table 4-1. Parameters to Net Radiation Computation..... - 44 -
Table 4-2 . Heat fluxes in unsaturated soils or rocks..... - 46 -
Table 4-3 . Parameters THM dependencies (secondary couplings). ..... - 47 -

CHAPTER 5

Table 5-1 . Parameters of the elastic model ..... - 53 -
Table 5-2 . Parameters of the elastoplastic model..... - 67 -
Table 5-3 . Parameters of the elastic model of the roof..... - 83 -

CHAPTER 1

INTRODUCTION

Interactions between the atmosphere and the ground have always been an important issue in civil and geotechnical engineering. It plays particularly a central role in the analysis of the natural risk associated to landslides, where, since a long time, precipitations have been recognized as one of the main triggering factors, together with other phenomena like erosion and seism. Nevertheless, despite the early recognition of the key effect of climatic actions, there exist still now relatively little cases where direct relationships could be established between occurrence and features of landslides and climate local characteristics (intensity, duration, frequency and spectrum history of rain, temperature, radiation, relative humidity and wind). Soil-atmosphere interaction is indeed a complex phenomenon that involves many coupling whose relative importance depends on the type of problem. As pointed by Blight (1997), depending on the preponderant couplings and their controlling factors, the soil-atmosphere interactions can lead to rapid and catastrophic events while, in other case, their effects may be slow and insidious, but still destructive and costly in the long term.

From the 80's, climate modellers have paid special attention to the coupled process taking place between the ground surface and the atmosphere. For instance, Noilhan & Planton (1988) reported several experimental works to analyze the mass and energy flux taking place between the ground and the atmosphere at large-scale. The merits of these works was to evidence the important interdependence between climate and ground surface processes and to allow for an exploration of the mechanisms involved, but they did not provide realistic insights into the relationships existing between ground characteristics and their effect on climatic changes.

One of the first parameterization of land surface processes for meteorological models was proposed by Noilhan & Planton (1988) who used parameters related, on the one hand, to classification systems for soil texture and vegetation and, on the other hand, to soil and vegetation physical characteristics. Maybe their more important contribution relies on the formulation of mass and energy exchange fluxes between the ground and the atmosphere as well as storage laws for soil heat and water contents, further considered in geotechnical problems by authors like Blight (1997), Blight (2009), Cui et al (2005), Cui et al, (2009). The surfaces fluxes have given further been implemented as specific boundary conditions in numerical codes to model the coupled processes of evaporation, rainfall, radiation and heat together in geomaterials. In this work, the modelling work has been realized using the coupled thermo-hydro-mechanical

Finite Element code CODE_BRIGHT (Olivella et al., 1994) where a special boundary condition has been implemented to simulate the interaction ground-atmosphere.

This thesis presents an instrumented cliff that contains a troglodyte cavity with roof stability problems. The analysis aims at understanding the mechanisms responsible of the current deformation of the cliff and its effect on cavity roof stability. As the rock is considered dry, deformations are essentially due to the thermal load caused by solar radiation and changes in air temperature. This case is used to validate, by comparison with field data, the equations for radiation and thermo-mechanical coupling, as well as to provide insights into the stability of fractured rock exposed to the atmosphere (Ruiz *et al*., 2012; Vaunat *et al* 2012).

The document presented here is developed along main five chapters. Chapter 2 deals with the site location, geological history and description of the case; Chapter 3 shows the field instrumentation system installed, the analyze of the field data and its relationship with the climatic changes and some laboratory test done; Chapter 4 presents the conceptual framework of analysis with a coupling Thermo-Hydro-Mechanical phenomena; Chapter 5 contains the results of the numerical analysis through the CODE_BRIGHT and finally the conclusion, summary and future works are in the Chapter 6.

1.1 REFERENCES

Blight, G. E., 1997. Interactions between the atmosphere and the earth. *Géotechniqu*e 47, No. 4, 713-767. 37_{th} Rankine Lecture

Blight, G. E., 2009. Solar heating of the soil and evaporation from a soil surface. *Géotechniqu*e 59, No. 4, 355-363.

Cui, Y. J., Lu, Y. J., Delage, P. & Riffard, M., 2005. Field simulation of in situ water content and temperature change due to ground-atmospheric interactions. *Géotechniqu*e 59, No. 4, 355-363.

Cui, Y. J. & Zornberg, J. G. Y. J., 2008. Water balance and evapotranspiration monitoring in geotechnical and geoenvironmental engineering. *Geotechnical and Gelogical Engineering*, Vol 26, Issues 6. 4, 783-798.

Noilhan, J., & Planton, S., 1988. A simple parameterization of land surface processes for metereological models. *Monthly Weather Review*, Vol 117, 536-589.

Olivella, S., Carrera, J., Gens A. & Alonso, E.E. 1994. Non-isothermal Multiphase Flow of Brine and Gas through Saline media. *Transport in Porous Media*, 15: 271-293.

Ruiz, D., Vaunat, J., Samat, S. & Virely, D. 2012. Thermo-mechanical modelling of an aerial cavern under climatic actions. *4_{th} Workshop CODE_BRIGHT*, Barcelona.

Vaunat, J., Samat, S., Alonso, E., Ruiz, D., Martin, E., Saillard, M., Virely, D. & Darrozes, J. 2012. Slope responses under climatic actions. Model and case interpretation. *In preparation*.

CHAPTER 2

CASE DESCRIPTION: *LA ROQUE GAGEAC*

2.1 INTRODUCTION

The site under study consists of an instrumented rock cliff, seat of natural recurrent block falls that endangered a touristic village located at its toe. This case provides an interesting opportunity to analyze the effect of climatic actions on the response of a dry rock over several years. The objective of this chapter is to present the characteristics of the problem: cliff geometry, including the presence of an aerial cavern with unstable roof, pattern of rock discontinuities, past hazard and current risk. All the information described comes from the technical report edited by the *Laboratoire Régional des Ponts et Chaussées de Toulouse* (2011) and the field observations taken during the scientific visit made by the staff of the *Technical University of Catalonia* (UPC) in March 2011. This information is completed in Chapter 3 with the description of the field instrumentation installed by the *Laboratoire Régional des Ponts et Chaussées de Toulouse* and the laboratory tests realized in the same institution.

2.2 SITE LOCATION

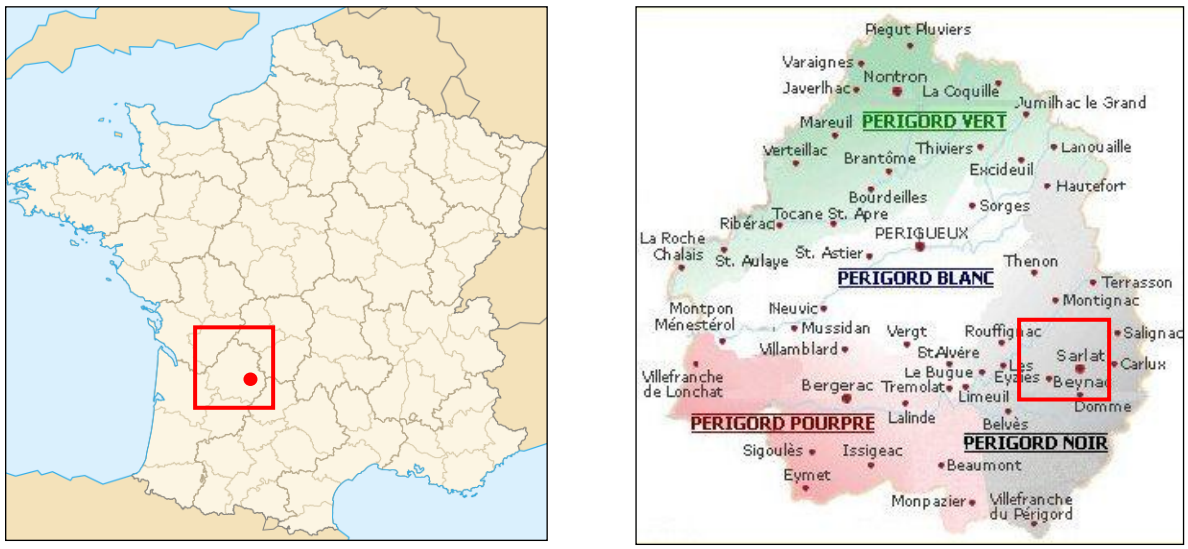

(a) **(b)**

Figure 2-1. Location of La Roque Gageac; a) Location of Dordogne department in France; b) Location of La Roque Gageac in Dordogne department.

The French locality *La Roque Gageac* is located close to *Sarlat* town (10 kilometers far) at te north-east of Aquitaine Basin in the Dordogne department (Figure 2-1). Although this locality has only 416 people, the tourism is the most important economic activity with 2 million visitors per year, because this is listed as one of most beautiful village of France.

The village is located at the toe of a calcareous rock-cliff of Cretaceous age, on the left bank of Dordogne River (Figure 2-2). The rock-cliff culminates at a height of about 100 m above the village and it is prone to block falls. At a height of 50m above an old village fortification, the cliff contains a troglodyte cavern, used as refuge during the Hundred Year's war and now recognized as a touristic site (Figure 2-3).

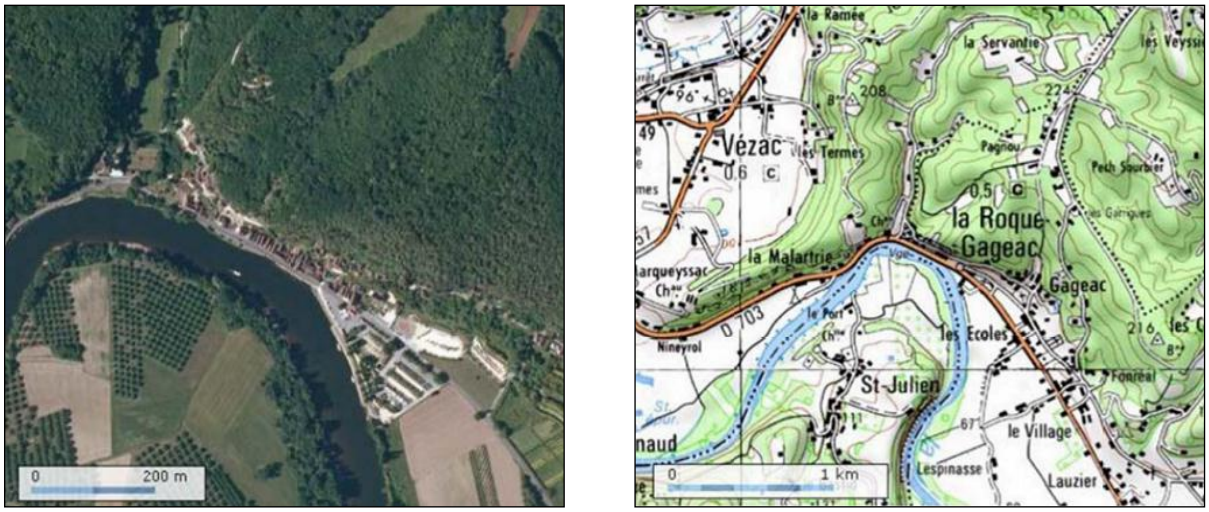

Figure 2-2. Orthophotograph of the site under study

(a) **(b)**

Figure 2-3. Site under study; a) Rock-cliff above the village; b) Aerial troglodyte cavern

Because part of the roof of the troglodyte cavern failed during winter 2010, resting support to the upper block rock, a detailed geological and geotechnical survey has been conducted to analyze the causes of the failure (i.e. strength, discontinuities pattern, interaction with the atmosphere, etc.) and its possible effect on the cliff upper part stability.

2.3 GEOLOGICAL CONTEXT

The Dordogne area is made by to deep valleys (up to 500 meter depth) generated by an important fluvial system. This system has created a morphology marked by the succesion of broad areas with numerous meanders and narrow areas with straight rivers sections.

This fluvial system crosses different geological formations: argillaceous rocks, marls, sandstones, etc. The formation at *La Roque Gageac* is a calcareous sandstone formed during the intermediate and upper Coniacien (65 Million-Years) in a marine environment (Figure 2-4).

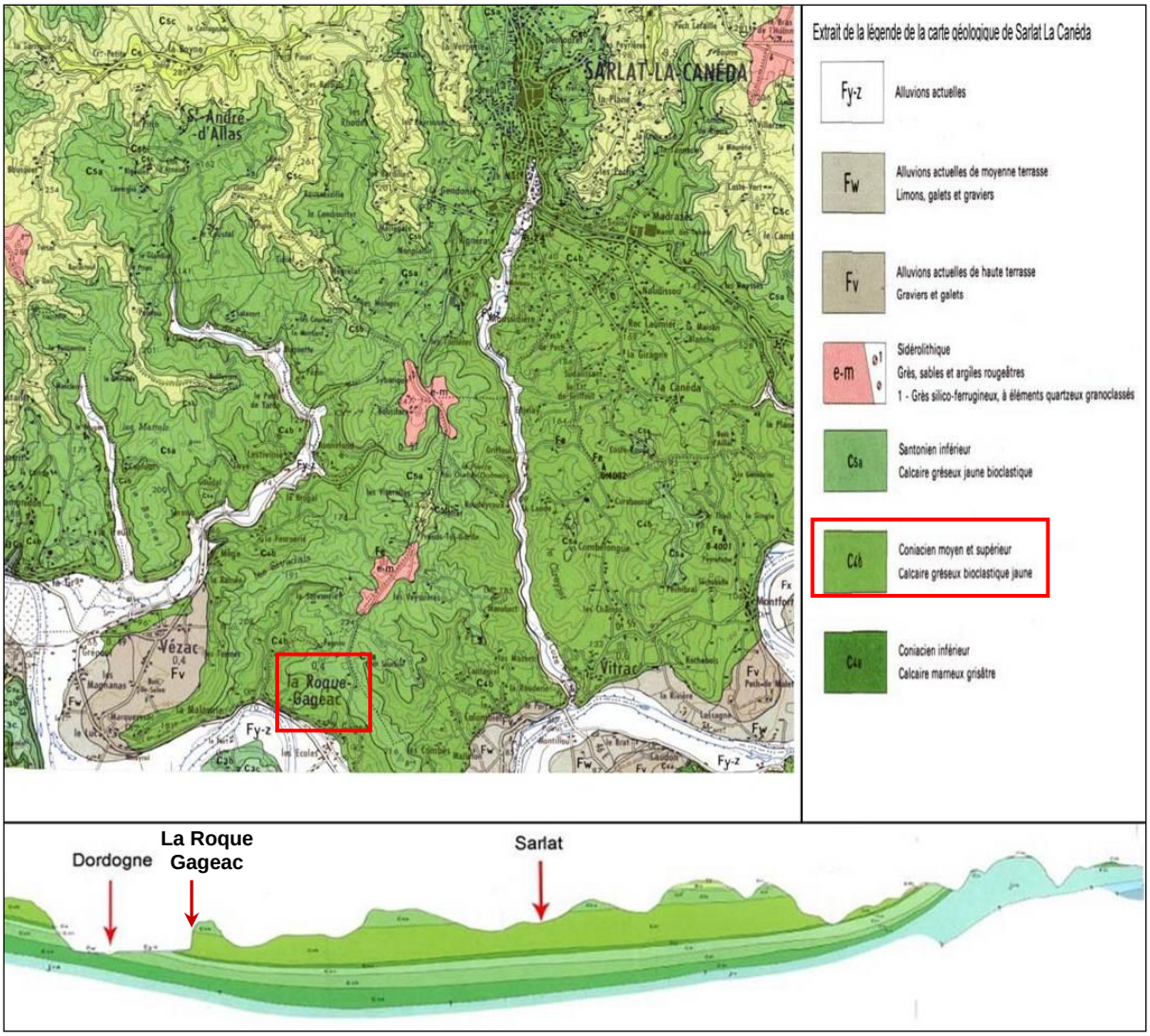

Figure 2-4. Geological scheme Sarlat-La-Cadena.

As a result of its calcareous nature, the geological formation (Upper Coniacien) is affected by karst phenomena, causing local decompression zones. The facies observed at *La Roque Gageac* and the paleo-poljé (geological hole) located in the meander of Saint Julie, close to site under study, are evidences of such an intense karstification.

80% of karst cavities are located in the permeable formation (Upper Coniacen) culminating above *La Roche Gageac* while the lower part of the cliff, made of a more impermeable formation (Lower Coniacen), does not present significant karstification. The aerial troglodyte cavern has been classified as a part of an inactive network of paleo-karts, however some still active networks (i.e. streams) can be detected in the calcareous formation at the bottom of the cliff just above of the village. These active and inactive networks of karstification are considered to be the main factors for rock structure weakening and cliff instability.

Another important factor of rock mechanical behaviour is the presence of bedding planes, whose pattern is controlled by ocean past currents. Alternative erosion and deposition processes have generated sedimentary structures characterized by layers with different orientations and inclinations (Figure 2-5).

As the result of this geological history, the rock is characterized by poor structural characteristics due to:
1) a strong material heterogeneity due to numerous facies lateral variations and
2) low mechanical characteristic due to the presence of different families of discontinuities.

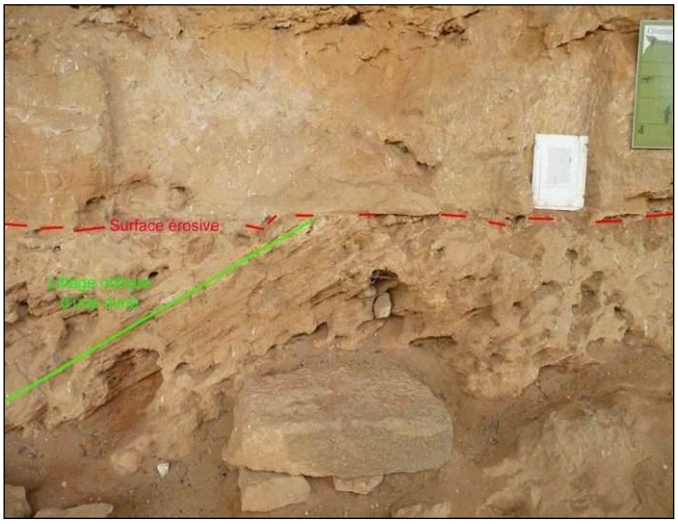

Figure 2-5. Example of hydraulic deposits with different shapes.

2.4 HISTORICAL ROCKFALLS AND CURRENT RISK

The main objective behind the analysis of the historical events is to assess the residual risk that may affect the village and people. To this effect, the main historical cases are reviewed hereinafter to determine the frequency and the different conditions responsible of the process of instability. Afterward, the residual risk associated to the present state of the rock massif will be explained from the field observations.

2.4.1 Historical Rockfalls

In addition to the failure occurred in 2010, the cliff and the troglodyte cavern have undergone several rockfalls of different magnitudes in the last century. Because there are no external loads nor buildings on the cliff, these recurrent instabilities are considered as being the result of the geological characteristics describe above and the possible effect of climatic actions.

The Table 2-1 summarizes the four events of major magnitude. In 1920, a block of several thousands of m^3 fell from the East side of the cliff without causing human casualties. In 1957, one slice detached from the West part and flattened on the center part of the village, killing three persons (Figure 2-6 and Figure 2-7). Several blocks detached further from the cliffs during the year 1994. Although there do not exist detailed studies of the events occurred in 1920 and 1957, the existing field observations shown that these types of overall instabilities are controlled by the different families of discontinuity.

Table 2-1. Main instability events in *La Roque Gageac* . *Technical Report, 2011.*

1920	Part of troglodyte monument fell on the village
1957	A large block fell on the village
1994	Rockfalls from the face of the cliff
2010	Part of the roof fell within the cavern

Figure 2-6. Rockfall in 1920

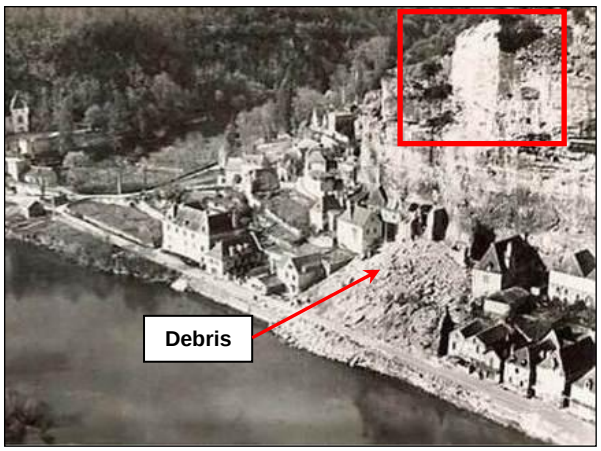

Figure 2-7. Rockfall in January 1957

The last failure occurred during the winter 2010 within the aerial cavern. Part of the roof fell into the cavern, endangering the historical monument and leaving a rock beam of questioning stability at the crown of the cavern (Figure 2-8). Although not known with exactitude, the size of the detached block can be considered as very important.

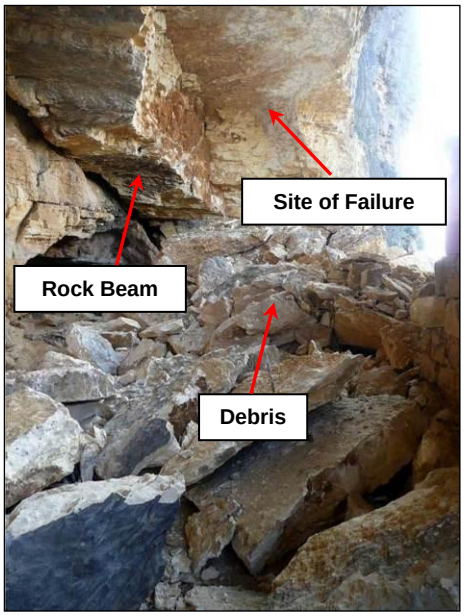

(a)

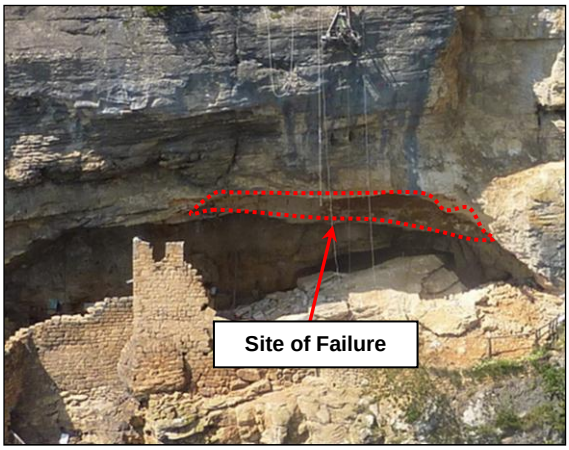

(b)

Figure 2-8. Rockfall in January 2010; a) Residual rock beam and damage within the cavern; b) Location of the Rockfall in the aerial troglodyte cavern

The general location of the different events in shown in Figure 2-9. They are all located above to the village *La Roque Gageac*, wich represents an important risk both in terms of human life and economic losses.

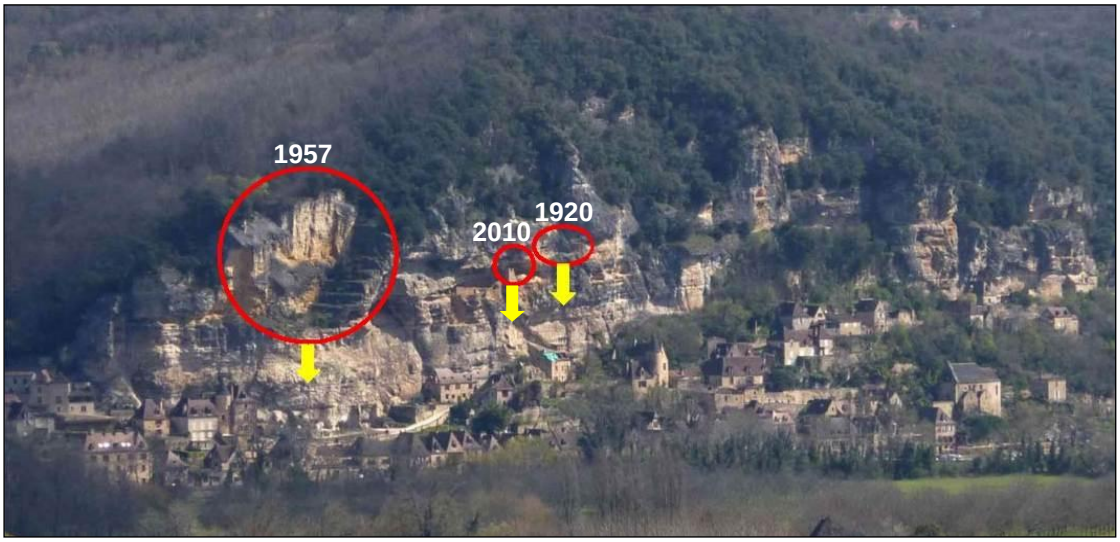

Figure 2-9. General location of the instability events. *Technical Report, 2011*.

An interesting aspect relies in the fact the three last major events (i.e. 1957, 1994 and 2010) occurred during periods of low temperatures; which would suggest that there exists a relationship between the atmospheric conditions and mechanical response of the cliff. This observation leads the LRPC to install a detailed instrumentation whose interpretation would be further aided by a numerical analysis. The instrumentation lay–out is described in Chapter 3 and the interpretation through numerical analysis presented in Chapter 4 to 6.

It is finally to be noted that numerous falls of small blocks has been also recorded during the same period (thirty to forty rockfalls per year). As they didn't cause fatalities or significant economical loss, their location is unknown and they are thus included in the inventory. It is possible that this type of failures is controlled by superficial instabilities associated to the strong flaking that occurs on the surface cliff.

2.4.2 Current Risk

From the historical events, it is expected that the rock-cliff presents, in its current state and under the current environmental condition, three levels of risk associated to different volumes of material:

- The first and lowest level of risk corresponds of the fall of small blocks.
- The second level of risk includes the fall of the material still in place in the roof of the aerial cavern. This failure may have two consequences: to destroy partly or totally the historical ruins present in the cavern and to push the current debris outside the cavern on top of the village.
- The third and highest level corresponds to the fall of a large rock block from the upper part of the cliff, caused by the lost of support resulting from the full cavern roof failure.

The first level of risk is characterized by the low destructiveness of each individual fall but high events frequency (up to 40 times per year). The continuous damaging effect on the structures may thus traduce into a significant risk for the town (Figure 2-11). The small block size and high frequency may be related to the "flaking" detected on the cliff surface and shown in Figure 2-10. This type of process is associated to rock physical-chemical degradation in presence of environmental cycles. In its report, the *Laboratoire Régional des Ponts et Chaussées de Toulouse* mentioned particularly the development of thermal stress due to the temperature cycles as a important factor for the production of flaking in this type of material.

Figure 2-10. Flaking on the surface rock-cliff

As the follow-up of the cliff surface by appropriate instrumentation would extremely costly if not impossible to install practically, some mitigation solutions may be alternatively

contemplated. The solution adopted was the installation of wire meshes (see Figure 2-11 and Figure 2-12) to protect the village against small rock falls. To optimize the location of the protection meshes, the zones of major initiation have to be identified. In that perspective, an interesting point of view is proposed by Pineda *et al*. (2011) who study the degradability of slightly weathered siltstone of Cretaceous age. The authors mention that the weathering process can be induced by drying/wetting cycles at low confining stress, which would explain why the flaking occurs preferably in the unloaded zones of the cliff (above cavern of karst cavity). Mesh protection have thus to be installed in first instance at the toe of these zones.

Figure 2-11. Small block from rock-cliff surface

Figure 2-12. Mesh for smalls to medium rockfalls

The failures of medium or large volumes of material are controlled by families of discontinuities. Two main families of discontinuities are observed in the massif, possibly controlled by stress release during valley formation and major tectonics directions: 1) a family of decametre-spaced, decimetre wide open fractures oriented parallel to the cliff face and 2) a family of vertical diaclases of millimetre to centimetre width that cut orthogonally the fractures. Opening between essentially horizontal stratification planes and superficial flaking can be observed in the decompression zones above the cavern (Figure 2-13).

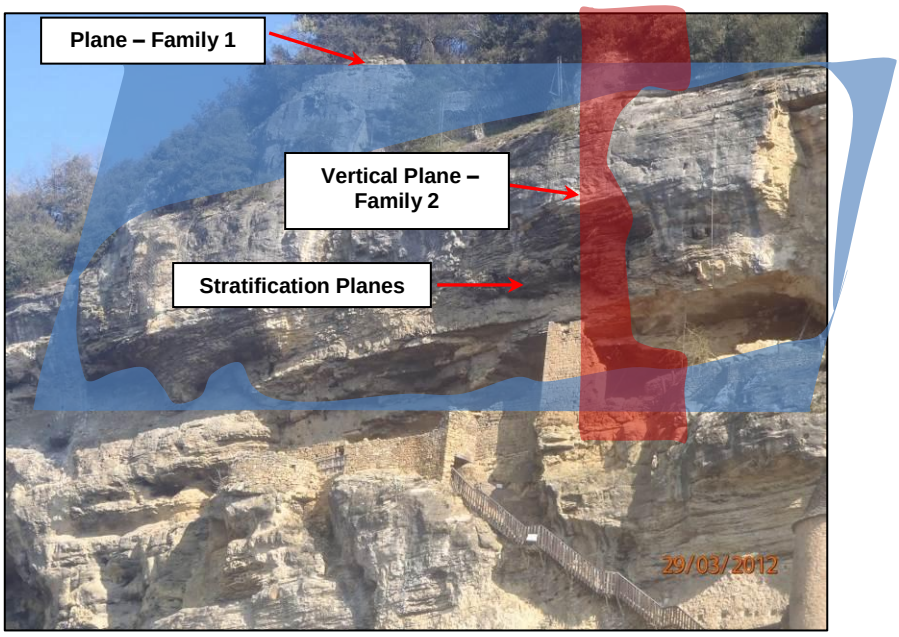

Figure 2-13. Main families of discontinuities

The second level of risk is associated to the failure of the rock beam still in place at the cavern roof and delimited by a stratification plane on the top, a vertical diaclasis on the left and an open fracture at its rear (Figure 2-14 and Figure 2-15). This beam works thus essentially as a cantilevered beam although some additional support is provided by friction along the left-hand diaclasis and rock-bridges across the open fracture. The stability of the beam would depend on the response of all these components to the environmental changes. These effects can be quantified by interpreting the instrumentation results at the light of a numerical model accounting for the interaction rock-atmosphere.

The third level of risk is associated to the failure of large blocks within the cliff. Figure 2-13 shows for instance a large block located on the top of the cavern that may fall if the rock beam fails. According to field observations, these blocks are delimited by large open fractures that cross the rock-cliff and emerge on the top of the massif. The stability of such block can therefore only be explained by the existence of rock-bridges within the discontinuities, whose mechanical degradation under environmental cycles may be the triggering factor for major events. The penetration depth of the climatic cycles applied at the cliff surface is a important controlling factor for this process. It can be assess through a numerical model calibrated on the measurements available around the cavern and extrapolated to higher depth in the massif. The

hazard can be further increase by the presence of karst cavities surrounded by unloaded arches where the material is provided with a low strength. Figure 2-16 shows a block located in a neighbouring cliff with a high hazard due to the presence of open fractures and decompressed zones.

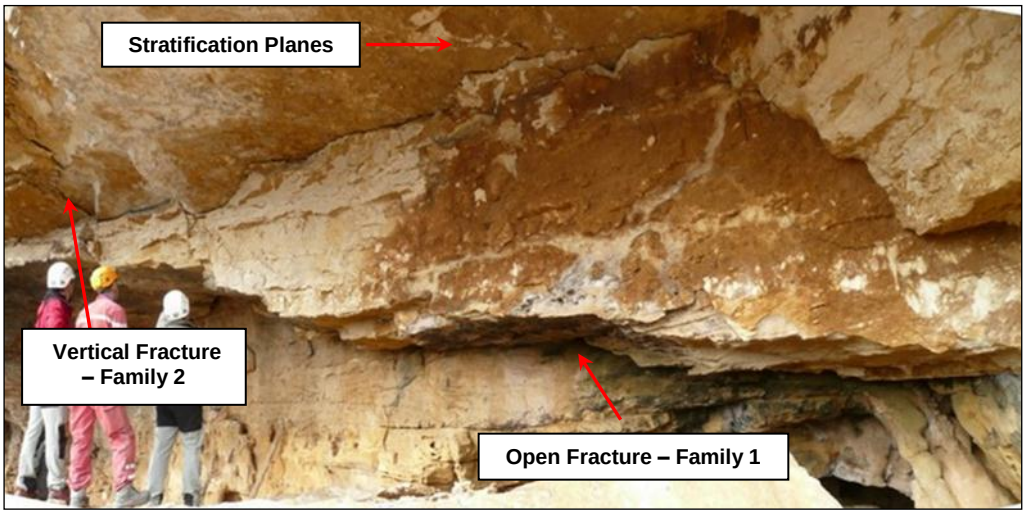

Figure 2-14. Residual rock beam within the troglodyte cavern

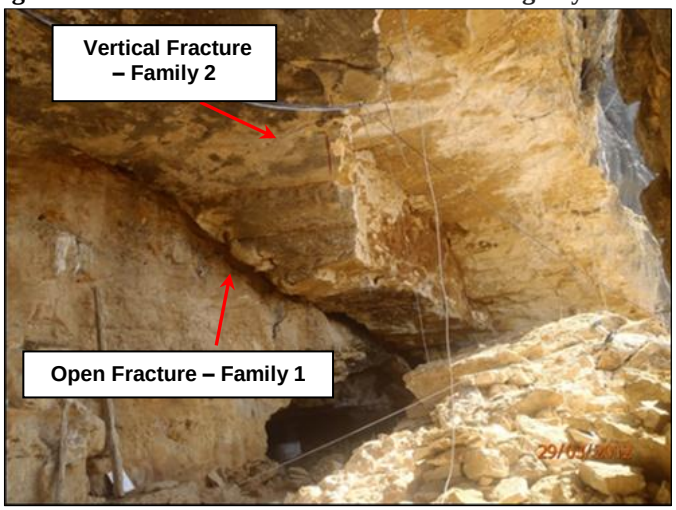

Figure 2-15. Open fracture limiting with the rock beam

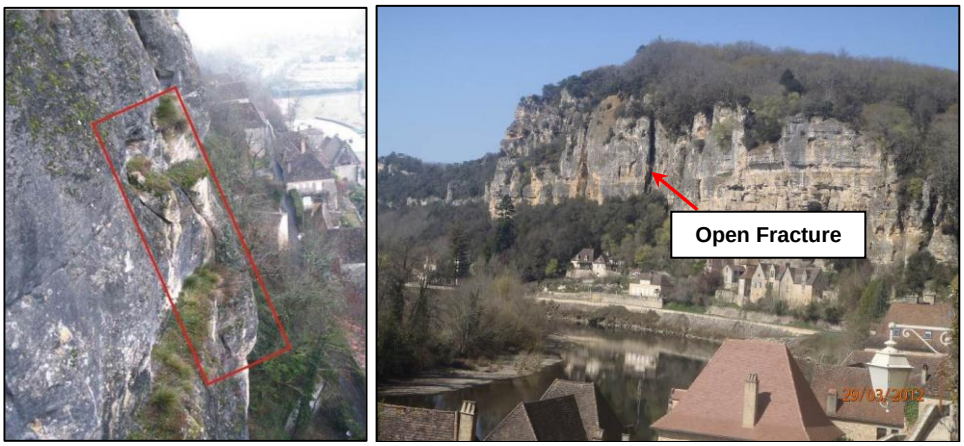

Figure 2-16. Open fractures and decompressed zones of another cliff near to site of study.

2.5 RELATION BETWEEN ROCK-CLIFF BEHAVIOUR AND CLIMATIC ACTIONS

As mentioned previously the rocks falls have a relationship with the atmosphere effects, specifically with the thermal cycles. Here will be described the general aspect of the climate zone and the effects on the mechanical behaviour will be described in the Chapter 3.

2.5.1 Climate

According to the technical report of *Laboratoire Régional des Ponts et Chaussées de Toulouse* (2011), the climate of the department Dordogne is greatly influenced by the oceanic dynamics. During winter, the climate is affected by the nearby Central Mountain system while, in summer, warm air masses coming from the Mediterranean has important climatic effects.

At regional level, the annual maximum temperatures range between 27^{o}C and 32^{o}C, and the minimum temperature between -10^{o}C and -15^{o}C. The average annual rainfall is 860 mm and the historical maximum occurred in May 1971 (100mm).

For the numerical analysis of the rock-atmosphere interactions, a complete set of local meteorological data is necessary. In absence of an *in situ* monitoring station, data from the nearest meteorological station, located at Sarlat town, at a distance of ten kilometres will be used for the modelling works..

2.6 REFERENCES

Laboratoire Régional des Ponts et Chaussées de Toulouse., 2011. La Roque Gageac - Endommagement de la roche sous l'effet des cycles thermiques. *Report Project DOSMS*

Pineda, J., Romero, E., Gómez, S., Alonso, E. 2011. Degradation effects at microstructural scale and their consequences on macroscopic behaviour of a slightly weathered silstone. *Geomechanics and Geotechnics, From Micro to Macro – Jiang et al. (eds)*, 73-78.

Ruiz, D., Vaunat, J., Samat, S. & Virely, D. 2012. Thermo-mechanical modelling of an aerial cavern under climatic actions. *4$_{th}$ Workshop CODE_BRIGHT*, Barcelona.

Vaunat, J., Samat, S., Alonso, E., Ruiz, D., Martin, E., Saillard, M., Virely, D. & Darrozes, J. 2012. Slope responses under climatic actions. Model and case interpretation. *In preparation*.

CHAPTER 3

FIELD INSTRUMENTATION AND LABORATORY TESTING

This chapter focuses on the presentation of the field instrumentation lay-out, a first interpretation of the measurements and their meaning for the behaviour of the failed and poor stability zones as well as the results of laboratory tests performed on debris samples.

3.1 FIELD INSTRUMENTATION

3.1.1 Instrumentation lay-out

Two main types of field information will be monitored: the atmospheric variables and the deformation of the massif.

The atmospheric data were provided by the French Service of Meteorology. They come from the meteorological station *Sarlat -LaCanéda* located at 10 kilometres from study area. The Figure 3-1 shows records of the daily temperature obtained between July 2010 and June 2011 and the daily precipitation between July 2010 and April 2010.

The precipitation register, which covers a period of 8 months, indicate that strong precipitations occurred during the fall, season for which failures has been never reported. Moreover, the absence of karstification at the face of the cliff and around the aerial cavern suggests that water do not have significant degradation effect in this zone of the cliff. As consequence, although the influence of rain cannot be totally ruled out, the emphasis will be put on the study of the relationships between thermal cycles, cliff deformation and instability through the direct interpretation of instrumentation measurements and the development of numerical modelling to reproduce them.

Figure 3-2 shows a comparison between the temperatures registered at the meteorological station *Sarlat-La Canéda* (each day) and the values measured within the cavern (each hour). A good agreement can be observed, validating the representativity of the regional temperature histogram at the local site. As a consequence, temperature measurements within the cavern will be use to prescribe air temperature at the cliff face for dates after the end of Sarlat regional record

(available between July 2010 and June 2011). The temperature has amplitude with a maximum temperature of 29ºC and minimum temperature of -10 ºC.

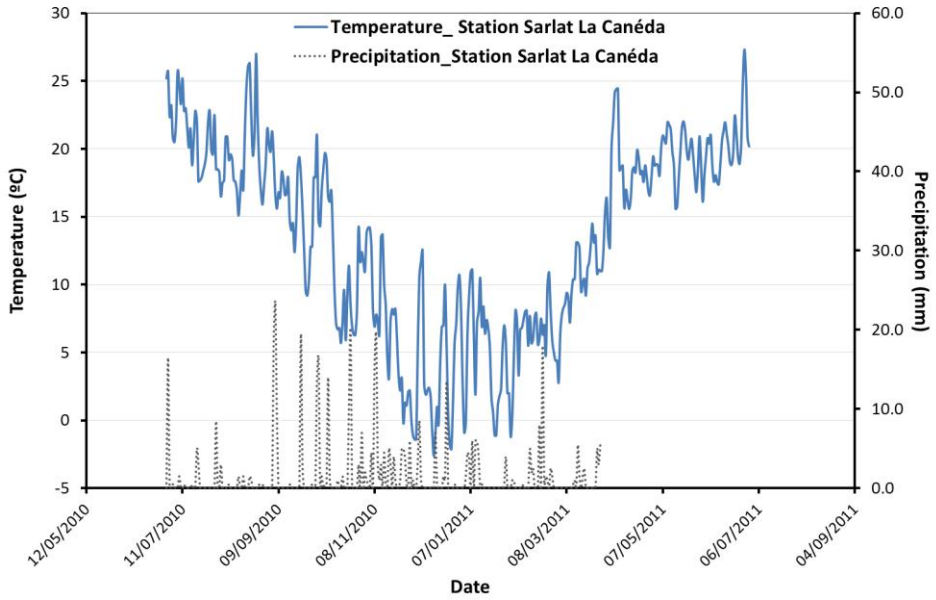

Figure 3-1. Data of the Meteorological station Sarlat_La Canéda

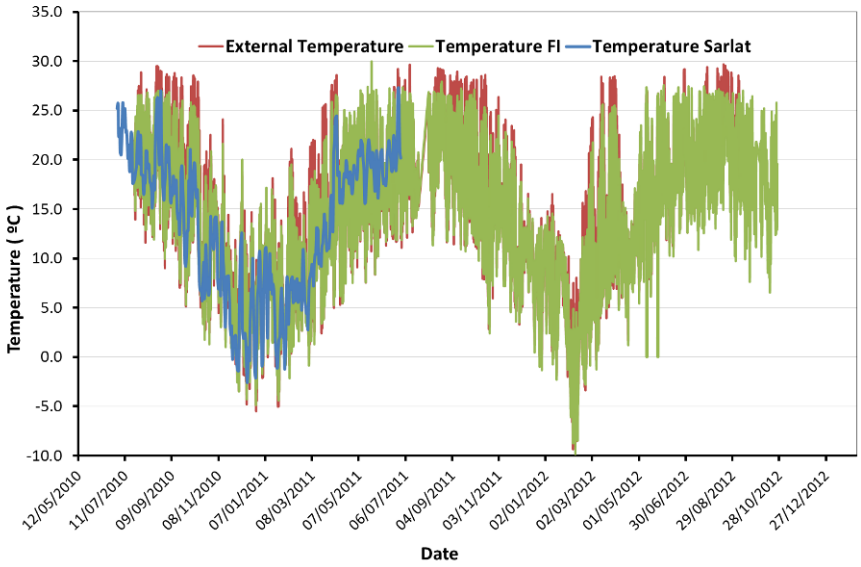

Figure 3-2. Comparison between temperatures registered at the meteorological station and measured within the cavern.

Figure 3-3 present a general overview of the instrumentation survey, which consists in monitoring displacement and temperature in the cavern and on the cliff upper face.

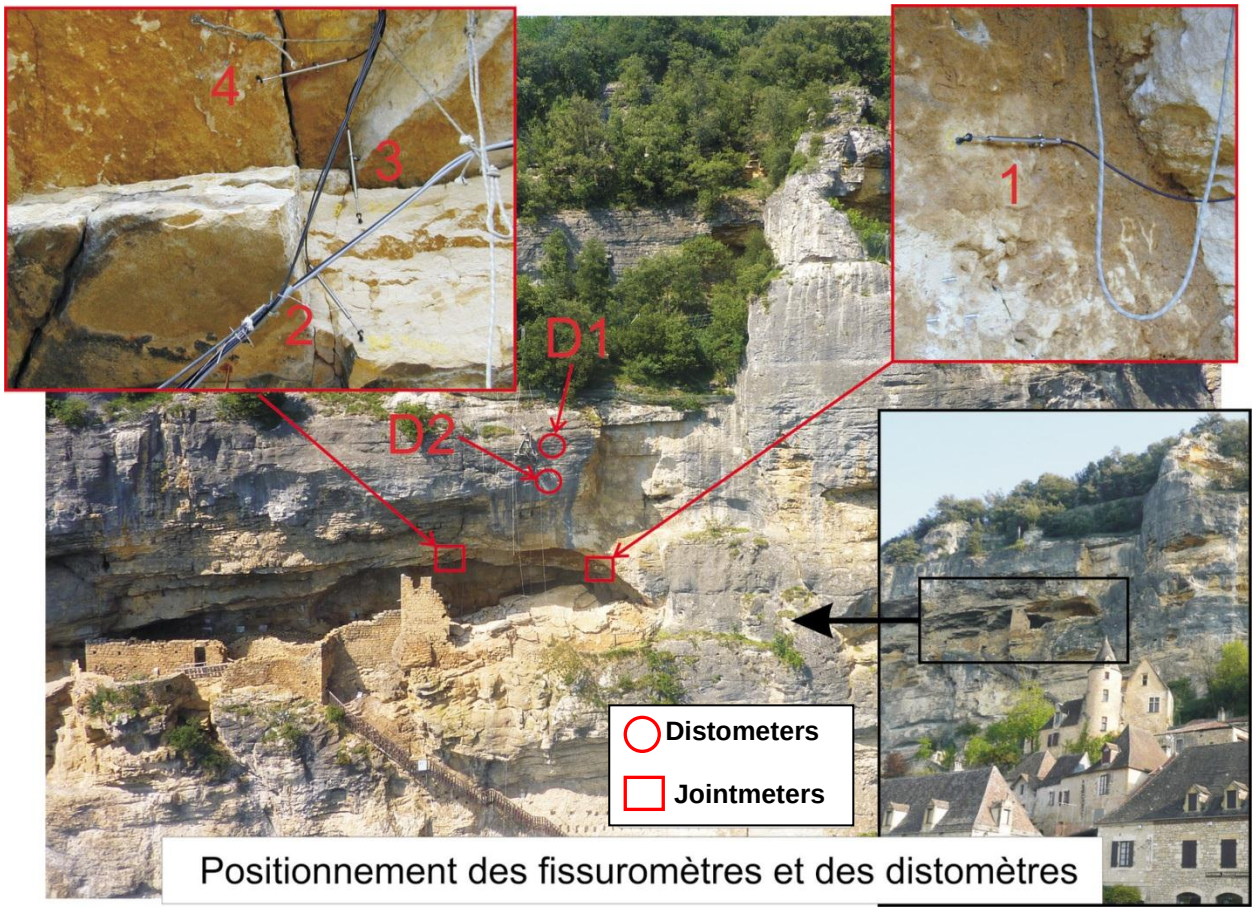

Figure 3-3. Localization of the instrumentation system.

Displacements are monitored by jointmeters and extensometers. Jointmeters were installed with the aim of evaluating the time evolution of the beam behaviour. They provide measurements of relative displacements across the discontinuities delimiting the rock beam within the cavern (Figure 3-3):

- the relative vertical displacement across the horizontal discontinuity existing between the top of the beam and cavern vault (provided by jointmeter 3),
- the relative horizontal displacement across the vertical diaclasis that cuts the beam close to one of its support (measured by jointmeter 4) and finally,
- the relative displacements across the discontinuities located at both end of the beam and acting are support (jointmeters 1 and 2).

Measurements are completed by cavern convergence measurements (between points I3-I4, I0-I1 and I0-I2 in Figure 3-21) Temperature within the cavern is also registered.

Two extensometers (distometers) provided with thermal sensors and installed in boreholes drilled horizontally from the cliff face above the cavern (D1 and D2) allow to follow-up displacements and temperature at 2, 4 and 6 m in depth in the rock. Convergences between superficial spots located on one vertical line between the top of the cliff and the cavern roof complete the survey. (Figure 3-21)

3.1.2 Basic interpretation of measurements

In this section, some preliminary insights are explored into the possible relationships between temperature variations, rock displacements and failure mechanisms. They will be further investigated by means of numerical simulations in the Chapters 5 and 6.

Two main scenarios are considered as possible:

- Failure due to rock degradation and accumulation of contraction and expansion strains after many cycles of temperatures. The pertinence of this scenario is difficult to assess on the basis of the two-years long register as it may require much more cycles to becomes evident.
- Failure associated to irrecoverable deformations caused by temperature minima reaching a given threshold. The possible existence of such a mechanism can be more easily appreciated as temperature reaches different minima during year 2010 and 2011 that can be related with the displacements measured in both the extensometers and the jointmeters.

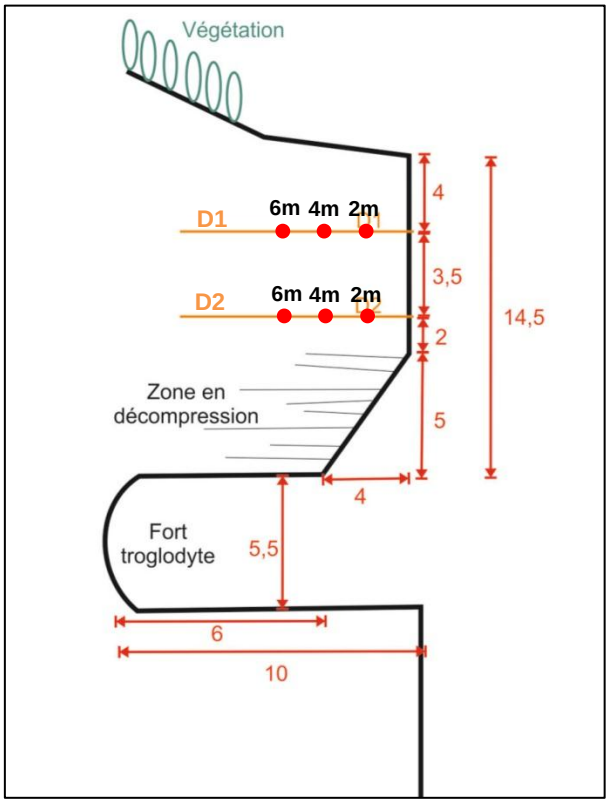

Figure 3-4. Cross section through troglodyte cavern. Measurements in meters

The exact location of the extensometers are indicated in the cross section shown in the Figure 3-4, that passes through the extensometer axes and cut the troglodyte cavern. The extensometers appear to be outside of the decompressed zones at the cavern roof, but their response may still be affected by the presence of discontinuity planes.

Temperature series registered in extensometer D1 and D2 are depicted in the Figure 3-5 and Figure 3-6. Temperature sensors are located close to the bases of the extensometers, at a distance of 2 and 6 m from the cliff face. It appears that:

- Temperature values are lower in extensometer D1 than in D2. Possible explanations rely in the difference in distance between the extensometer and the cavern wall (exposed to the atmosphere) or in the difference in sun incidence angle.
- Temperature cycle experiments a attenuation in magnitude and a delay in phase with depth, which is consistent with the diffusive character of the heat equation. Between 2m and 6 m, the delay is of approximately equal to 40 days.

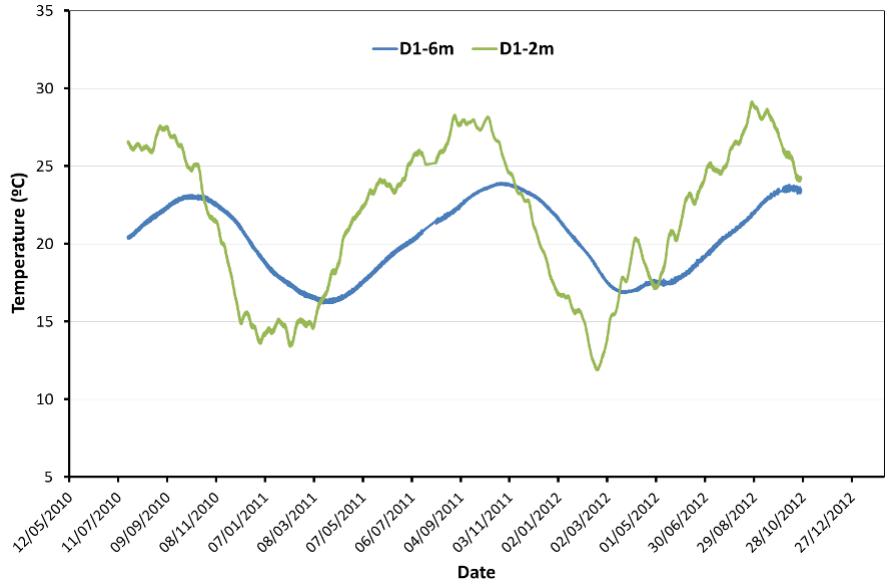

Figure 3-5. Time evolution of temperature _ Distometer D1

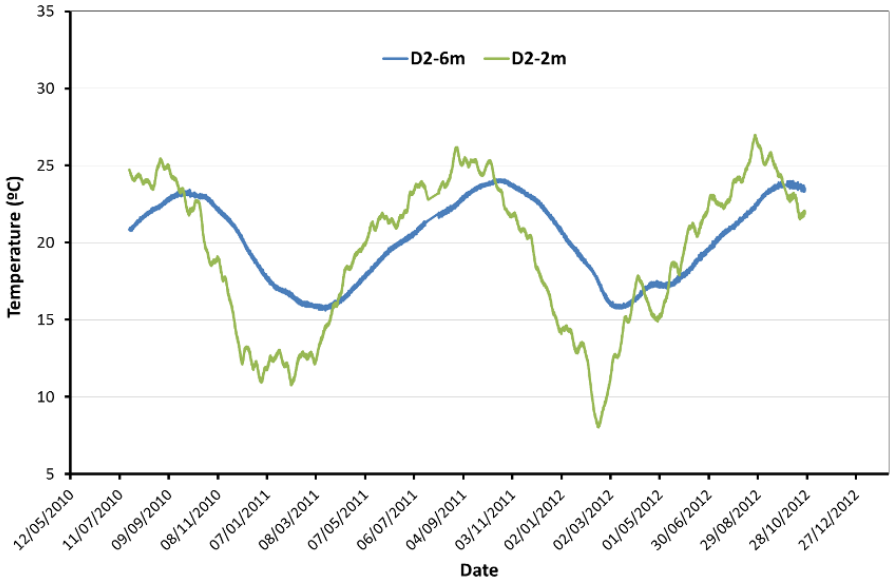

Figure 3-6. Time evolution of temperature _ Distometer D2

Measurements of displacement in the extensometers (Figure 3-7 for D1 and Figure 3-8 for D2) provide quantitative information about the effect of atmospheric cycles on the rock massif. The strong relationship between rock displacement and external temperature (Figure 3-7b and Figure 3-8b) strengthens the assumption that heat input from the atmosphere is the main controlling factor of cliff deformation.

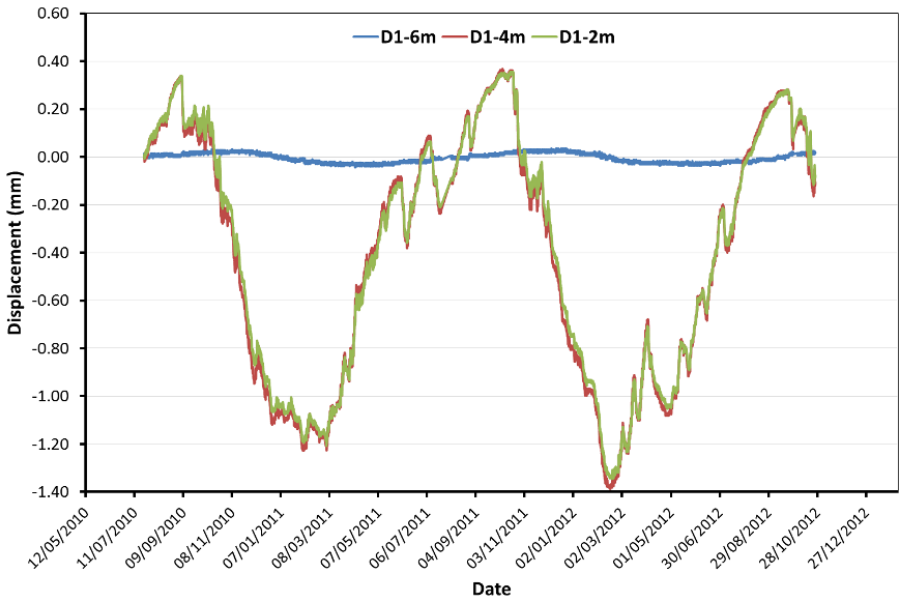

(a)

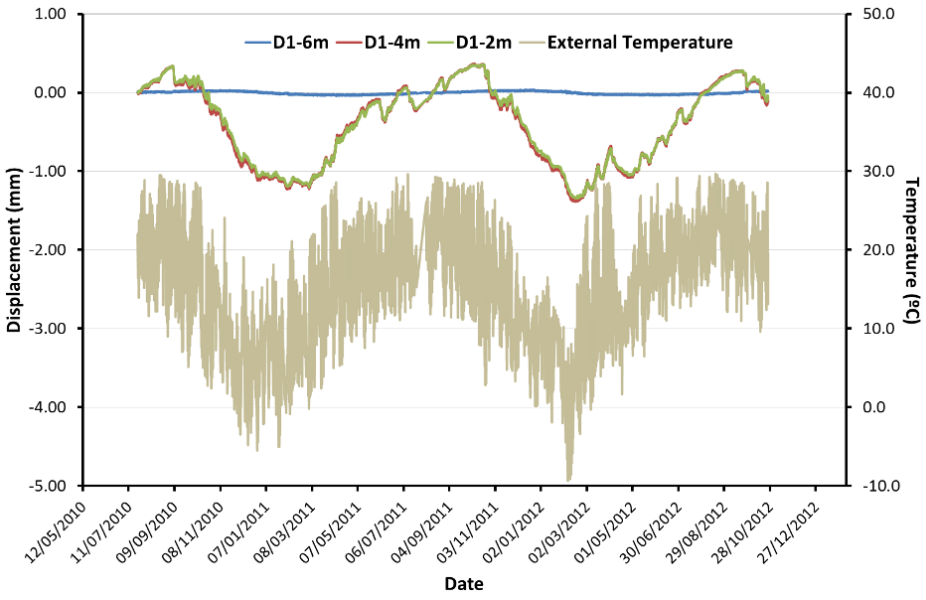

(b)

Figure 3-7. Time evolution of displacement _ Distometer D1; a) Displacement at 2m, 4m and 6m; b) Relationship Temperature-Displacement

Further conclusion can be drawn from the extensometerrs deformations. give the relative displacement from the end of them, considering its extreme point in the rock without movements. Negative values correspond to contractions generate when the external temperature is low and the positive values mean expansion when the external temperature is high (Figure 3-7

and Figure 3-8). The amplitude of the series is larger in the negative values (contractions) than the positive values due to the distometers were installed in July 2010 (Summer) when the rock massif was expanded. Both distometers don't have irreversible strains under thermic cycles instrumented, despite the low temperature registered in 2011.

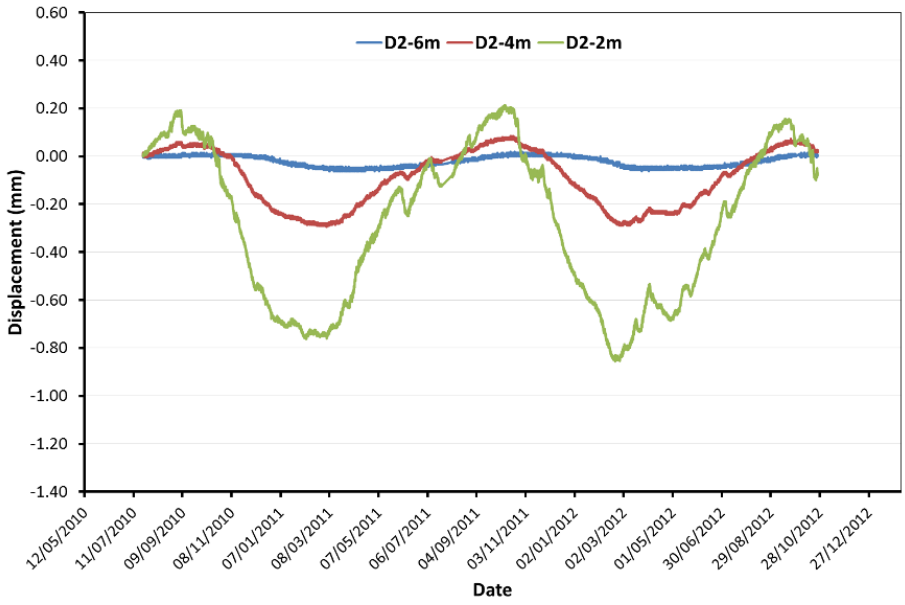

(a)

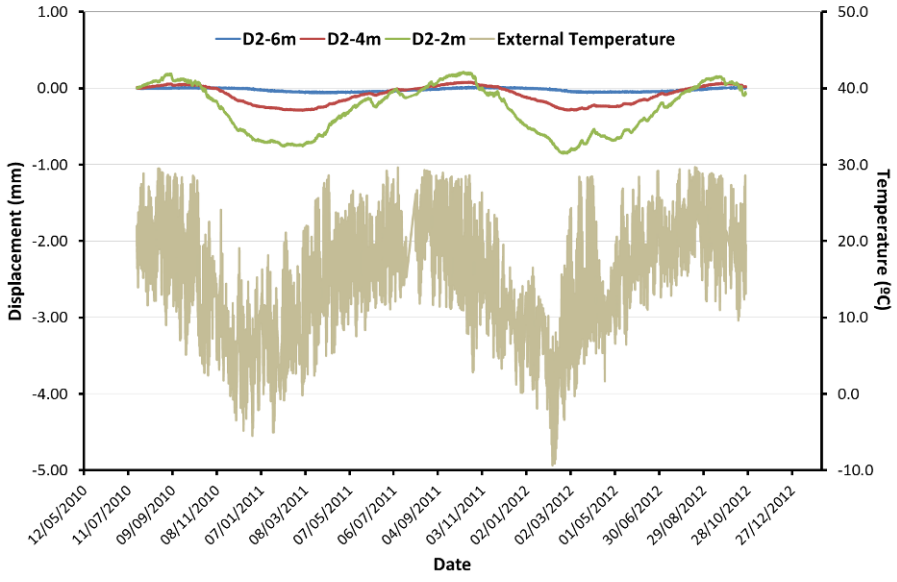

(b)

Figure 3-8. Time evolution of displacement _ Distometer D2; a) Displacement at 2m, 4m and 6m; b) Relationship Temperature-Displacement

A special response in the distometer D1 is that displacement series at 2 meters and 4 meters are equal, evidencing a block movement very different to displacement distribution due to thermal effects. If the time evolution of the temperature in the distometer D1 is inspected, the values at 2 meters have more extreme temperature than values observed at 4 meters, therefore the displacement at 2 meters should be higher, but it doesn't happen. Unlike the distometer D1, the distometer D2 presents a homogeneous deformation induced by the thermal load on the cliff

face, with higher values at 2 meter that 4 meter values (Figure 3-5, Figure 3-6, Figure 3-7 and Figure 3-8). The displacements in the distometer D2 have lower values than values registered in the distometer D1 and it happens due to that temperature in this point is lower.

The thermal strains showed in the Figure 3-9 and Figure 3-10 are obtained respect to final point of distometer (6m). The thermal strain at 4 meters in the equipment D1 is higher, checking the movement type block described above.

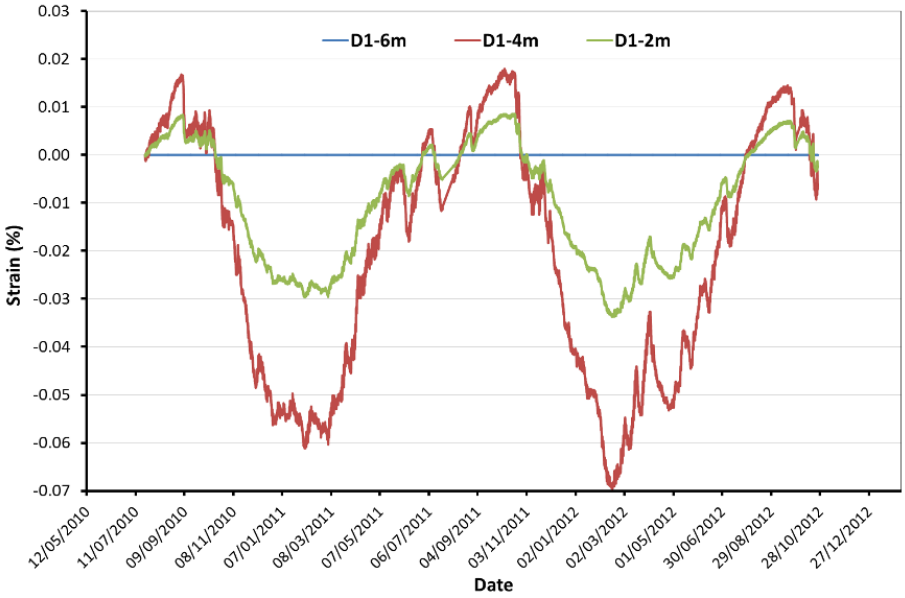

Figure 3-9. Time evolution of Strain _ Distometer D1

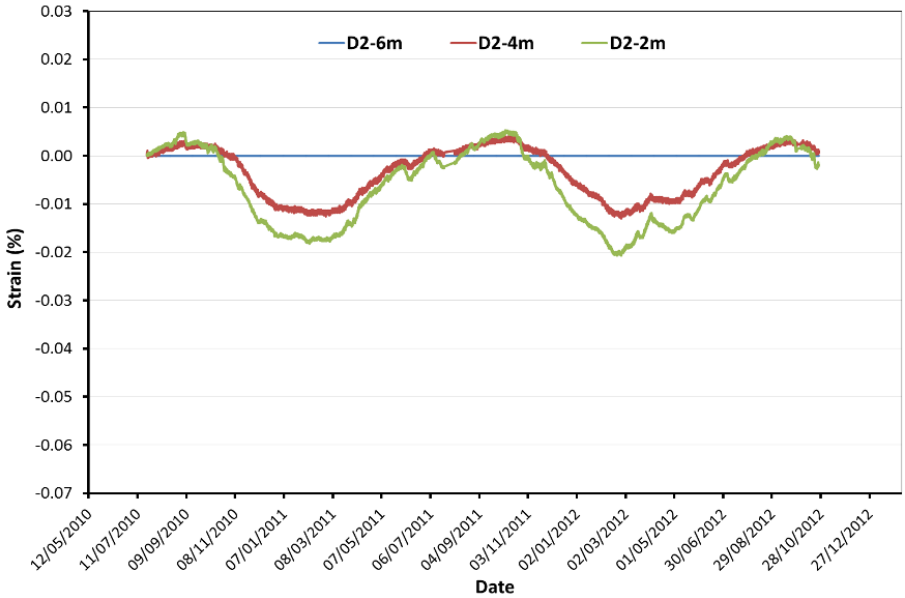

Figure 3-10. Time evolution of Strain _ Distometer D2

A possible explanation of the behaviour type block observed in the distometer D1 is a plane of discontinuity that crosses the distometer site (Figure 3-11). This plane does not cross the

troglodyte cavern, but probably the distometer D1 was installed through this plane (Figure 3-11b).

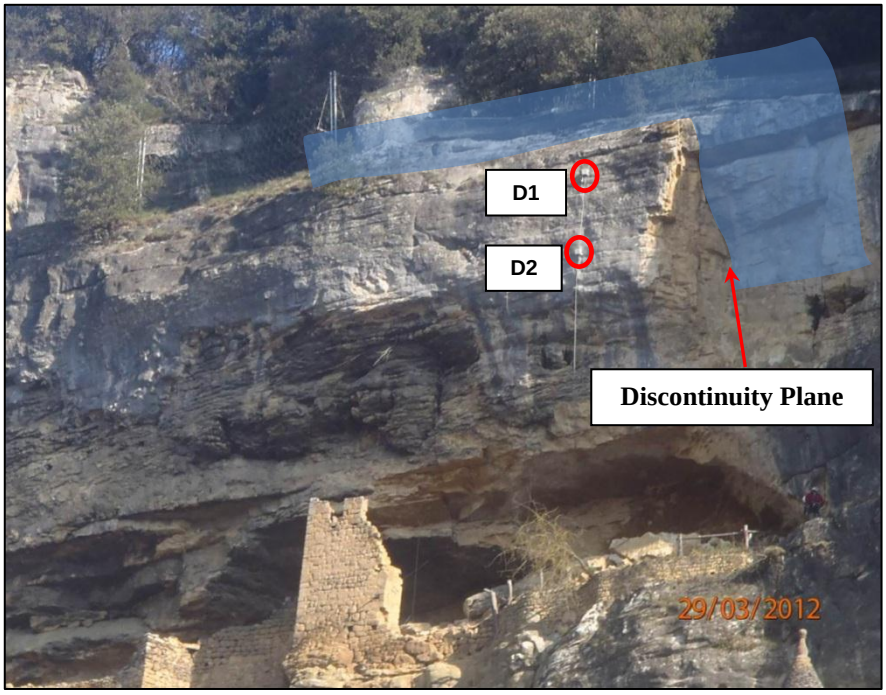

(a)

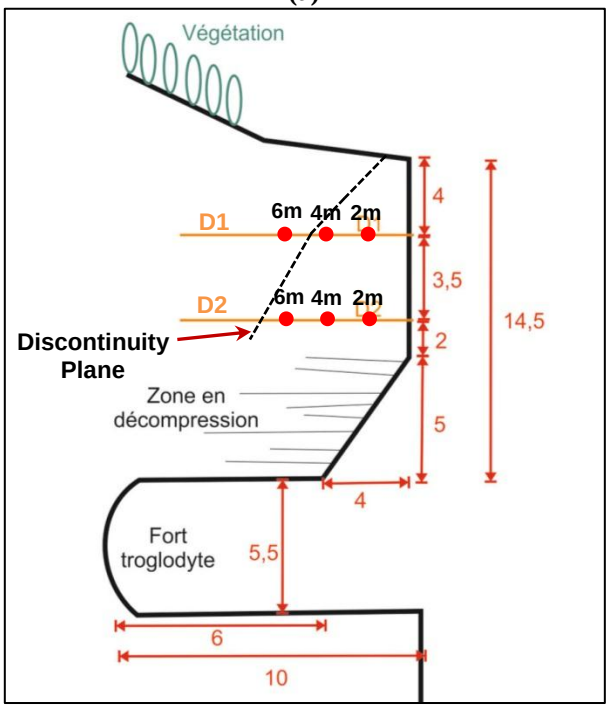

(b)

Figure 3-11. Discontinuity plane across distometers site; a) Location of the plain discontinuity; b) Cross section through troglodyte cavern

Now the evolution of the joinmeters is described. The jointmeters evaluate the time evolution of the displacement across the discontinuities delimiting the roof of the cavern and the rock beam within the cavern. The Figure 3-12 shows the displacement changes against thermic cycles; again the displacements follows very close the temperature register.

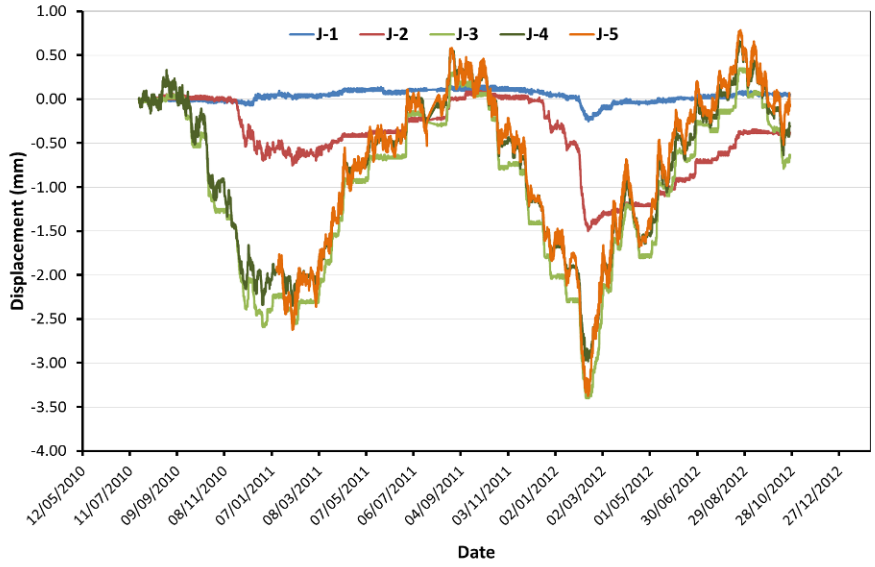

(a)

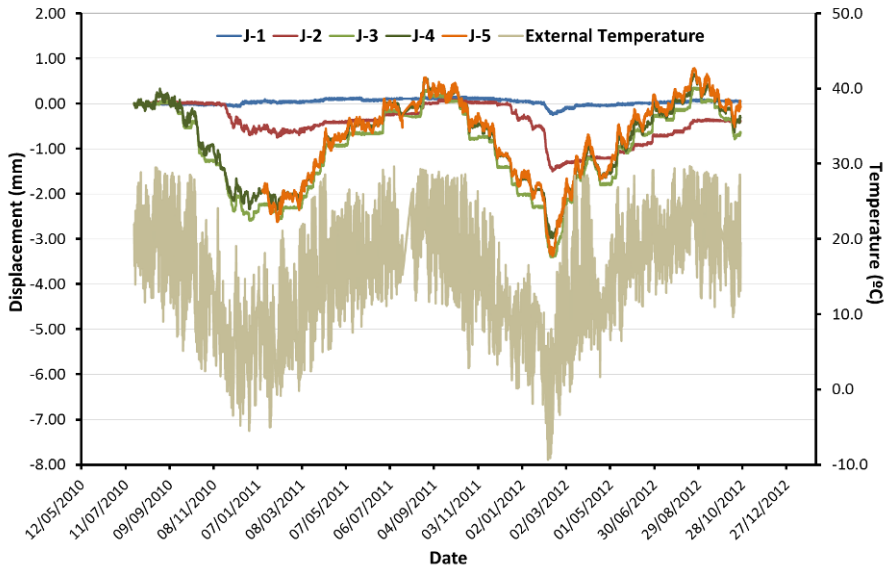

(b)

Figure 3-12. Time evolution of displacement _ Jointmeters J1, J2, J3; J4 and J5; a) Time evolution of displacement; b) Relation Temperature-Displacement

As shown in the Figure 3-3, the displacements at roof of the troglodyte cavern are studied by de joitmeters J-3, J-4 and J-5. The jointmeters J-1 and J-2 study the support points of the residual beam within the cavern. The joitmeters J-3, J-4 and J-5 know reversible displacements under thermic cycles; however the jointmeters J-1 and J-2 present irreversible displacements due to the low temperature in February 2012 explained by a particularly cold week associated to the arrival of polar air mass on Europe. The irreversible displacement due to extreme values of lower temperature indicates that the failures occur when a threshold temperature is reached.

The behaviour of the jointmeters and therefore the discontinuities againts effects of external temperature is opposite to presented in the distometers. A distometer or extensometer measures the effect on the rock body under thermic cycles, hence a contractions is produces in low

temperatures and expansion when the temperature is high. However the jointmeters measures the displacement evolutions of a discontinuity between rock bodies which suffer contractions at low temperatures and therefore the discontinuity is opened; this mechanism is very similar to the tensile fracturing of the rock (mode1) reported by Hudson & Harrison 1997. The mechanism is explained in the Figure 3-13.

As conclusion, the negative values in the displacements series indicate the aperture of the discontinuities at wintertime. If the joint aperture increases the contact area for resisting the weight of the blocks decreases, hence a stress concentration occurs and the failures can be generated. The threshold of low temperature produces extreme apertures and irreversible displacements are observed.

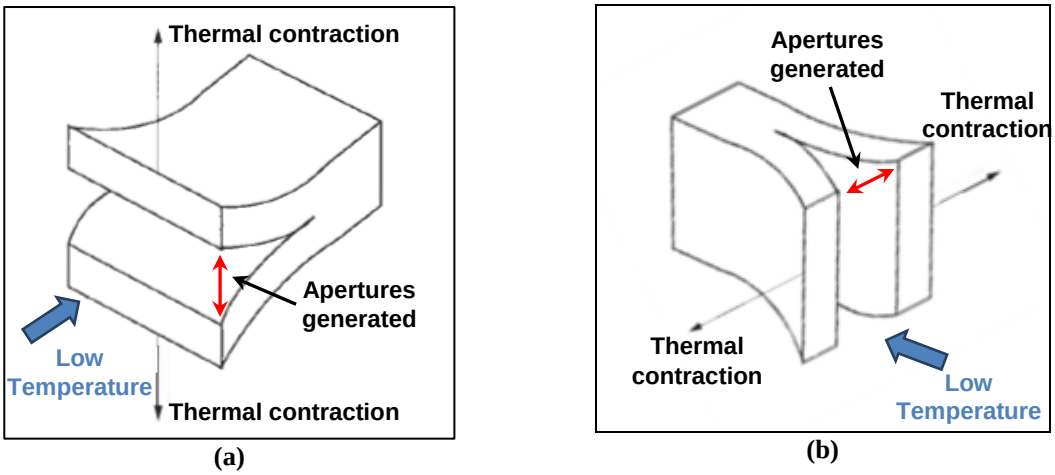

Figure 3-13. Mechanism of discontinuities against low temperature values; a) Horizontal discontinuity; b) Vertical diaclases

A remarkable response of the joinmeters data is that displacement which measure the horizontal joint at the roof of the cavern are larger than the measurements done on the vertical cracks limiting the beam. The design of underground mines the stability of the roof has been studied widely through *Rock Voussoir Beam* concept which evaluates the stability of the multi-jointed beam located in the roof of the excavations. Sofianos (1996) reports that through experimenting on such stacks of beams it is noted that the lowest beam is not loaded by the upper ones. The gravitational load of the uppermost beams is clearly transferred laterally to the supports rather than vertically on the lowest member. This process mobilizes friction between the surfaces of the upper beams and generates an arch structure above the mine opening. Thus the rock beds above the roof of the mined opening and below the arch are decoupled and the lowest rock bed may be considered as loaded by its own weight only. For the case of *La Roque Gageac* the roof of the troglodyte cavern is subjected possibly to only weight in the vertical direction, but horizontally it can be subjected to high stress from tectonic origin. The above postulate may explain the difference in the amplitude, however the Jointmeter J-4 shows large amplitude and it is measures a vertical joint.

The irreversible displacement in the equipments J-1 and J-2 checks the poor stability of the beam and a possibility of its failure after some thermal cycles (Figure 3-16 and Figure 3-17). Is necessary to study the behaviour and response of the support points and how the beam moves under the atmospheric temperature.

The jointmeter J-1 was initially installed for measure the vertical crack in the extreme support of the beam. This support point has a fracture composed of horizontal and vertical segments (Figure 3-18), for this reason the device was relocated in December 2010 with the objective to follow the evolution of horizontal segment of the crack (Figure 3-14). The position changes and the current site influence the responses of the jointmeter J-1.

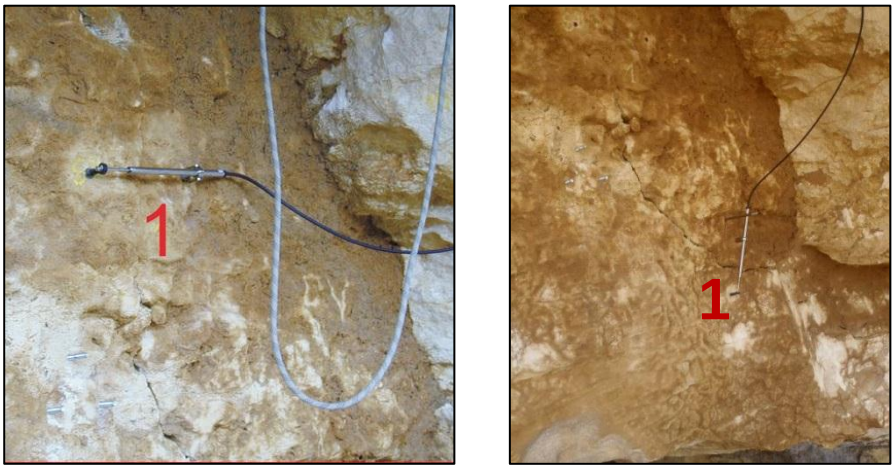

(a) **(b)**

Figure 3-14. Different orientation of the Jointmeter J-1; a) July 2010 to December 2010; b) December 2010 until the present time

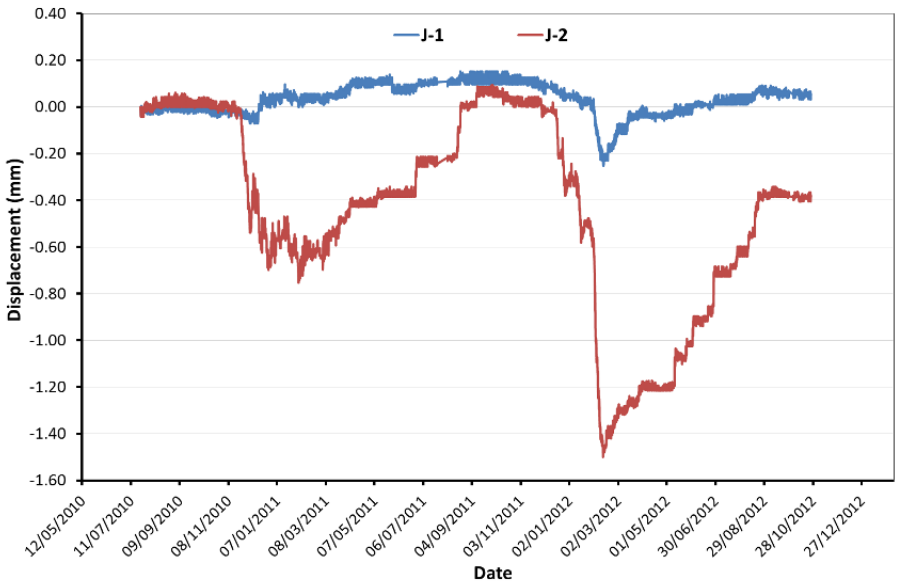

Figure 3-15. Time evolution of displacement _ Jointmeters J-1 and J-2

The Figure 3-16 and Figure 3-17 indicates the magnitude of irreversible displacement. Both discontinuities suffer permanent aperture after the low temperatures registered in 2011. The discontinuity located at the middle of the troglodyte cavern had a permanent displacement five times greater than the permanent displacement at the other extreme of the beam. The difference in the irreversible displacements generates a deflection on the beam (Figure 3-18).

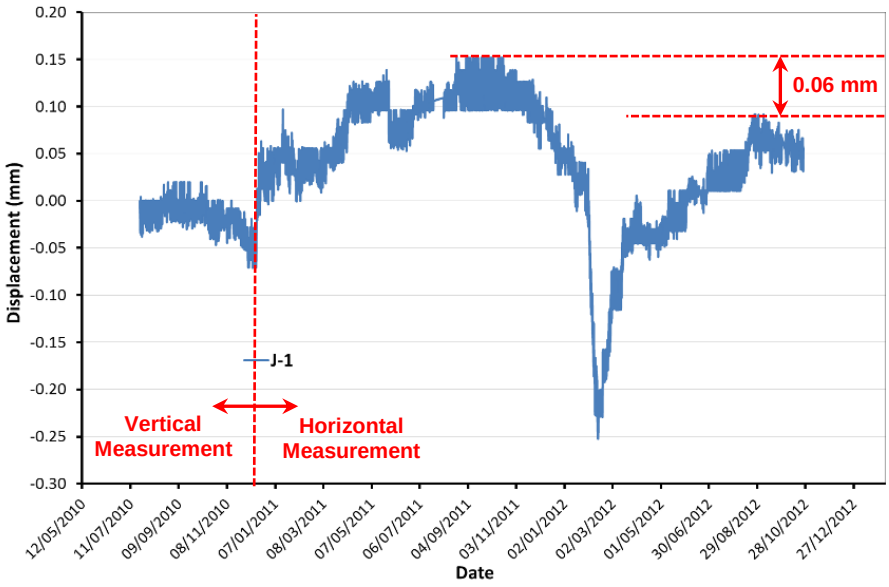

Figure 3-16. Irreversible displacement Jointmeter J-1

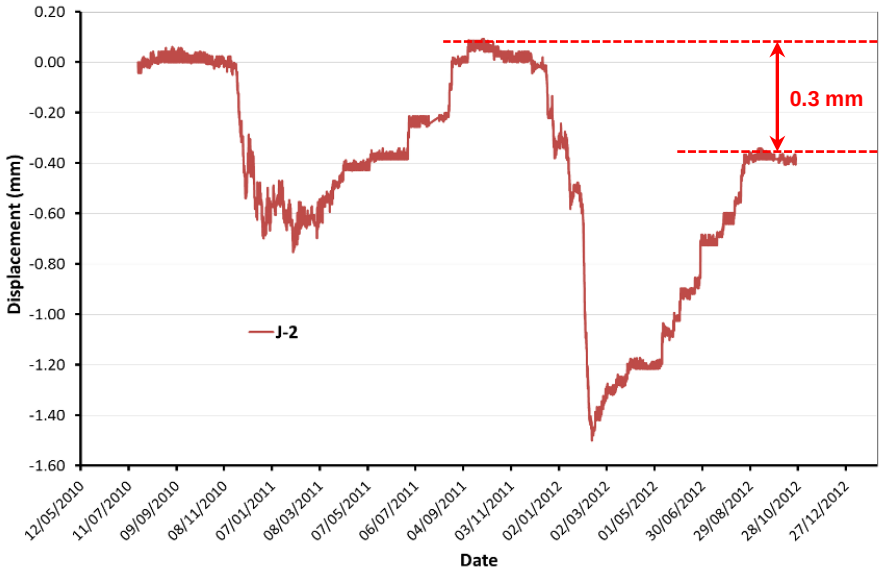

Figure 3-17. Irreversible displacement Jointmeter J-2

During the wintertime, the beam knows thermal contractions causing the aperture of the joints that delimiting the beam, therefore overall beam moves with a large magnitude in the middle of the cavern. As the beam only support its only weight an increases in the tensile strength at extreme of this occurs due to that the contact surfaces decreases (Figure 3-13).

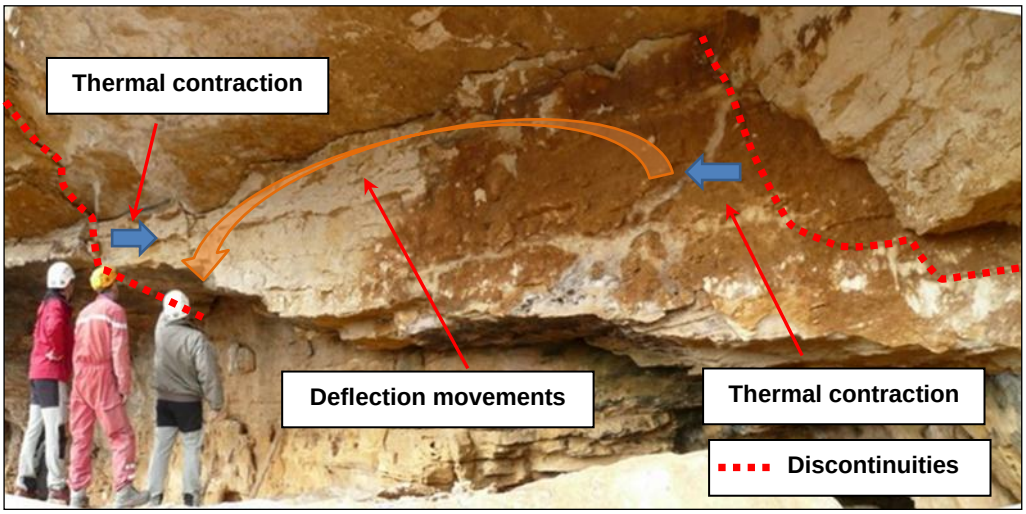

Figure 3-18. Movement of the beam against low temperature.

A review of the location of the jointmeter J-2 shows this isn't perpendicular to the vertical joint at the middle of the cavern and from the angle between the device and the discontinuity is possible a decomposition of the movement. The Figure 3-19 shows the horizontal and vertical displacements obtain from the instrumentation data. As a conclusion the beam presents apertures and declines irreversible.

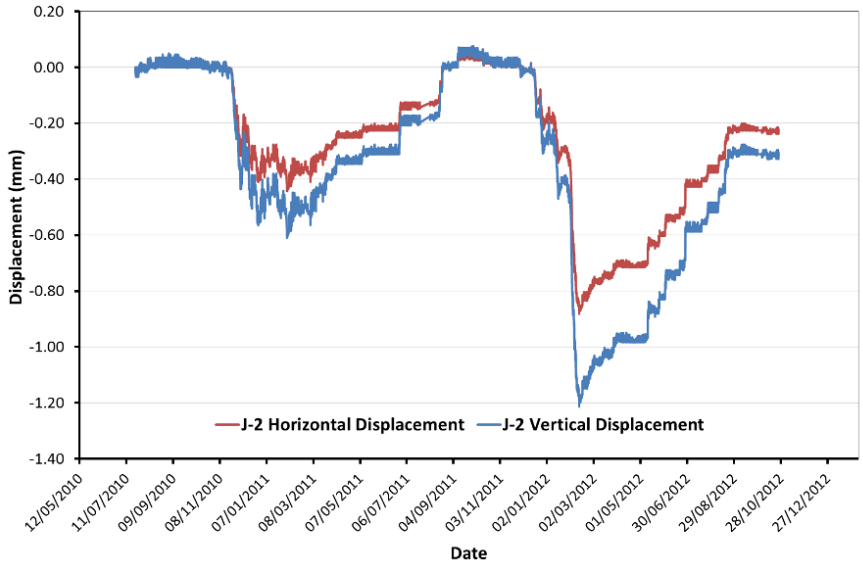

Figure 3-19. Displacement components Jointmeter J-2

A comparison between the displacements registered by the joinmeters and distometers shows larger values in the discontinuities; taking into account that negative values in the distometers indicate contractions and an opposite response in the jointmeters. The previous convention was fixed to compare the magnitude of both instrumentation systems.

Although the displacements in the jointmeters are three time larger that distometers value, the most important comparison must be with the strains. As concluded previously the thermal strain

in the distometers (continuous rock strains) are less than 0.1%. Even though the jointmeters don't have a fixed points to calculate the relative strains is possible to obtain the strain respect the length of the instruments (20 cm aprox); hence the thermal strains can have magnitudes of 2% (30 times larger than distometer values). The discontinuities and low confinement are the main factors to generate large thermal strains at the roof of the cavern.

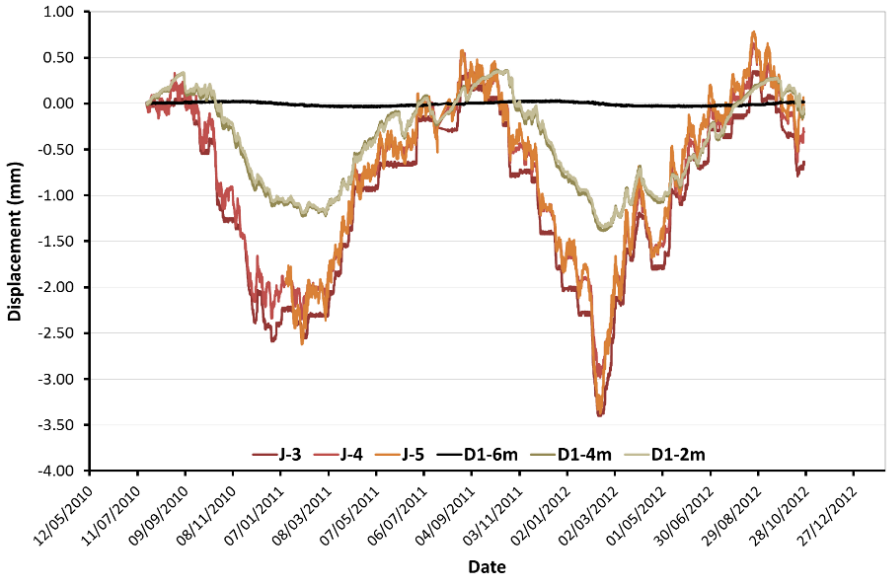

(a)

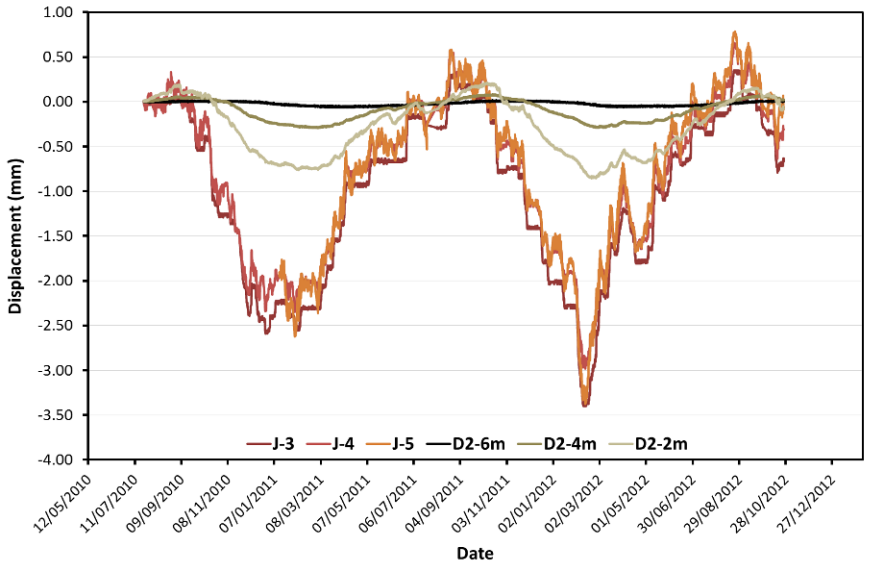

(b)

Figure 3-20. Displacement comparison between distometers and jointmeters; a) Jointmeters vs Distometer D1; b) Jointmeters vs Distometer D2

The instrumentation system is completed whit the convergence measurements of the cavern and the decompressed zone at top of the cavern Figure 3-21. With monthly frequency its results are compared with the data of the distometers and jointmeters (Figure 3-22).

(a) **(b)**

Figure 3-21. Convergence Measurements; a) Superficial spots located on one vertical line at top of the cavern; b) Within the cavern

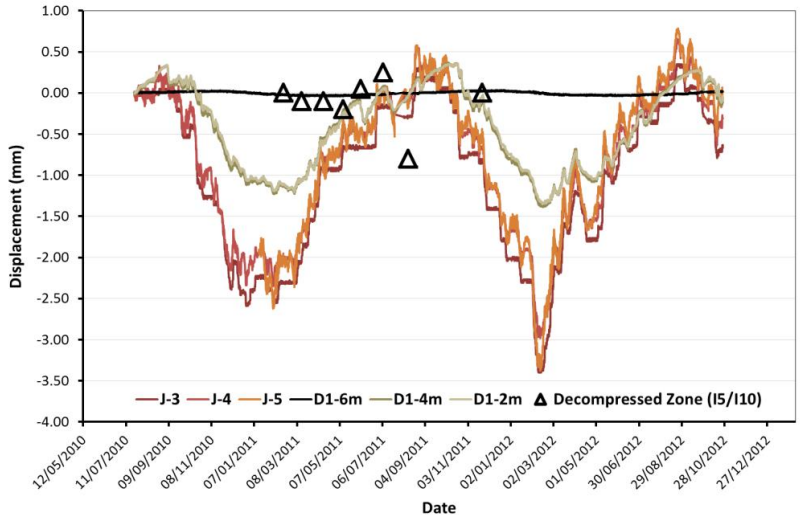

(a)

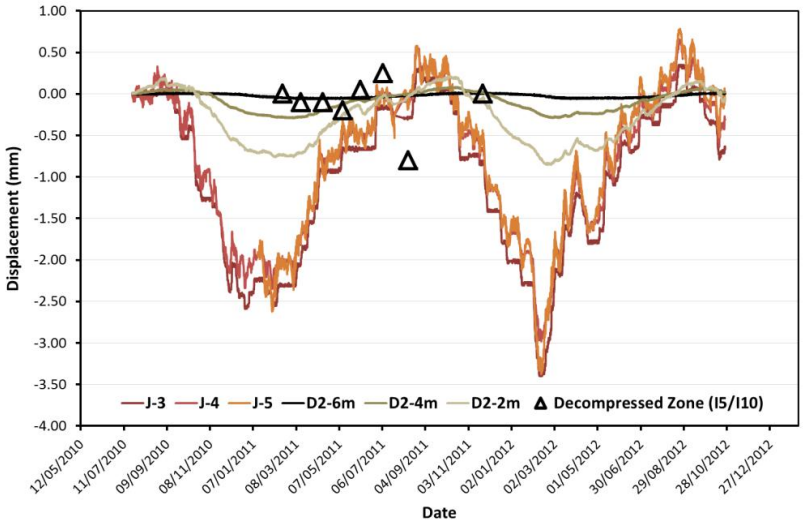

(b)

Figure 3-22. Displacements of Decompressed Zone; a) Comparison with Jointmeters and Distometer D1; b) Comparison with Jointmeters and Distometer D2

The convergence measurements of the decompressed zone have a similar behaviour than jointmeters data, with expansion when the temperature is low; however these vertical displacements present maximum values of 0.2mm. With a length of 5.65 meters between the points I5 and I10, the thermic strains are close to 4e-3 %.

The low strains of decompressed zone may be explained by the vertical stress (weithgt) on the area. The vertical movements are restricted by confined stress in this direction. Actually the large strains in the roof may be due to is loaded by its own weight only (arc effect).

Finally, the Figure 3-23 indicates how changes the shape of the cavern with the temperature cycles.

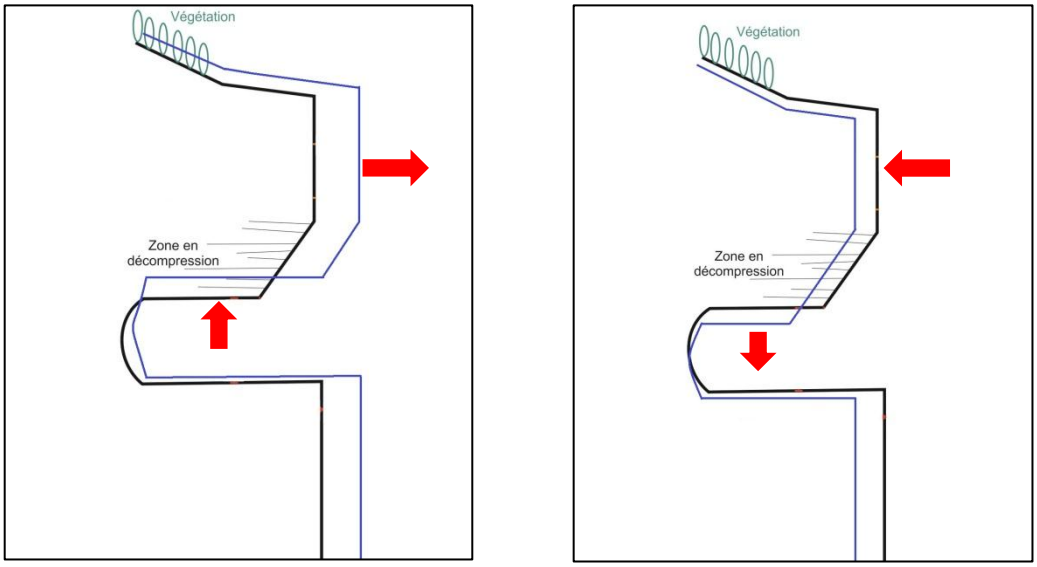

(a) **(b)**

Figure 3-23. Deformations of the cavern against thermic cycles; a) High temperatures; b) Low temperatures

To support the interpretation of instrumentation, a numerical has been built to analyze the mechanisms at the basis of the time evolution of displacements and, particularly, of its relationship with temperature.

3.2 LABORATORY TESTING

A series of laboratory test was performed by the *Laboratoire Régional des Ponts et Chaussées de Toulouse*. The samples were obtained from block of debris of failure in 2010 and the types of test are:

- 10 uniaxial compressions test (Figure 3-24).
- 5 Brazilian tensile strength test (Figure 3-25).
- 3 Triaxial compression tests with confining pressure of 2.5, 5 and 10 MPa.

The waves of compression and shear were measurements through 2 blocks on perpendicular direction of stratification planes and the porosity was obtained too.

Figure 3-24. Uniaxial compression test.

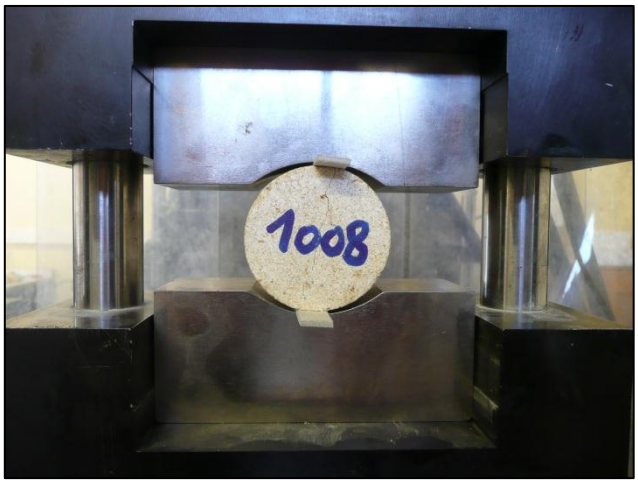

Figure 3-25. Brazilian tensile strength test.

The results of these tests are presented in Table 3-1 and its value will be discussed below.

Respect to traxial test a transition between the brittle to ductile behaviour is observed with the increment of confining pressure (Figure 3-26). Even though it may be thought that this transition would only be of interest to geologist considering rocks subjected to the high pressures and temperatures that exist at great depth, there can be engineering circumstances where the transition is of importance. This is because the confining pressure associated with the brittle-ductile transition varies with the rock type and is low in some cases. As mentioned Hudson & Harrison (1997), perhaps the most important aspect of this phenomenon is to understand the reason why the stress – strain curves take the form they do. In compression the rock tends to fracture perpendicular to the least principal stress, i.e. parallel to the major principal stress. Consequently, the application of even a small confining pressure has a significant effect on inhibiting the development of these cracks, and indeed, the mechanism of crack formation, which gradually changes to shearing as the confining pressure is increased.

Table 3-1. Results of test.

No. Test	ρ (kg/m³)	V_p (m/s)	V_s (m/s)	σ_c (MPa)	σ_{tb} (MPa)	σ_c (MPa)		E (GPa)	ν
						σ_1	σ_3		
998	2434	5420	3014			80.20	5.0	42.58	0.15
999	2399	5046	2814			81.68	10.0	46.97	0.12
1000	2444	5029	2875			65	2.5	38.35	0.15
1008					6.18				
1009					5.49				
1010					5.10				
1011					4.16				
1012					5.44				
1013	2317	4757	2736	47.44					
1014	2437	3269	2675	47.28					
1015	2340	4684	2731	53.73					
1016	2400	4786	2537	59.71					
1017	2290	4681	2561	35.44					
1018	2423	5241	2675	31.30					
1019	2367	4884	2572	63.29					
1020	2373	4431	2427	51.68					
1021	2368	4078	2376	43.20					
1022	2377	4153	2571	40.65					

No. Test	ρ_d (kg/m³)	ρ_s (kg/m³)	n_c (Porosity)	n_t (Total Porosity)	W (%)
Bock No1	2356	2868	0.111	0.179	4.7
Bock No2	2329	2835	0.113	0.179	4.8

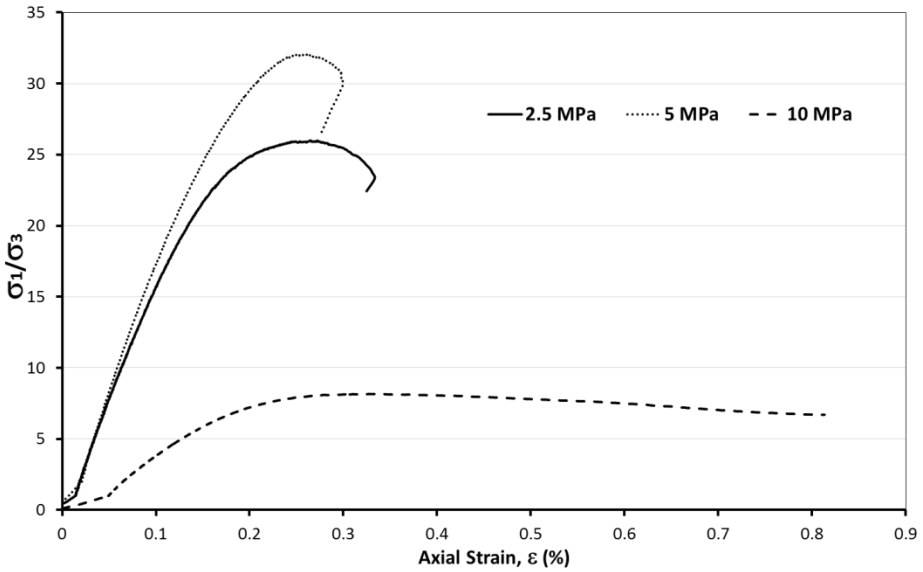

Figure 3-26. Brittle – ductile behavior of the rock.

The tensile strength results present similar values with a mean of **5.27 MPa** and low standard deviation of **0.66 Mpa**. The small variation in the result can be explained through the relation between type of test and volume evaluated with the probability density curves (Figure 3-27).

There are two particular tests of the uniaxial compression study identified like No 1017 and No 1018; its low values may be due to this samples have a discontinuities (Figure 3-24). While the mean value is **47.37 MPa,** the uniaxial compression of samples affected by discontinuity has value of **30 MPa** approximately.

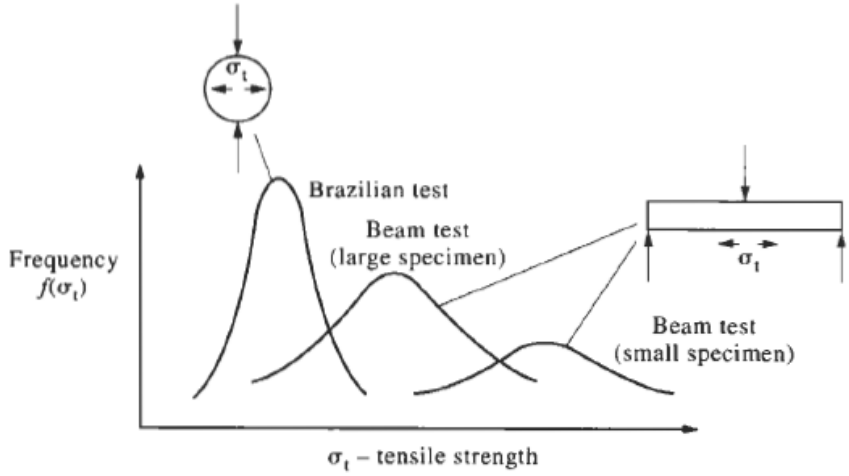

Figure 3-27. Tensile strength variation as a function of specimen volume and type of test. Hudson & Harrison 1997.

The high porosity corresponds to geological context and has an influence in the low tensile strength of the rock and low water content guarantee that the influence of water is negligible; therefore the problem can be defined like a Thermo-Mechanical coupling.

The Hoek-Brown empirical failure criterion presents a good agreement with the strength data from the uniaxial and triaxial compression test (Figure 3-28). Although the strength of intact rock was compared, the criterion has the capacity to estimate the rock mas strength through of parameters related with the degree of fracture and the degree of "particle interlocking". The formulation of a elastoplastic model based on this criterion will be presented in the Chapter 4.

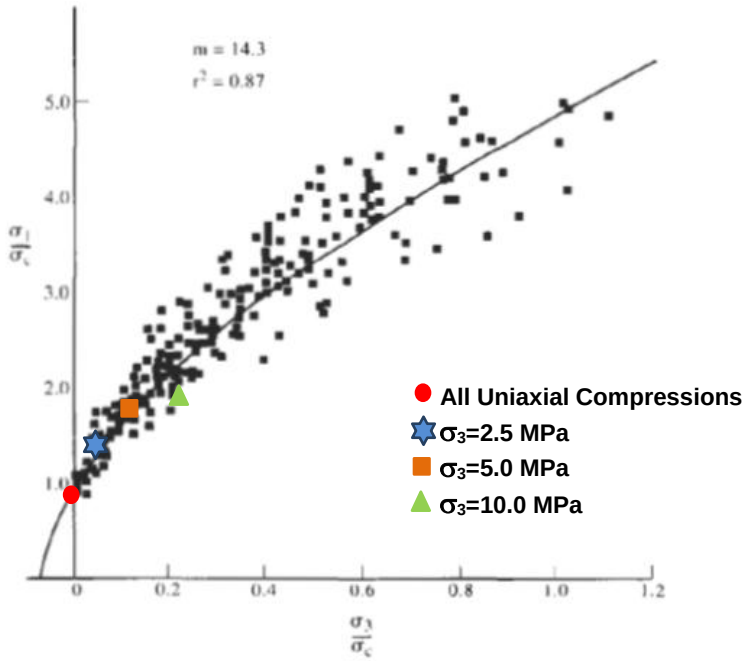

Figure 3-28. Normalized failure Envelope for Sandstone. Hoek & Brown 1980

A qualification of the rock massif was made by the *Laboratoire Régional des Ponts et Chaussées de Toulouse.* The Rock Mass Rating is the parameter selected. The Table 3-2 shows the different values of the proprieties used to estimate the RMR. The value of RQD was an estimate from the experience about the massif.

Table 3-2. RMR qualification

Property	**Value**	**Note**
Uniaxial Compression strength	47.4 MPa	4
RQD	75-90%	17
Separation of discontinuities	200-600 mm	10
Discontinuity Roughness	Roughness surfaces	25
Water	Dry	15
RMR		71

From the original Hoek- Brown failure criterion (1980) several proposed to integer the rock massif characteristic has been proposed. To generate a numerical modelling of the cliff a modulus against deformations is necessary. Hoek-Brown (1997) proposed a computation of the modulus that involves the massif characteristics

$$\mathrm{E(Gpa)} = \left(1 - \frac{D}{2}\right) \sqrt{\frac{\sigma_c}{100}}\; 10^{\frac{GSI-10}{40}} \qquad \textbf{Eq. 3-1}$$

The parameter *GSI* with the structure of the massif (e.i. intact, blocky or disaggregated) and *D* is a disturbance factor. The modulus of rock massifs is 31 GPa that is lower that the intact rock modulus.

3.3 REFERENCES

Hoek, E. & Brown, T. 1980. Empirical strength criterion for rock masses. *Journal of the Geotechnical Engineering Division,* Vol. 106, No. 9. 1013-1035.

Hoek, E. & Brown, T. 1997. Practical estimates or rock mass strength. *Int. J. Rock Mech. & Mining Sci. & Geomechanics Abstracts. 34 (8), 1165–1186.*

Hudson, J. & Harrison, J. 1997. Engineering Rock Mechanics. *Elsevier Ltd.*

Laboratoire Régional des Ponts et Chaussées de Toulouse., 2011. La Roque Gageac - Endommagement de la roche sous l'effet des cycles thermiques. *Report Project DOSMS*

Laboratoire Régional des Ponts et Chaussées de Toulouse., 2011. La Roque Gageac – Note Technique Système d'Instrumentation. *Report Project DOSMS*

Ruiz, D., Vaunat, J., Samat, S. & Virely, D. 2012. Thermo-mechanical modelling of an aerial cavern under climatic actions. *4$_{th}$ Workshop CODE_BRIGHT*, Barcelona.

Vaunat, J., Samat, S., Alonso, E., Ruiz, D., Martin, E., Saillard, M., Virely, D. & Darrozes, J. 2012. Slope responses under climatic actions. Model and case interpretation. *In preparation*.

Sofianos, A. 1996. Analysis and desing of an underground hard rock voussoir beam roof. *Int. J. Rock Mech. & Mining Sci. & Geomechanics Abstracts. 33 (2), 153–166.*

CHAPTER 4

CONCEPTUAL FRAMEWORK OF ANALYSIS

The previous Chapters has been demonstrated the existence of a strong coupling between the atmospheric actions and instability events of the rock-cliff. Simulating this type of coupled phenomena isn't a straightforward task. The processes controlling atmosphere conditions include effects of radiation and heat exchange, moist processes (clouds and precipitation), air mass motion and interactions with earth ground components (free surface water, vegetation, outcropping soils and rocks). Figure 4-1 presents a schematic overview of these different effects and their interactions. From general point of view, the soil-atmosphere interaction is due to boundary fluxes like a precipitation (P), evaporation (E) and solar radiation (Rn) that affect the balance in the thermo-hydro-mechanical formulation of the porous media (Noilan & Planton, 1989). The Thermo-hydro-mechanical processes in soils and rocks fulfilled basic laws of physics.

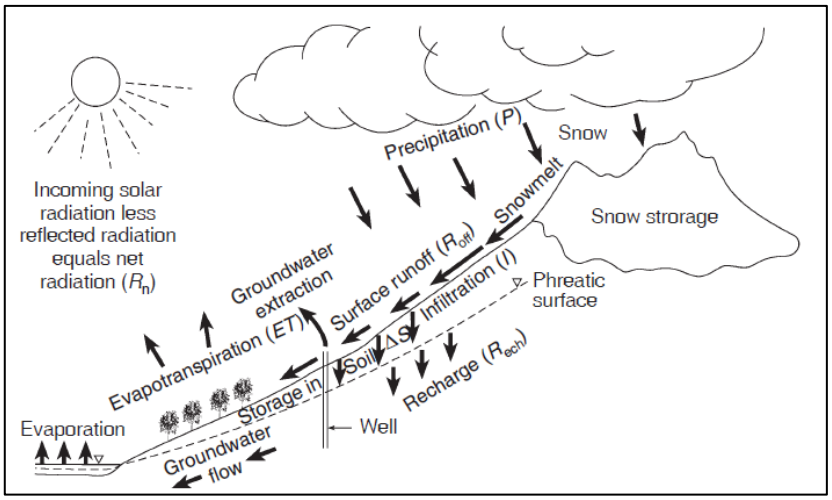

Figure 4-1. Scheme of mass and energy interactions between ground, vegetation and atmosphere. Blight 1997

Involve all variables in a modelling can be a complex work due to the great amount of data are required, however if the real problem requires all interactions, these must be integrated in a consistent formulation. The engineering challenge is to find the main atmospheric actions that interfere in the problem; this work requires experience, a quality field observations and good understanding of the problem.

Now, the description of the modelling climatic actions and Thermo-Hydro-Mechanical formulation will be described. The general formulation of both items will be mentioned, but simplifications due to the problem characteristics are commented. The overall formulations are reported by Olivella *et al.* 1994 and Vaunat *et al.* 2012.

The predominant atmospheric action on the cliff is the temperature and its time evolution that generates thermal strain cycles. The fact that the cliff is considered dry implies that coupled phenomenon is Thermo-Mechanical which is a specific part of the general framework.

The main postulate for the modelling work is that the temperature on the surface of the ground isn't the atmospheric temperature. The energy flux on the ground surface is related with the net radiation from the sun. The key aspect about the numerical work is can reproduce this flux as a boundary condition on the rock-cliff surface and then to analyse the conduction phenomena into the porous medium.

4.1 MODELLING CLIMATIC ACTIONS

Most of the energy received by the earth is due to solar radiation, which is a shortwave radiation. On top of the atmosphere, the incident solar radiation (R_a) depends on the energy emitted by the sun (1376 W/m^2), the current distance between the sun and the earth, the latitude and the current time. Atmosphere and clouds further reflect and absorb part of the incident radiation and the irradiance at the level of the ground R_g is significantly lower than R_a. The ratio R_g / R_a depends essentially on the cloudiness, absorptivity of the atmosphere (increased by the presence of greenhouse gas) and travel length across the atmosphere that depends in turn on latitude and current time. The energy absorbed by clouds and atmosphere is released upward back to the space and downward in direction to the earth under the form of long wave radiation. The ground receives thus both types of radiation in a ratio that depends on latitude, cloudiness and current time.

Part of the total energy received by the ground is reflected according to the albedo of the surface (ratio between incident and reflected radiation). The albedo depends on surface characteristics (i.e. material or color). Because the albedo is typically two times lower for water (~10%) than for soils and rocks, it is influenced by the degree of saturation of the ground surface. For the case *La Roque Gageac*, the cliff may present a high value of albedo, due to the rock has a particular color white.

The remaining part of energy is temporarily stored in the soil. One share of it is further released to the atmosphere by conduction, advection and long wave radiation. The conductive flux is driven by the difference in temperature between soil and atmosphere. Advection includes heat transported by mass fluxes crossing the ground surface: air, liquid water and vapour. The long wave radiation is controlled by the emissivity of the soil. The advective fluxes has importance in

a problems that includes the saturated/unsaturated soil, however with the consideration of dry state of the rock, these fluxes don't exist. The part not released to the atmosphere gives the amount of energy stored in the soil that controls the change of soil temperature. In a classical relation between atmosphere and the ground the energy stored in the soil provides the heat available for water vaporisation, therefore it is the key variable controlling the evaporation flux, however in this specific case the energy stored influences only the thermal strains of the solid phase of the rock.

For cases when the water phase exists, *Vaunat et al.* (2012) explain the evaporation phenomenon through the soil surface. In bare grounds, evaporation is driven by the difference of water potential between the atmosphere (where water exists only under the form of vapour) and the soil (where liquid water co-exists with vapour in unsaturated conditions). The other major contribution to the hydric balance of the vadose zone is the net infiltration, difference between the precipitation and the run-off. Precipitation intensity, soil permeability, slope inclination and rugosity are the main factors influencing the amount of superficial water running down on slope surface and thus not entering into the ground. The balance between evaporation and net infiltration gives the change of soil water content for the period under consideration.

In vegetalized area, the hydric balance between the soil and the atmosphere is strongly modified by plant evapotranspiration. Roots take water from the soil and transmit it to the leafs that release it to the atmosphere under the form of vapour. Vegetation acts thus as a bypass to soil surface and deepens the zone of direct evaporation, which results in a powerful enhancement of soil water extraction. Water and energy available in the soil, leaf and root density, root depth, vegetation type, atmosphere relative humidity and temperature are many factors influencing the transpiration rate. Even though, the top of the cliff have thick vegetation, the stability problem is related with the vertical surface of the ground and hence this factor is not taking account.

For the purpose of geotechnical modelling, the complexity of atmospheric processes and vegetation life systems cannot be represented as such, but realistic simplifications of their effects on the ground should be implemented. In that perspective, the present model does not handle the atmosphere as a whole but introduces its effect as a special boundary condition prescribed at soil surface. This condition retrieves all the fluxes crossing the surface (solar short wave and long wave radiation, water infiltration, wind) and the state of the atmosphere above the slope (temperature, relative humidity and air pressure). In the same spirit, vegetation is modelled through a non linear sink term of water mass, applied up to some depth below the slope surface (root zone). The atmosphere/vegetation boundary condition defined in that way should moreover be consistent with the continuum formulation considered to model the underlying ground, which should thus account for thermo-hydro-mechanical coupled processes. The formulation is shortly summarized hereinafter with emphasis on the different couplings accounted for and their relationships with surface fluxes due to soil-atmosphere-vegetation interactions.

The total energy flux will be described now and then how these affect the porous media.

4.1.1 Total Energy Flux

As mentioned previously, the surface energy balance is used generally to estimate evapotranspiration, which is primarily one of energy consumption. Although evapotranspiration doesn't occur in the surface cliff, to understand the overall energy fluxes across the ground surface is necessary, because the simplifications can be checked.

The Figure 4-2 shows the different components of the fluxes across the soil surface. The net radiation flux for the surface (incoming solar and diffuse sky radiation, less reflected radiation and outgoing long-wave terrestrial radiation) is presented in the Figure 4-2a, the sensible heat flux for the air (the heat causing changes in temperature of the air) and the latent heat flux of evaporation (heat causing evaporation or condensation at the soil surface). From the algebraic sum of different energy fluxes the soil heat is obtained from temperature gradients in the soil, together whit the specific heat capacity for the soil at its current water content. All fluxes are measured in W/m^2 (or J/m^2), and the convention is that incoming radiation and absorbed heat fluxes are positive.

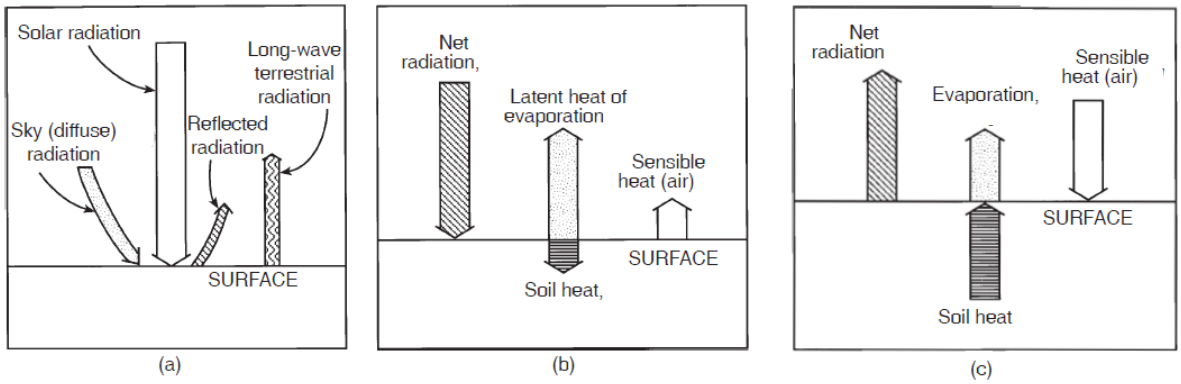

Figure 4-2. Components of the radiation balance at a soil surface; a) Incoming and outgoing radiation; b) Radiation interchange during the day; c) Radiation interchange at night day. Blight 1997

As pointed by Blight (1997), for long-term measurement at fixed location weather stations are available that automatically measure and record all parameters necessary to evaluate an energy balance (Figure 4-3); however this completed instrumentation is rarely at sites where the academic investigation is not performed.

The case *La Roque Gageac* doesn't have a complete atmospheric instrumentation and the only solution is to calculate the different components of energy balance. From the Atmospheric boundary condition module in CODE_BRIGHT (2011), the total energy flux j_e thus writes as follows:

$$j_e = R_n + H_s + H_c \qquad \textbf{Eq. 4-1}$$

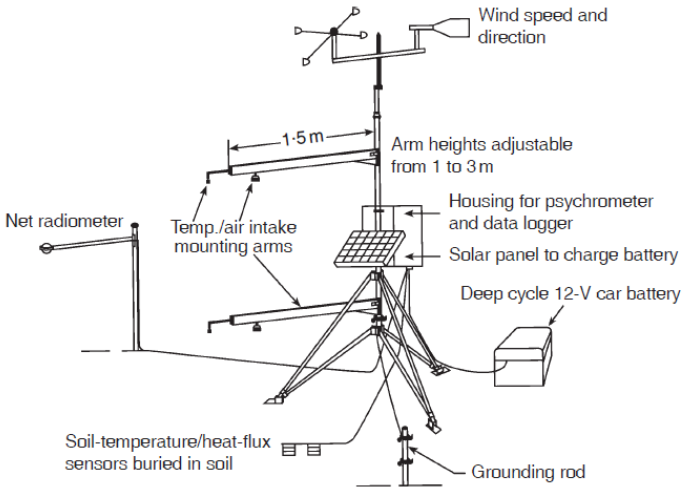

Figure 4-3. Apparatus for automatic measurements and logging of energy balance components . Blight 1997

The convective or latent heat flux H_c is calculated taking into account the internal energy of liquid water, vapour and air:

$$H_c = h_v\left(E + j_w^g\right) + h_{la}\left(P + j_w^l\right) + h_{a0}\, j_a \qquad \textbf{Eq. 4-2}$$

where h_v, h_{la} and h_{a0} are the free energy of vapour, liquid water and air, respectively. These three properties depend on the temperature.

The sensible heat flux H_s is, calculated through an aerodynamic diffusion relation:

$$H_s = \frac{k^{\acute{e}} v_a \phi}{\ln\left(\frac{z_0}{z_a}\right)^2} \rho_{ga} C_a \left(T_a - T\right) \qquad \textbf{Eq. 4-3}$$

where C_a is the specific heat of the gas.

Noilan & Planton (1988) propose the net radiation as a sum of absorbed fractions of the incoming solar radiation and atmospheric infrared radiation:

$$R_n = (1 - A_l)R_g + \varepsilon R_a - \varepsilon\sigma T^4 \qquad \textbf{Eq. 4-4}$$

where Rg is the direct solar short wave radiation, Ra is the long wave atmospheric radiation, A_l is the albedo, ε is the emissivity and σ is the Stefan-Boltzman constant (5.67×10^{-8} J s^{-1} m^{-2} K^{-4}).

Both the albedo and emissivity are considered function of the liquid saturation S_l:

$$A_l = A_d + \left(A_d - A_w\right)\left(S_l^2 - 2S_l\right) \qquad \textbf{Eq. 4-5}$$

$$\varepsilon = 0.9 + 0.05 S_l \qquad \textbf{Eq. 4-6}$$

where Ad and Aw are the dry and wet albedos.

The long wave atmospheric radiation Ra depends on the atmospheric temperature and absolute humidity according to an empirical relation:

$$R_a = \sigma T_a^4 \left(0.605 + 0.048\sqrt{1370\rho_{va}}\right) \quad \textbf{Eq. 4-7}$$

The calculation of the solar radiation Rg takes into account the time of the day and the year according to:

$$\begin{cases} R_g = \dfrac{\pi R_G}{2d_s}\sin\left(\dfrac{(t - t_m + 0.5d_s)\pi}{d_s}\right) & \text{if } t_m - 0.5d_s \le t \le t_m + 0.5d_s \\ \mathrm{R_g} = 0 & \text{otherwise} \end{cases} \quad \textbf{Eq. 4-8}$$

where ds is the time span between sunrise and sunset and tm is the time at noon and R_G is the daily solar radiation calculated by an empirical relation:

$$R_G = \int_{t_m - 0.5d_s}^{t_m + 0.5d_s} R_g\, dt = R_A\left(0.29\cos\lambda + 0.52 I_n\right) \quad \textbf{Eq. 4-9}$$

where λ_l is the latitude and In is the cloud index (= 1 for a clear sky, = 0 for a completely clouded sky) and R_A is the daily solar radiation in absence of atmosphere:

$$R_A = S_0 r_s \left[\frac{d_d}{\pi}\cos\lambda\cos\delta\sin\left(\frac{\pi d_s}{d_d}\right) + d_s\sin\lambda\sin\delta\right] \quad \textbf{Eq. 4-10}$$

where S_0 is the solar constant (= 1367 $J.m^{-2}.s^{-1}$), r_s is the relation between the average distance between the earth and the sun and that of a given moment, d_d is the duration of a day (= 86400 s) and δ is the declination of the sun.

The values of d_s, r_s and δ are calculated as follows:

$$d_s = \frac{d_d}{\pi}\,\mathrm{acos}\left(-\tan\lambda_l \tan\delta\right) \quad \textbf{Eq. 4-11}$$

$$\begin{aligned} r_s = 1.00011 &+ 0.034221\cos\left(2\pi\frac{t - t_0}{d_a}\right) + 0.00128\sin\left(2\pi\frac{t - t_0}{d_a}\right) \\ &+ 0.000719\cos\left(4\pi\frac{t - t_0}{d_a}\right) + 0.000077\sin\left(4\pi\frac{t - t_0}{d_a}\right) \end{aligned} \quad \textbf{Eq. 4-12}$$

$$\delta = -\delta_{\max}\sin\left(2\pi\frac{t - t_s}{d_a}\right) \quad \textbf{Eq. 4-13}$$

where d_a is the duration of a year (= 365.241 days = 3.15568×107 s), t_0 is the time of January 1st, t_s is the time when autumn starts (September 21st for the northern hemisphere) and δmax is the maximum declination of the sun (= 0.4119 rad = 23.26°).

If the rock-cliff is considered dry, the latent heat flux is cero, thus the total energy flux is the net radiation and latent heat flux.

$$j_e = R_n + H_s \qquad \textbf{Eq. 4-14}$$

The dependence of external temperature on the computation of net radiation generates a variation of the radiation fluxes during the year, with higher values in summertime that wintertime. The above characteristic is a realistic behaviour demonstrated by Cui et al. 2008 (Figure 4-5) and Blight 1997 through instrumentation data.

In short-time measurements (Figure 4-4) a correlation between the air temperature and solar radiation is not clear, but in long-time observations (Figure 4-5) a tendency is observed. The computation of the *La Roque Gageac* will be composed by a lot years of temperatures, thus the correlation between this values must be taking into account.

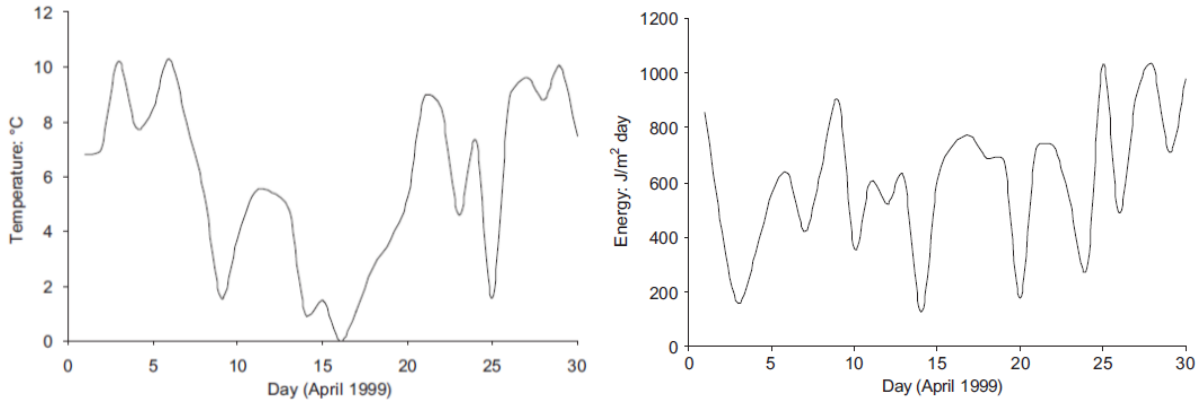

Figure 4-4. External temperature and solar radiation measurements at Boissy-le-Châtel, France, during April 1999. Cui *et al.* 2005

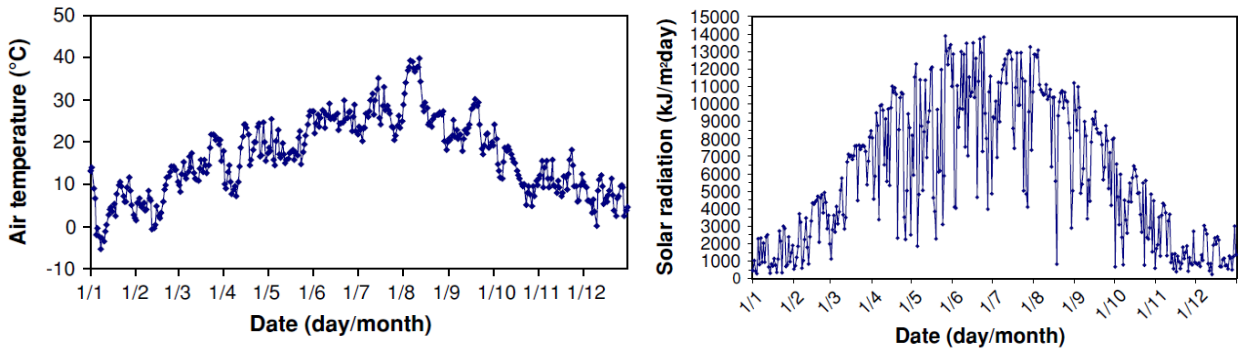

Figure 4-5. External temperature and solar radiation measurements at Boissy-le-Châtel, France, during 2003. Cui *et al.* 2008

From the temperature data of the meteorological station *Sarlat-La Canéda* and parameters reported in the Table 4-1, the net radiation flux on the rock-cliff was calculated (Figure 4-6).

Table 4-1. Parameters to Net Radiation Computation

Albedo	0.4
Emissivity ε	0.9
Cloud index I_n	0.55
La Roque Gageac Latitude λ	0.7821 Rad

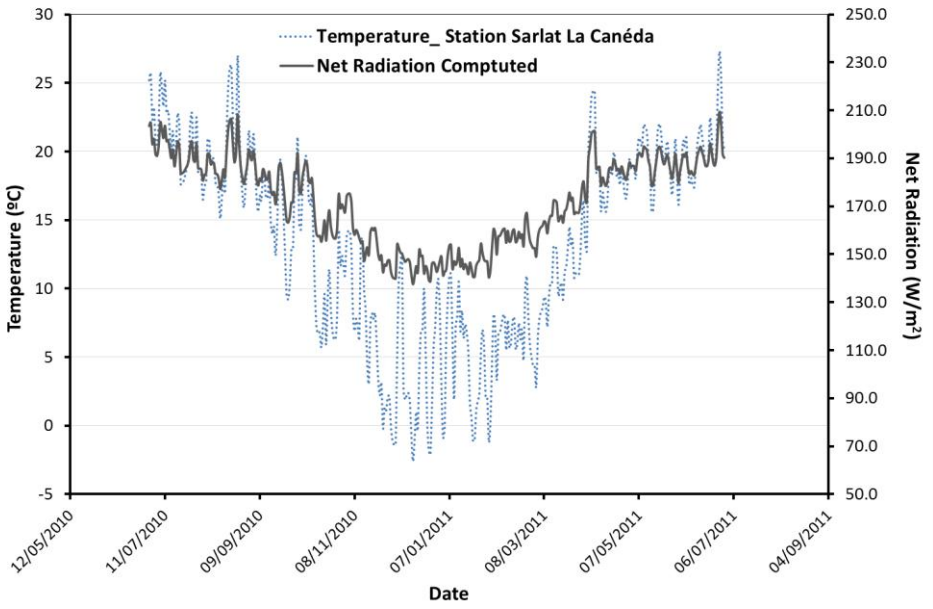

Figure 4-6. Net radiation in *La Roque Gageac* computed from meteorological data of Sarlat-La Canéda

With the flux boundary condition established, the modelling of the coupled phenomena will be completed with the physic laws that control the response of the porous media under this external action.

4.2 THERMO-HYDRO-MECHANICAL COUPLING IN SOILS AND ROCKS

Thermo-hydro-mechanical processes in soils and rocks fulfilled basic laws of physics, in that case the conservation laws of mass, energy and the stress equilibrium.

In unsaturated conditions, soils and rocks are composed by a solid skeleton filled by two fluid species: air and water. The latter are present either in liquid state (liquid water and dissolved air) or under the form of gas (vapour and dry air).

The overall coupling processes is presented by Olivella *et al*. 1994 and Vaunat *et al*. 2012, where the balance equations (water mass, air mass and energy) with the stress equilibrium are formulated.

As a problem was defined like a Termo-Mechanical coupling, the conservation of energy and stress equilibrium are explained only. However the Figure 4-7 shows the complexity of formulation and the lot of existing couplings

It is interesting to note that the use of material derivative D/Dt in Eq. 4-15 allows expressing air and water fluxes as relative to the velocity of the soil skeleton, which maintains the validity of the formulation in case of rapid soil movements[1]. Further details of the formulation can be find in *Olivella et al.* 1994.

The conservation law of energy expresses the balance of heat in a unit volume of soil. The heat contained in the volume is the sum of the heat contained in the solid, liquid and gas phase, which can be expressed, under simple assumptions, as the product of temperature by mass specific heat (including latent heat). The flux of heat entering in or going out from the medium is due to four components: conductive heat, controlled by Fourier's law and medium thermal conductivity, and heat convected by liquid water, dry air and vapour (Table 4-2). For the case *La Roque Gageac* the heat convected by liquid water, dry air and vapour doesn't interfere.

$$\frac{De}{Dt} + div(j_e) = f_e \qquad \textbf{Eq. 4-15}$$

e = energy of solid grain $((1-n)\rho_s e_s)$
+ energy of liquid water $(nS_r\rho_w e_w)$
+ energy of vapour $(nS_r\rho_v\omega_g e_v)$
+ energy of dry air $(n(1-S_r)\rho_a\omega_a e_a)$

e_s = energy of an unit volume of solid grain $(C_s T)$
e_w = energy of an unit volume of liquid water $(C_w T)$
e_v = energy of an unit volume of vapour $(C_v T + e_{v0})$
e_a = energy of an unit volume of dry air $(C_a T)$

j_e = conductive flux (i_c)
+ flux of dry air energy $(\rho_a\omega_a q_g e_a)$
+ flux of liquid water energy $(\rho_w q_l e_l)$
+ flux of vapour energy $((i_v + \omega_g\rho_v q_g)e_g)$

f_e = source/sink term of energy

Balance equations are completed by the stress equilibrium:

$$div\ \sigma + \rho g = 0 \qquad \textbf{Eq. 4-16}$$

Total stress σ is related to soil or rock deformation through the concept of effective stress that controls the behaviour of the materials. In saturated soils, this is Terzaghi's effective stress σ' = σ – pw that prevails. In saturated rocks with low compressibility (compressibility of the rock C close to that of the minerals Cm), deformation caused by a given change of water pressure is lower than that due to the same change in total stress. The concept of effective stress includes therefore a less and unity factor that weights the pore pressure, and often expressed as C / Cm,. Whatever is the concept considered, σ depends on water pressure and deformation and this dependency is the first main coupling between stress equilibrium and water mass balance, which allows modelling consolidation process in saturated conditions.

[1] This formulation assumes that gradients of apparent densities convected by the solid phase are negligible.

Table 4-2 . Heat fluxes in unsaturated soils or rocks.

Fluxes	Within the soil or rock		Prescribed flux at the boundary
	Governing law	Theoretical expression	
Heat	Convection by liquid water +	$j_{ew} = \rho_l q_l C_w T$	$\bar{j}_{ev} = \bar{\rho}_{l0}\bar{q}_l C_w \bar{T}_0$ if $\bar{q}_l$ inflow $\bar{j}_{ev} = \rho_l \bar{q}_l C_w T$ if $\bar{q}_l$ outflow
	Convection by dry air +	$j_{ea} = \omega_a \rho_g q_g C_a T$	$\bar{j}_{ea} = \bar{\omega}_{a0}\bar{\rho}_{g0}\bar{q}_g C_a \bar{T}_0$ if $\bar{q}_g$ inflow $\bar{j}_{ea} = \omega_a \rho_g \bar{q}_g C_a T$ if $\bar{q}_g$ outflow
	Convection by vapour +	$j_{ev} = \omega_v \rho_g q_g (C_v T + e_{v0})$	$\bar{j}_{ev} = \bar{\omega}_{v0}\bar{\rho}_{g0}\bar{q}_g (C_v \bar{T}_0 + e_{v0})$if $\bar{q}_g$ inflow $\bar{j}_{ev} = \omega_v \rho_g \bar{q}_g (C_v T + e_{v0})$if $\bar{q}_g$ outflow
	Conduction	$i_c = -\lambda \nabla T$	$\bar{i}_c = \bar{q}_{T0} + \bar{\gamma}_T (T - \bar{T}_0)$

Temperature changes cause deformation of soils or rocks that modify the stress state, highlighting the one main coupling between stress equilibrium and heat balance equation (Figure 4-7). The relationship between the temperature and mechanical changes has a particular coupling due to it is usually in one direction. The imposition of heat on porous media generates thermal strains; however as a pointed Gens *et al.* 2007, coupling from mechanical to thermal behaviour is negligible. The changes of porosity are so slight that they do not affect thermal conductivity.

Besides the main couplings, there exists secondary coupling through the dependency of material and interstitial fluid parameters on state variables (Tab. 2). Bulk properties of soil or rock, like thermal conductivity and heat capacity, are controlled by the relative mass ratios of soil, air and water present in the medium. As such, their values depend on all variables that modify solid, air and water contents: medium deformation, temperature, air and water pressures.

Fig. 2 provides a full picture of all the possible couplings considered by the formulation to model the THM response of soil and rocks, distinguishing between main and secondary couplings (in italic). It must be emphasized that all the couplings are not necessarily active, depending of the characteristics of the problem under consideration (i.e. the case *La Roque Gageac*)

The proposed THM formulation allows applying several conditions at the boundaries of the problem: on the one hand, displacement, temperature, liquid and gas pressures and, on the other hand, forces and fluxes.

As far as concerns boundary heat fluxes, they are totally determined by prescription of external heat flux ($\bar{q}_{T0}$), temperature (T_0) and boundary impedance against heat conduction ($\bar{\gamma}_T$). Indeed, T_0 provides the additional information necessary to compute the heat flux convected by liquid water, dry air and vapour (Tab. 2), whereas $\bar{\gamma}_T$ (T - T_0) gives the conductive flux due to temperature difference across the boundary $\bar{q}_{T0}$ models any additional flux directly applied at the boundary of the problem.

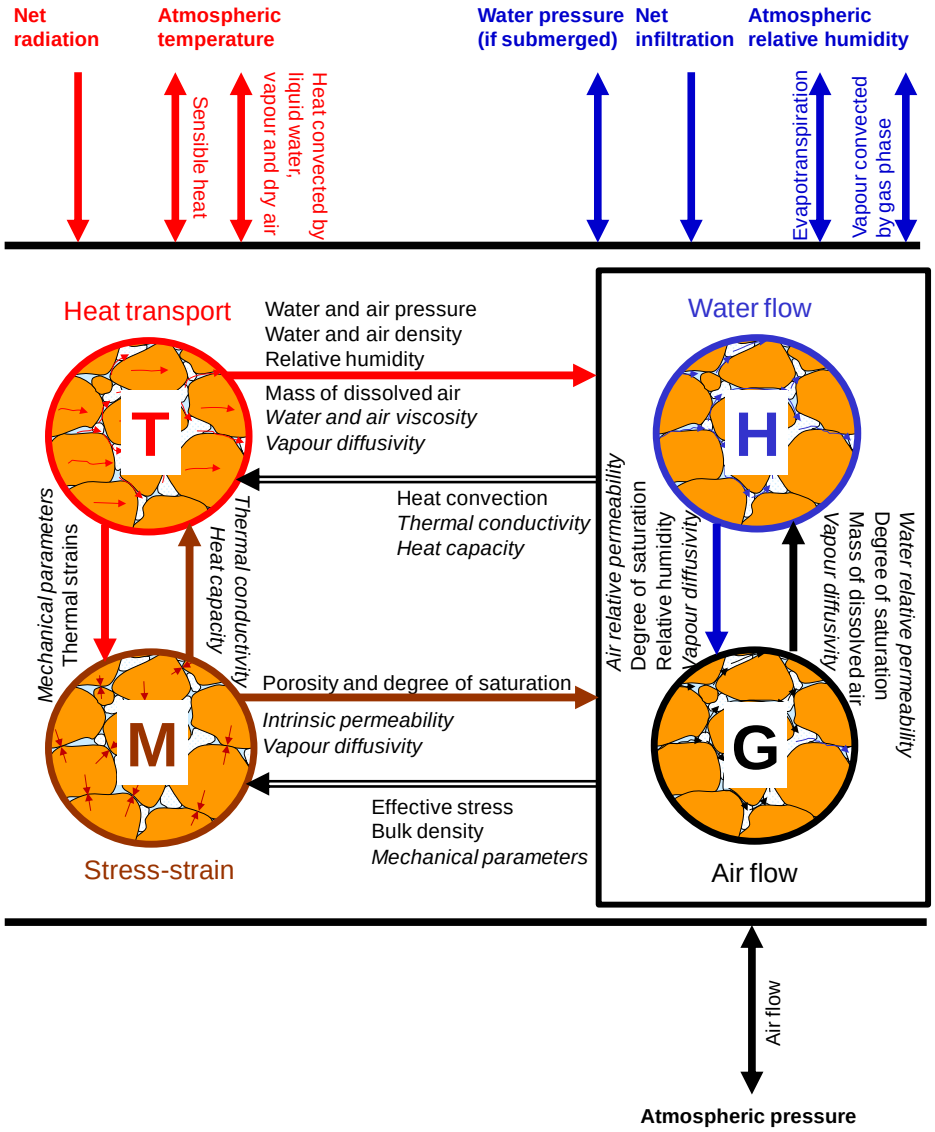

Figure 4-7. Overall THM coupling in soils and rocks (secondary couplings are in italic).

Table 4-3 . Parameters THM dependencies (secondary couplings).

Relationship	Parameters	Dependency on			
		T	p_w	p_a	ε
Fourier law	Thermal conductivity	x	x	x	x
Storage term in heat	Heat capacity	x	x	x	x
Generalized Darcy's law	Intrinsic permeability				x
	Air relative permeability		x	x	
	Water relative permeability		x	x	
	Air viscosity	x			
	Water viscosity	x			
Fick's law	Vapour diffusion coefficient	x	x	x	x
	Dissolved air diffusion coefficient	x	x	x	x
Stress-strain relationship	Mechanical parameters	x	x	x	x

With the conduction heat as the main phenomenon in the case *La Roque Gageac*, the medium thermal conductivity (λ) and heat capacity (Cs) of the solid phase are the factors that control a temperature change into the rock.

Finally, the theoretical framework to model the case is completed with the formulation of Hoek-Brown yield criterion (*CODE_BRIGHT User's Guide 2010)*.

After the failure state the elastic behaviour is described by:

$$d\sigma_{ij}^{M} = D_{ijkl}^{eM}\left(d\varepsilon_{kl}^{M} - \delta_{kl}\frac{ds}{K_s^M} - d\varepsilon_{kl}^{P}\right) \qquad \textbf{Eq. 4-17}$$

σ_{ij}^{M} are the stress prevailing at clay particles contact, D_{ijkl}^{eM} is the mechanical elastic stiffness matrix of the clay, $d\varepsilon_{kl}^{M}$ are the strains corresponding to the clay matrix deformation (external strain), K_s^M is the bulk modulus against suction changes (if any), $d\varepsilon_{kl}^{P}$ are the plastic strains of the clay matrix. The external strains $d\varepsilon_{kl}^{M}$ are are given by thermal expansion coefficient:

$$\Delta\varepsilon_v = 3b_s\Delta T \qquad \textbf{Eq. 4-18}$$

where b_s is the linear thermal expansion coefficient for the medium.
The stress space is limited by the next yield function:

$$F^p = \frac{4\sin^2\left(\theta^M - \frac{\pi}{6}\right)}{R_c^M} J^{M2} - \frac{2\ m^M \sin\theta^M}{\sqrt{3}}\ J^M - m^M(p^M + p_t^M) \geq 0 \qquad \textbf{Eq. 4-19}$$

$p_t^M = R_c^M/m^M$ is the rock tensile strength, R_c^M the uniaxial compressive strength, m^M a parameter defining the shape of the parabolic yield criterion. R_c^M depends on suction and temperature following the law:

$$R_c^M\ (s,T) = R_c^M(0)\left[(1-r^M)\exp\left(-\beta^M s\right) + r^M + K_{MT}(T - T_{ref}\right] \qquad \textbf{Eq. 4-20}$$

The plastic potential is considered associated and it is given by:

$$G^p = \frac{4sin^2\left(\theta^M - \frac{\pi}{6}\right)}{R_c^M} J^{M2} - \frac{2m^M sin\theta^M}{\sqrt{3}} J^M - m^M(p^M + p_t^M) \qquad \textbf{Eq. 4-21}$$

A softening law is introduced through the following dependency of tensile strength on the plastic strain:

$$p_t^M = \frac{R_{c0}^M}{m^M}\left[1\text{-}(1-\alpha^M)\frac{\max(\varepsilon_1^{pM}, \xi_r^M)}{\xi_r^M}\right]^2 \qquad \textbf{Eq. 4-22}$$

R_{co}^{M} is the intac strength, α^{M} a brittleness parameter, ε_{1}^{pM} is the major principal plastic strain, ξ_{r}^{pM} the accumulated major principal strain at which the residual strength is reached. α^{M} is related to the intact and residual uniaxial compression strength by the formula:

$$\alpha^{M} = \sqrt{\left(\frac{R_{cres}^{M}}{R_{c0}^{M}}\right)^{2} + \frac{2}{3} m^{M} \frac{R_{cres}^{M}}{R_{c0}^{M}}} \qquad \textbf{Eq. 4-23}$$

$\alpha^{M} = 1$ means perfect plasticity, $\alpha^{M} = 0$ total degradation (residual strength equal to 0). $\alpha^{M} > 1$ means hardening plasticity while $\alpha^{M} < 1$ means softening plasticity.

4.3 REFERENCES

Blight, G. E., 1997. Interactions between the atmosphere and the earth. *Géotechniqu*e 47, No. 4, 713-767. 37$_{th}$ Rankine Lecture

Cui, Y. J., Lu, Y. J., Delage, P. & Riffard, M., 2005. Field simulation of in situ water content and temperature change due to ground-atmospheric interactions. *Géotechniqu*e 59, No. 4, 355-363.

Cui, Y. J. & Zornberg, J. G. Y. J., 2008. Water balance and evapotranspiration monitoring in geotechnical and geoenvironmental engineering. *Geotechnical and Gelogical Engineering*, Vol 26, Issues 6. 4, 783-798.

Departament d'Enginyeria del Terreny, Cartogràfica i Geofísica (2010). *CODE_BRIGHT User's Guide.* Polytechnic University of Catalonia (UPC) – Barcelona Tech. Spain.

Gens, A., Vaunat, J., Garitte, B. & Wileveau, Y. 2007. In situ behaviour of a stiff layered clay subject to thermal loading: observations and interpretation. *Géotechnique* 57, No. 2, 207–228

Noilhan, J., & Planton, S., 1988. A simple parameterization of land surface processes for metereological models. *Monthly Weather Review*, Vol 117, 536-589.

Olivella, S., Carrera, J., Gens A. & Alonso, E.E. 1994. Non-isothermal Multiphase Flow of Brine and Gas through Saline media. *Transport in Porous Media*, 15: 271-293.

Ruiz, D., Vaunat, J., Samat, S. & Virely, D. 2012. Thermo-mechanical modelling of an aerial cavern under climatic actions. *4$_{th}$ Workshop CODE_BRIGHT*, Barcelona.

Saaltink, M., Pereira, J.M. & Samat, S. 2011. Atmospheric Boundary Conditions Module in *CODE_BRIGHT.*

Vaunat, J., Samat, S., Alonso, E., Ruiz, D., Martin, E., Saillard, M., Virely, D. & Darrozes, J. 2012. Slope responses under climatic actions. Model and case interpretation. *In preparation*.

CHAPTER 5

NUMERICAL ANALYSIS

To support the interpretation of the instrumentation, a set of numerical models has been built to analyze the main mechanisms of interaction between the atmosphere and the rock-cliff. The objective of the modelling is to provide further evidence on the representativity of the assumptions made during the basic interpretation of the measurements and to reproduce quantitatively by the model the time evolution of the displacement and temperatures.

The model build to simulate the response of the cliff at *La Roque Gageac* will consider only the first year of instrumentation data (July 2010 to June 2011), as the numerical work was performed before the data of the second year become available. The analysis of longer time series is however contemplated as a continuation of the work. Despite the consideration of one seasonal cycle only, the modelling will provide keys about the following issues:

- The strong relationship between the atmospheric action and the mechanical response on the cliff.
- The central point played by the temperature in the mechanical response of the cliff, which justifies the use of a Thermo-Mechanical only.
- The key effect of radiation flux on the temperature pattern within the massif.
- The reversible nature of most displacement, except for the response of the residual beam within the cavern.
- The pattern of response of the discontinuities under thermal cycles, characterized by opening during temperature decrease.

The numerical analysis is composed by five models:

- A two dimensional model (2D) considering the atmosphere daily temperature and the solar radiation (both short- and long-wave) as boundary conditions and an elastic law for the mechanical behaviour of the rock.

- A two dimensional elastic model considering the daily temperature only as boundary condition. The objective of this model is to highlight the importance of the net radiation for the thermal field inside the cliff.

- A two dimensional model (2D) considering the full thermal load (air temperature and solar radiation) and an elastoplastic law based on the Hoek & Brown criterion for the mechanical behaviour of the rock.
- A three dimensional model (3D) considering an elastic law for the material, the full thermal load and more detailed aspects about the real shape of the troglodyte cavern. This modelling aims at, on the one hand, at validating the 2D model, and, on the other hand, at demonstrating the low stress carried by the beam because of the development of an arching effect.
- A 2D model of the rock beam only where the differents discontinuities are modelled by joint elements.

The models were developed by means of a Finite Element Method code (CODE_BRIGHT) developed by the Department of Geotechnical Engineering and Geo-Sciences (UPC) (Olivella *et al*., 1994) to model Thermo-Hydro-Mechanical problems in geological media. The rock-atmosphere interaction is modelled by a special boundary condition recently implemented in the code recently (Saaltink *et al.* 2011).

5.1 NUMERICAL MODELS

5.1.1 Elastic model 2D with net radiation flux

The two dimensional (2D) models consider a vertical section of the cliff passing through the diaclasis shown in Figure 2-13. Massif boundaries (left and bottom in Figure 5-1a) have been set at 100 m from the cliff face and top, to avoid possible influence on the computation.

The mesh of the model (in plane strain condition) is composed by 1333 quadrilateral element and 1431 nodes. The geometry of the troglodyte cavern is reported in the Figure 5-2 and the output points correspond to the measurement points of the extensometers (2m, 4m and 6m from the cliff face). At this stage of the analysis, the model does not take into account the presence of discontinuities.

Equations of stress equilibrium and heat balance are solved in this case. As far as concerns initial conditions (Figure 5-1b), a constant temperature equal to 14 ºC is imposed in all massif. The initial stress state follows a lithostatic distribution with K_0 = 3 at the top and K_0 = 2.5 at the bottom (vertical stress equal to the weight of the rock column and horizontal stress equal to vertical stress multiplied by the corresponding lateral earth-pressure coefficient K_0). Although there is not information about the current stress state in the massif, the previously approximation was made on the basis of data reported by Hudson & Harrison (1997) (see Figure 5-3). Fixed displacements are prescribed on the inner massif boundaries, whereas the top and face of cliff are considered unloaded (normal and shear force equal to 0). From a thermal point of view, an

adiabatic and isothermal (temperature equal to initial temperature) are considered for the left and bottom boundaries, respectively.

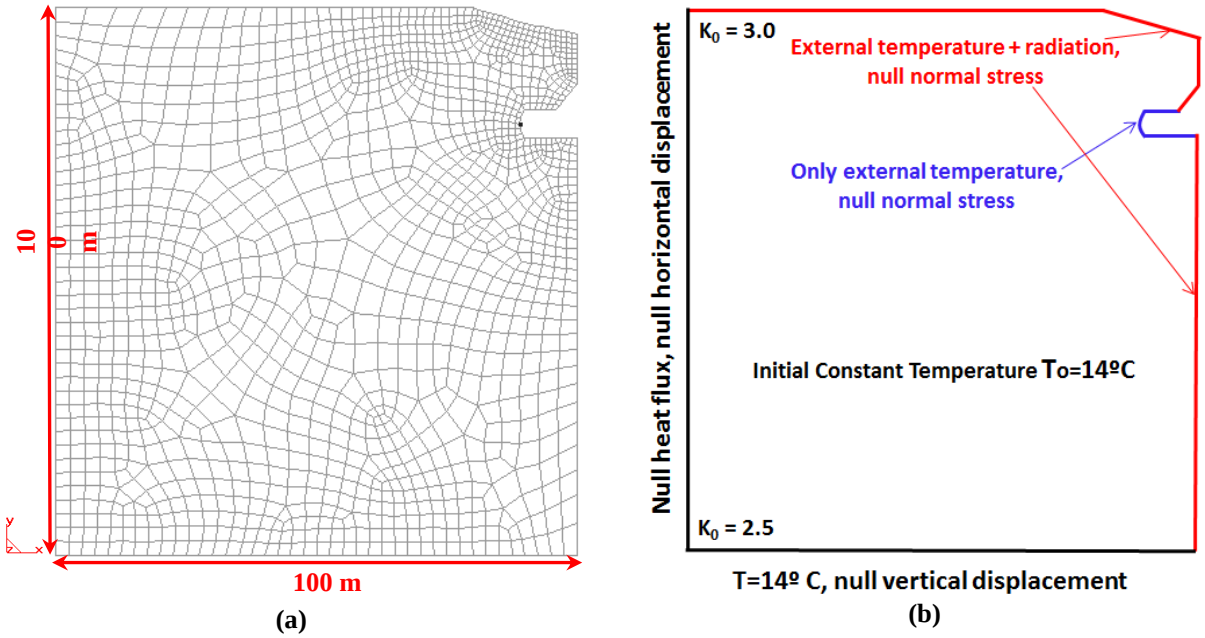

Figure 5-1. Elastic two dimensional model; a) Dimensions and mesh; b) Boundary and initial conditions

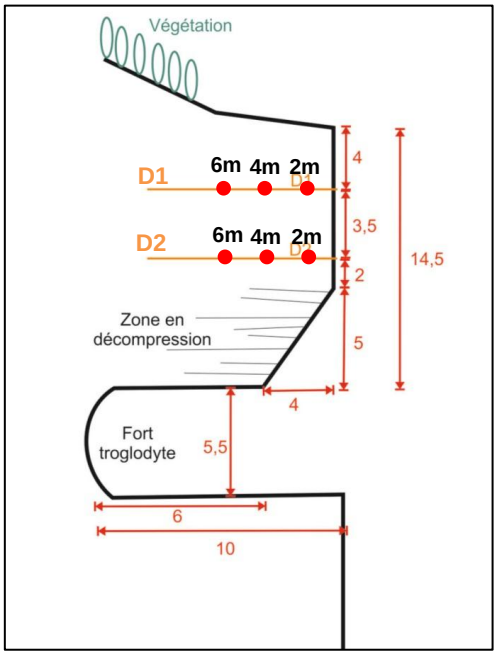

Figure 5-2. Dimensions of troglodyte cavern and output points of the model.

In a first step of the computation, the stress state is left equilibrating at constant temperature T_0 = 14ºC in order to capture the perturbation caused by the presence of the cavern. In a second step, a climatic condition, including daily atmospheric temperature and solar short- and long-wave radiation is prescribed at the top and the face of the cliff. Because the cavern is not exposed to sun light and neglecting the (small) effect of radiation diffraction by cavern air, radiation

component is removed at the wall and the roof of the cavern and only the external temperature is imposed (Figure 5-1b) on these boundaries.

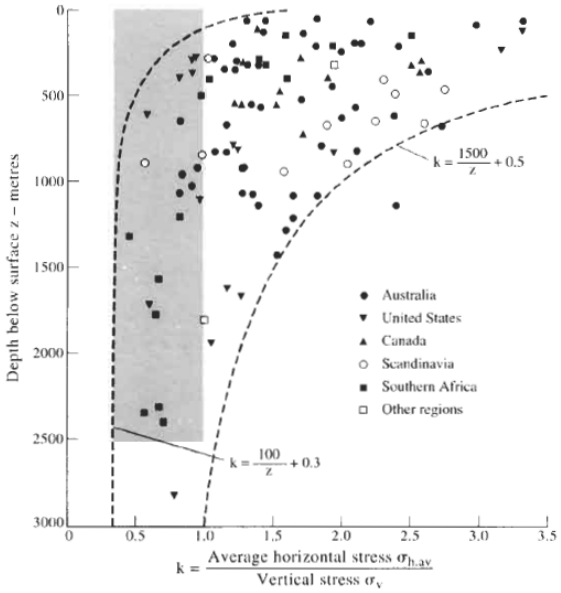

Figure 5-3. Collated worldwide in situ stress data: mean horizontal stress component (After Hoek & Brown, 1980). Reported by Hudson & Harrison

Temperature values are taken from the meteorological histogram registered at Sarlat station and shown in Figure 3-2. Net radiation fluxes are computed according to the framework presented in Chapter 4 (Figure 4-6).

The Table 5-1 shows the parameters used in this model for the rock. The mechanical response modelled using a linear elastic law with constant Young's modulus and Poisson's ratio, whose values have been assessed to reproduce the displacements in the extensometers. Young modulus value outcoming from the back-analysis is lower than that measured in laboratory tests on intact samples (Chapter 3). The discrepancy is attributed to the fact that the average field value accounts for the lower stiffness of massif discontinuities. For the same reason, the back-analyzed value of Poisson's ratio is slightly higher than that measured in traxial tests.

Table 5-1 . Parameters of the elastic model

Parameter	Values
Young's modulus	31000 MPa
Poisson's ratio	0.2
Heat capacity	1200 $J.kg^{-1}.K^{-1}$
Thermal conductivity	2.0 $W.m.K^{-1}$
Thermal linear expansion coefficient	6 10^{-6} $^oC^{-1}$

Heat conduction within the rock is totally controlled by material heat capacity and thermal conductivity. In absence of experimental tests, these parameters have been assessed by volume averaging of the heat capacity and thermal conductivity of the different minerals entering in the

rock composition. The coefficient of thermal linear expansion has been back-analyzed to adjust the deformations measured in the extensometers.

Because of the unavailability of previous meteorological records and to prevent spurious transient effects, the July 2010-June 2011 30 histogram has been prescribed reiteratively during 30 years to insure the reach of a stationary response of the massif. The Figure 5-4 shows the temperature evolution computed by the model during the thirty years at 2 m in the massif along the D1 borehole. At that point, the stationary response is obtained after 1100 days approximately. From that time on, the same cycle is reproduced annually (the fluctuations observed in the figure comes from a output artefact: because temperature results are output with a preset frequency, not all the minima or maxima appears in the output file). This result validates the capability of the model to reproduce consistently the same response under quasi-stationary climatic cycles.

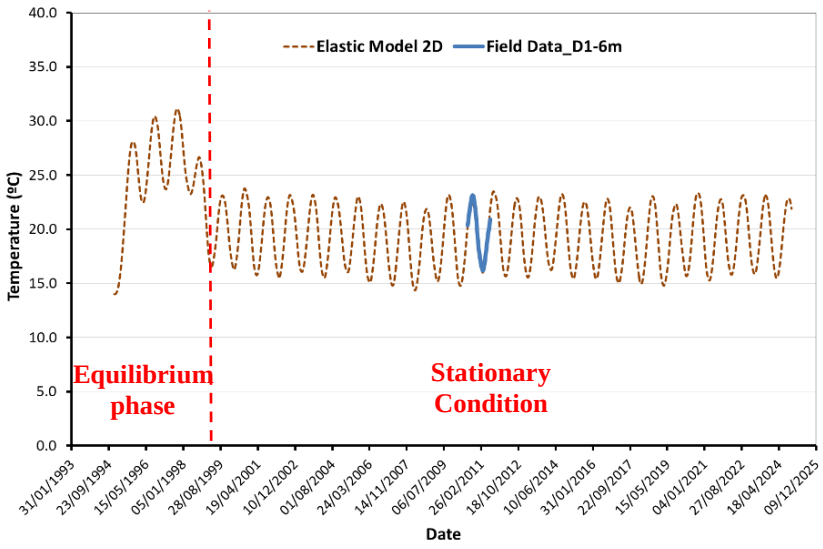

(a)

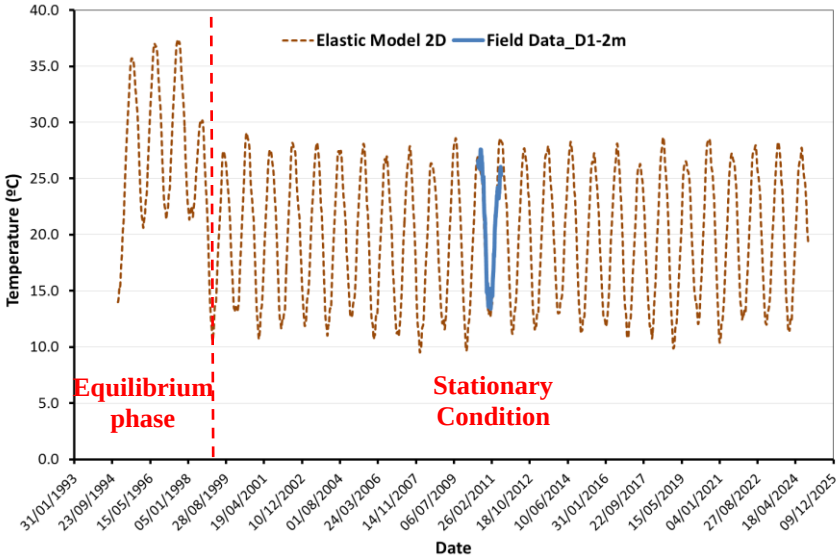

(b)

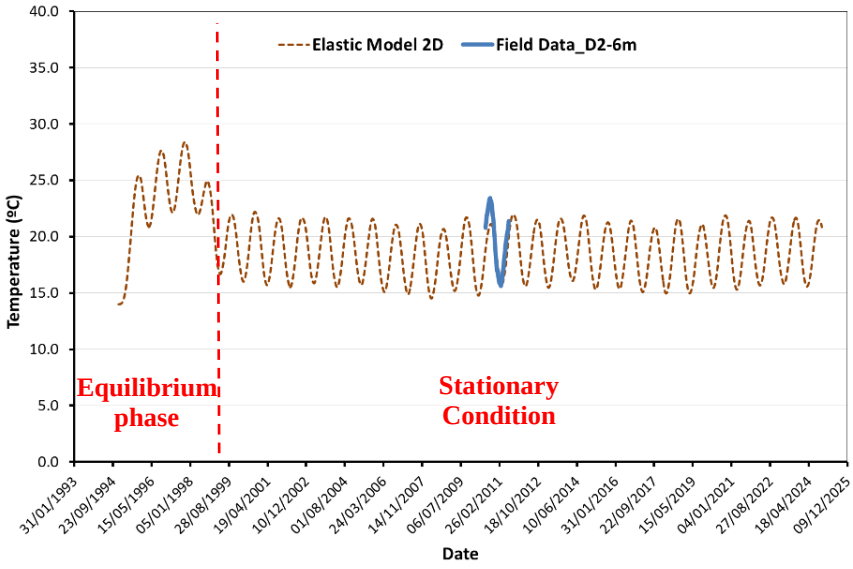

(c)

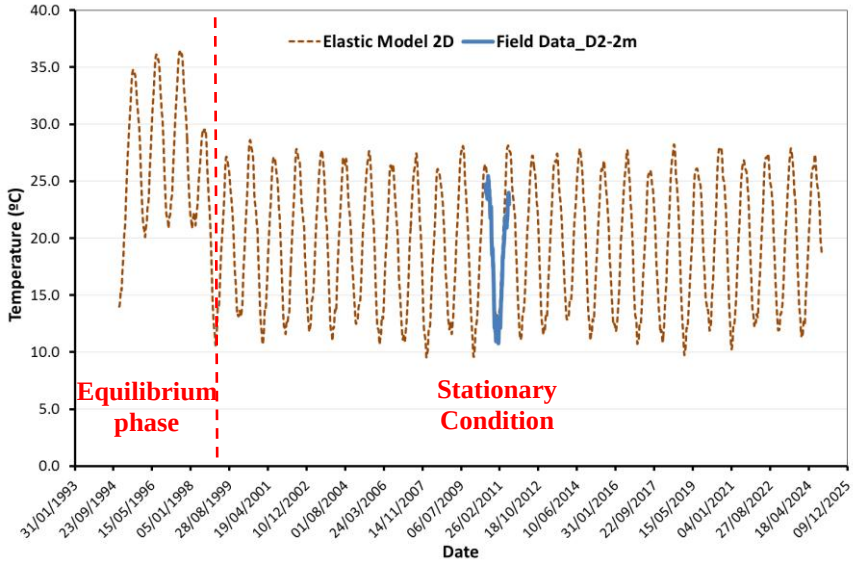

(d)

Figure 5-4. Temperature calculated in thirty thermal cycles (30 years); a) Distometer D1 at 6m; b) Distometer D1 at 2m; c) Distometer D2 at 6m; d) Distometer D2 at 2m.

In Figure 5-5 and Figure 5-6, measurements have been compared with the computed results in the quasi-stationary regime (July 2010 to June 2011). The comparison indicates an excellent agreement between the measurements and the simulation, which validates for this case the formulation and implementation of the atmospheric conditions and the choice for material thermal parameters. The right capture by the model of both temperature attenuation and signal shift between 2 and 6 m is particularly to be highlighted. A slight delay can however be observed between the data and the numerical results at extensometer D2-6m. It is attributed to the proximity of the cavern wall, where some radiation exists due to air diffraction, although the surface is not directly exposed to the sun. As diffraction is not accounted in the formulation of the atmospheric boundary condition, this effect cannot be reproduced by the model.

Figure 5-7 show isochrones of temperature at different times between July 2010 and June 2011. The smooth temperature gradient between the boundaries exposed to climatic actions and the bottom boundary, where a temperature of 14ºC is prescribed, indicates that the latter value is a reasonable guess of massif deep real temperature.

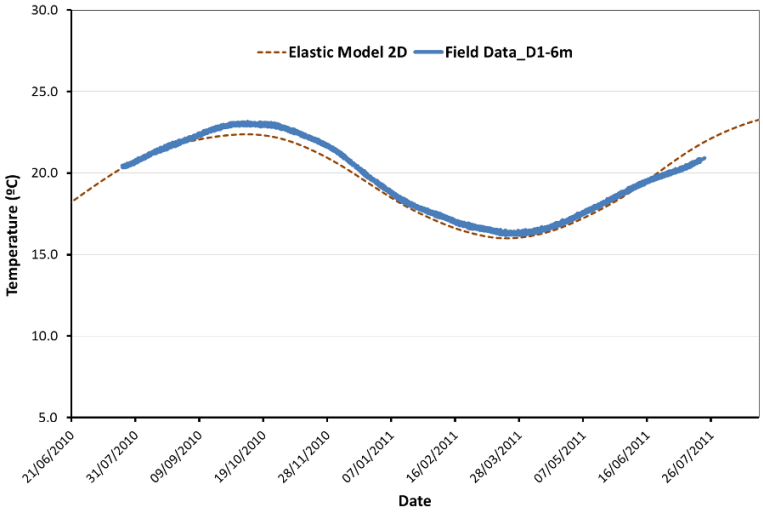

(a)

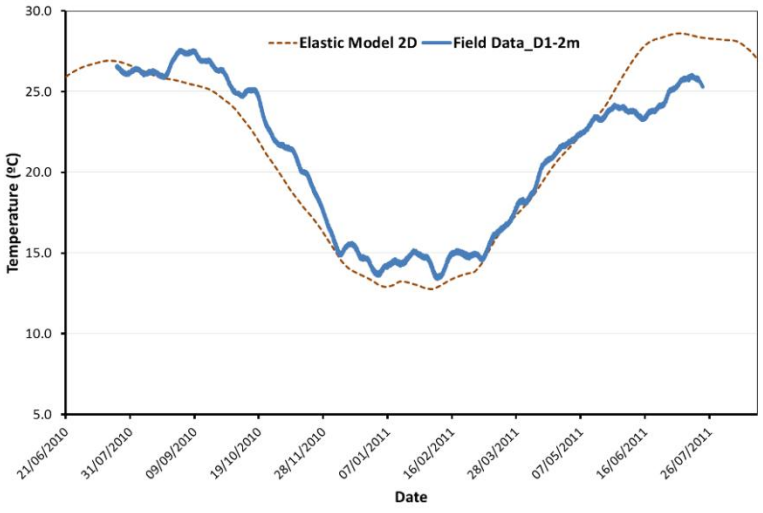

(b)

Figure 5-5. Temperatures at distometer D1 - Elastic model 2D with net radiation flux; a) 6 meters into the rock; b) 2 meters into the rock.

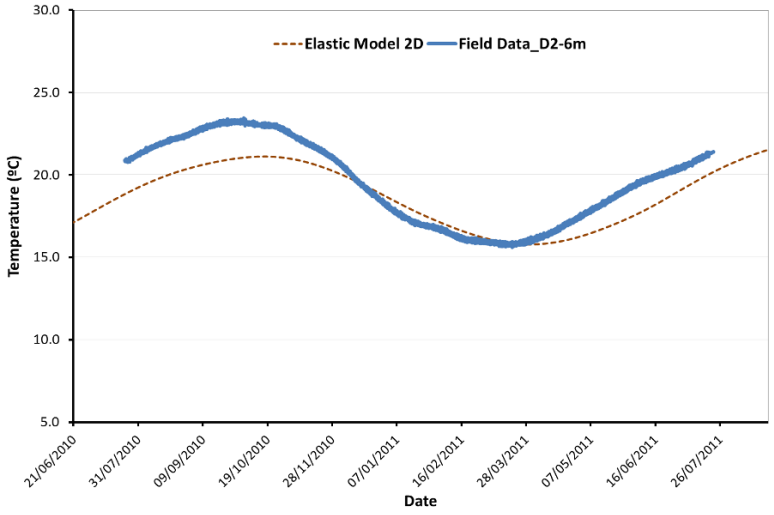

(a)

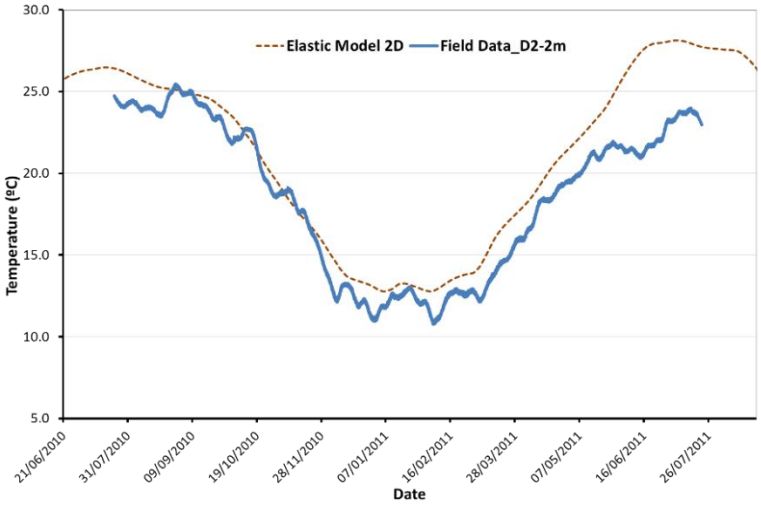

(b)

Figure 5-6. Temperatures at distometer D2 - Elastic model 2D with net radiation flux; a) 6 meters into the rock; b) 2 meters into the rock.

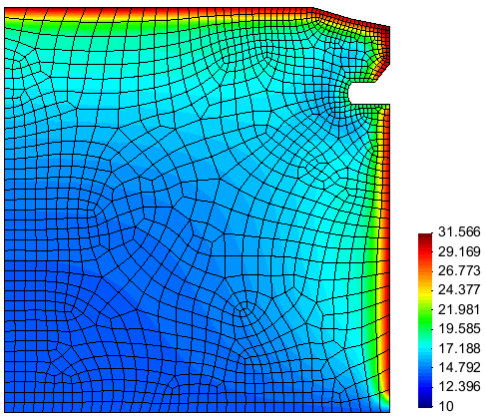

Date: 22/07/2010

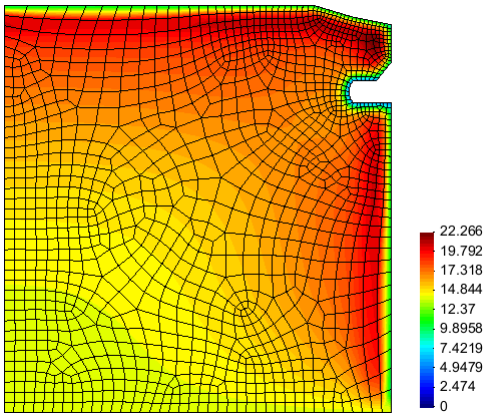

Date: 21/11/2010

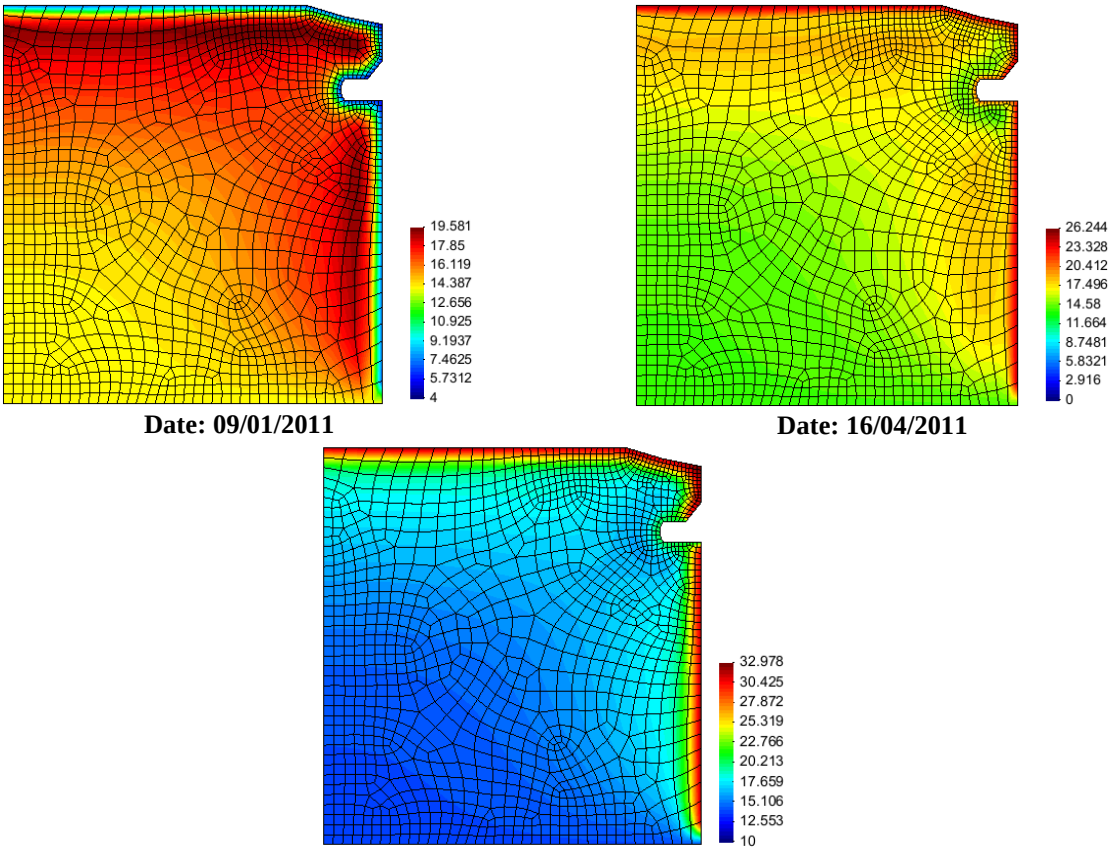

Figure 5-7. Graphical result of temperature - Elastic model 2D with net radiation flux

The time evolution of displacements in extensometers D1 and D2 are plotted in Figure 5-8. The curves adopt a pattern very similar to that of temperature, characterized by an initial transient phase of toward equilibrium that reaches quasi-stationnary conditions after 1100 d approximately. This confirms that, for this specific case, displacements are related exclusively to the change of temperature through the material thermal expansion coefficient.

A zoom over the instrumentation period is depicted in Figure 5-9 (for extensometer D1) and Figure 5-10 (for extensometer D2). It suggests that response of the model is quite similar to the real data, however a remarkable difference is presented in the displacement of distometer D1 at 2 meters. As described in the Chapter 3 this device shows a movement type block generated possibly by a discontinuity and with equal displacement at 4 m and 2 meters, but the numerical model represents a continuum solid under thermal effect, therefore the displacement is higher at near to surface. In conclusion the numerical model predicts displacements larger than those measured. The numerical response of the model at distometer site has the convention explained in the Chapter 3; negative values of the displacement mean a contraction of the rock.

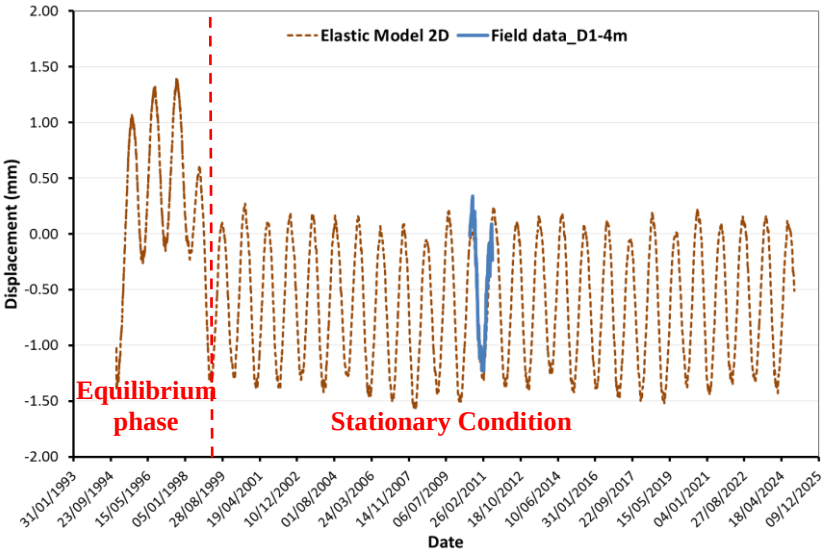
Elastic Model 2D
Field data_D1-4m
Displacement (mm)
Equilibrium phase
Stationary Condition
Date

(a)

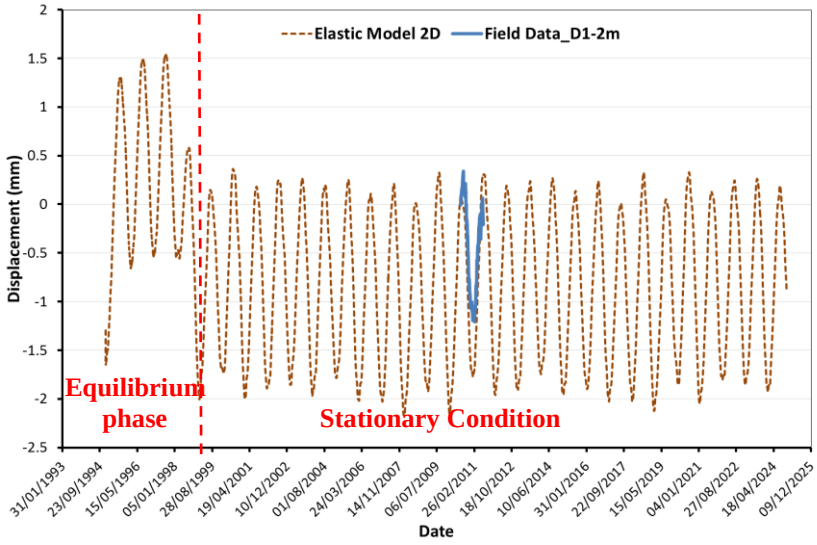
Elastic Model 2D
Field Data_D1-2m
Displacement (mm)
Equilibrium phase
Stationary Condition
Date

(b)

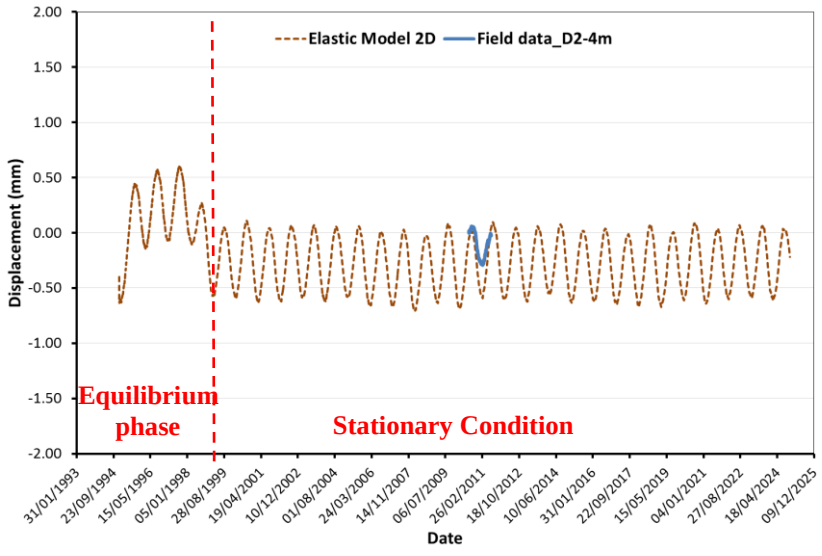
Elastic Model 2D
Field data_D2-4m
Displacement (mm)
Equilibrium phase
Stationary Condition
Date

(c)

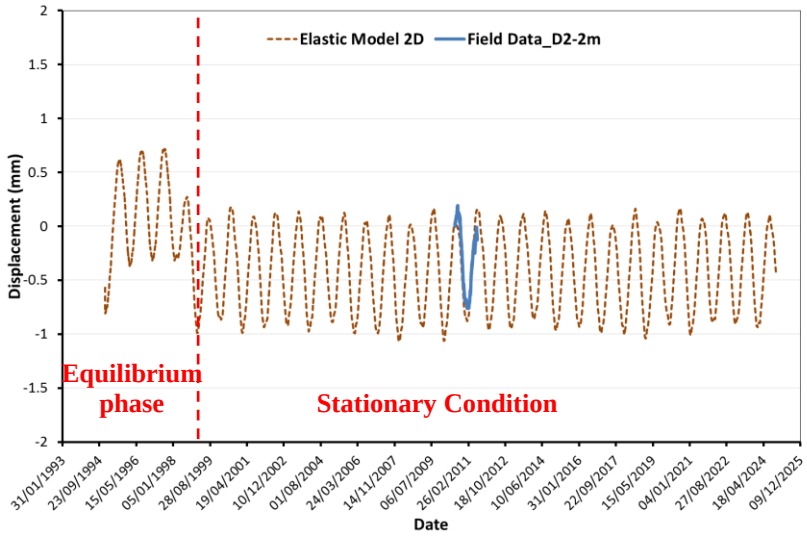

(d)

Figure 5-8. Displacement calculated in thirty thermal cycles (30 years); a) Distometer D1 at 6m; b) Distometer D1 at 2m; c) Distometer D2 at 6m; d) Distometer D2 at 2m.

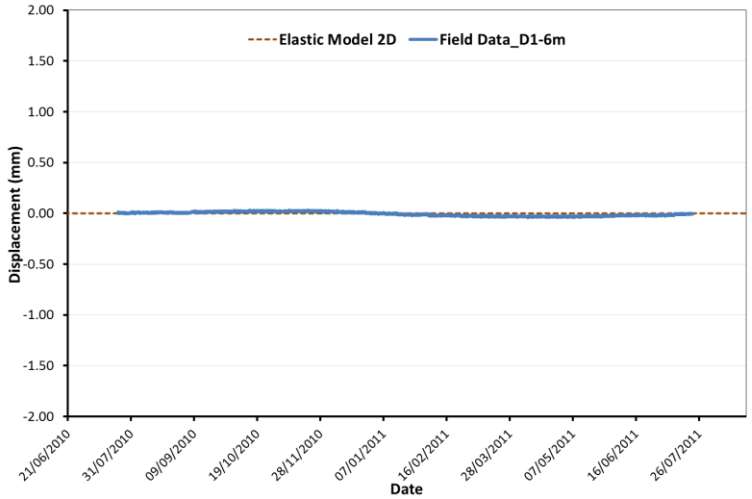

(a)

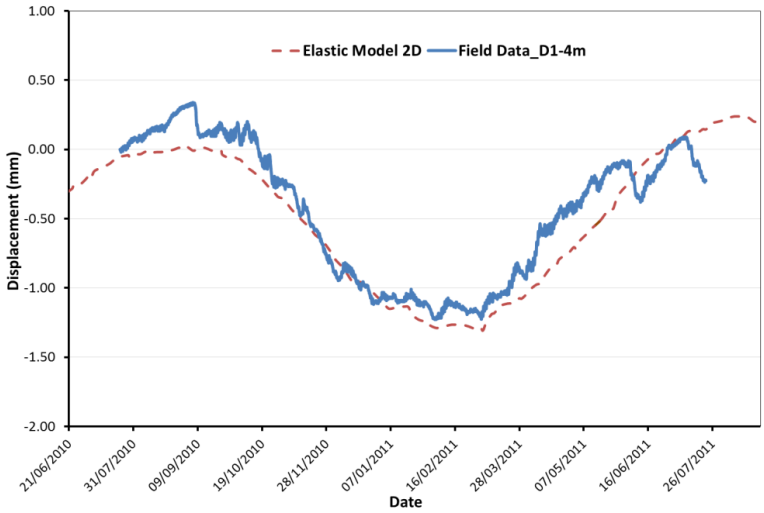

(b)

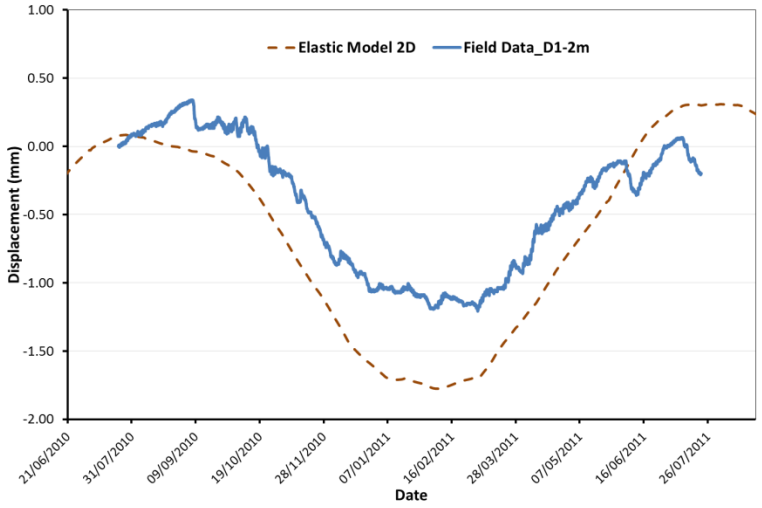

(c)

Figure 5-9. Displacements at distometer D1 - Elastic model 2D with net radiation flux; a) 6 meters into the rock; b) 4 meters into the rock; c) 2 meters into the rock.

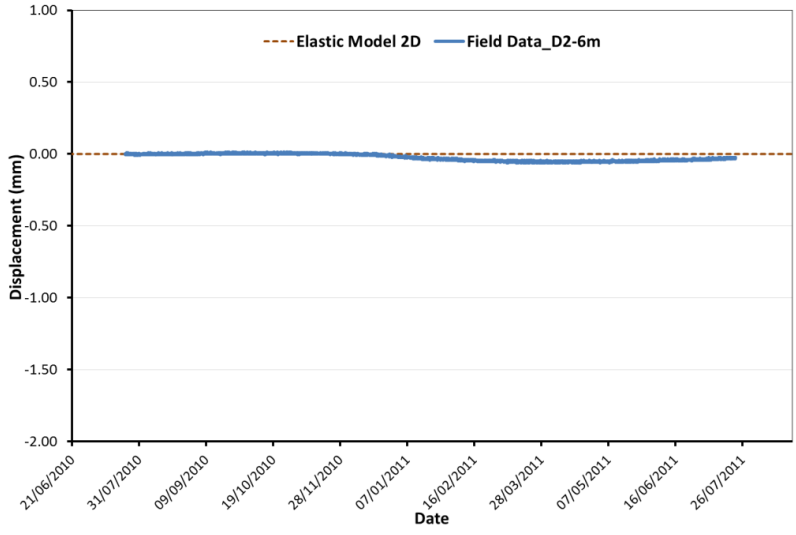

(a)

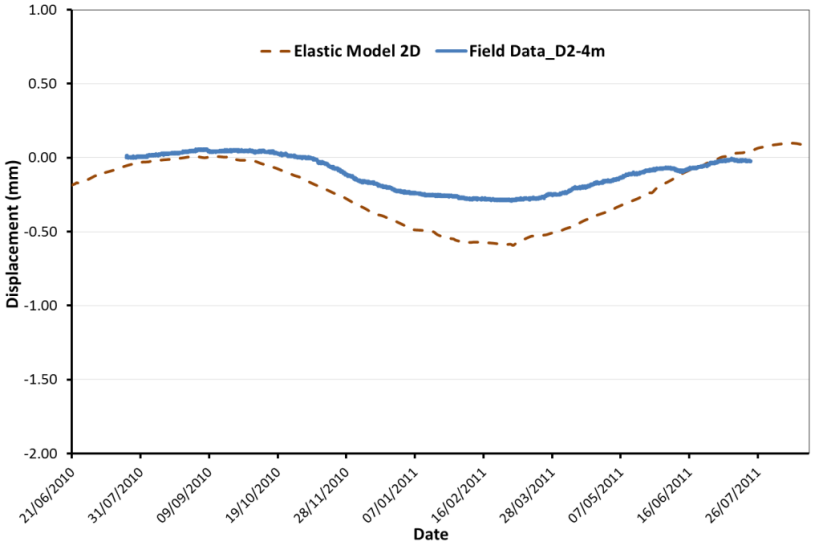

(b)

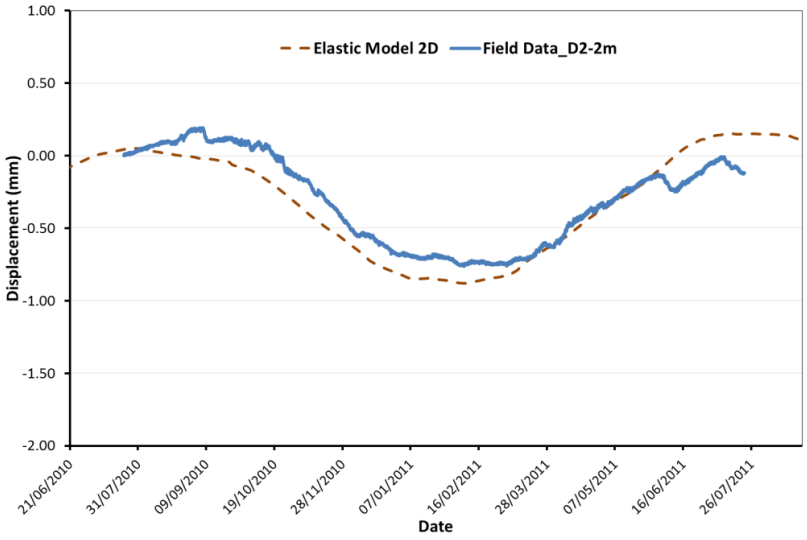

(c)

Figure 5-10. Displacements at distometer D2 - Elastic model 2D with net radiation flux; a) 6 meters into the rock; b) 4 meters into the rock; c) 2 meters into the rock.

With the low displacement values measured at decompressed zone, there is a possibility that the results can be represents by a continuum model. The difference between the vertical displacement at the points I5 and I6 was obtained of this elastic model (Figure 5-11); the numerical result shows that the decompressed zone behaves as the continuum, due to the vertical stress generates by the part of the weight (the arch effect can be generated) provides a restriction against the displacement. The previous behaviour described does not occur at the roof of the cavern when the confining is very low.

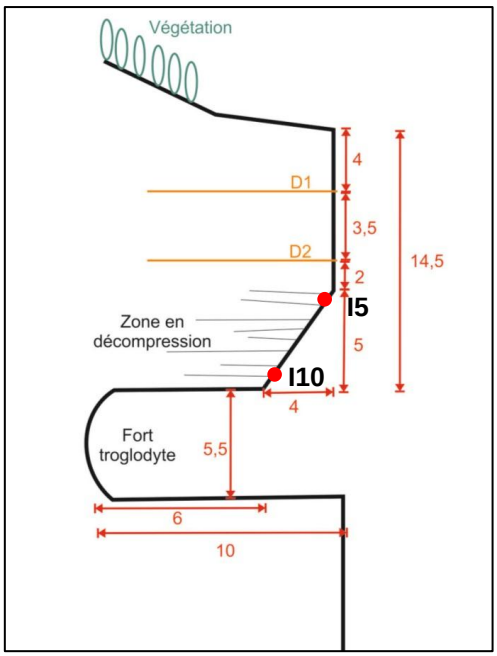

Figure 5-11. Measuring points at decompressed zone

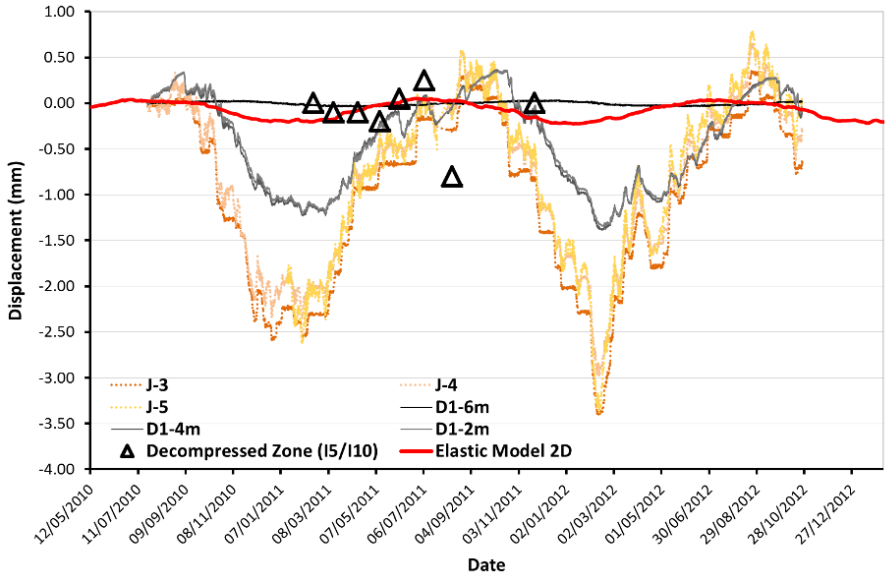

Figure 5-12. Displacements at decompressed zone - Elastic model 2D with net radiation flux

Negative values of the compressed zone indicate that this zone expands under low temperatures (see Figure 3-23).

5.1.2 Elastic model 2D without net radiation flux

This model was done with the only goal to demonstrate that the net radiation flux is a key action in this coupled problem. The model is the same as explained above, but as a boundary condition at the rock surface and cavern only the external temperature is imposed (Figure 5-13).

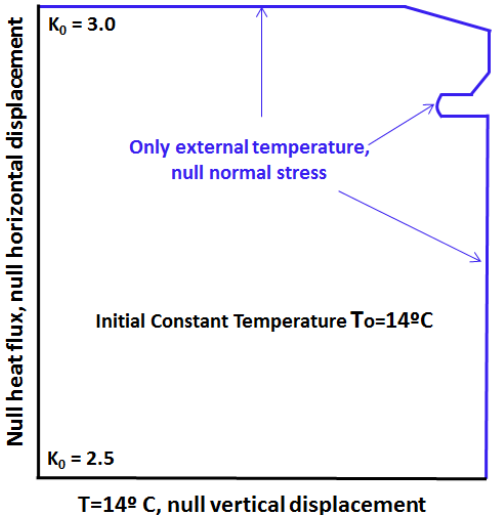

Figure 5-13. Elastic two dimensional model without radiation flux - Boundary and initial conditions

Even if, the series shows a stationary behaviour after an equilibrium phase, the Figure 5-14 and Figure 5-15 prove conclusively that the phenomenon must be include the net radiation flux as a boundary condition in a surface cliff. If the correct temperature isn't represented, the displacement is too wrong.

Finally, the graphical results of temperatures are shown in the Figure 5-16 and these are completely different to the graphical results of the model with net radiation flux.

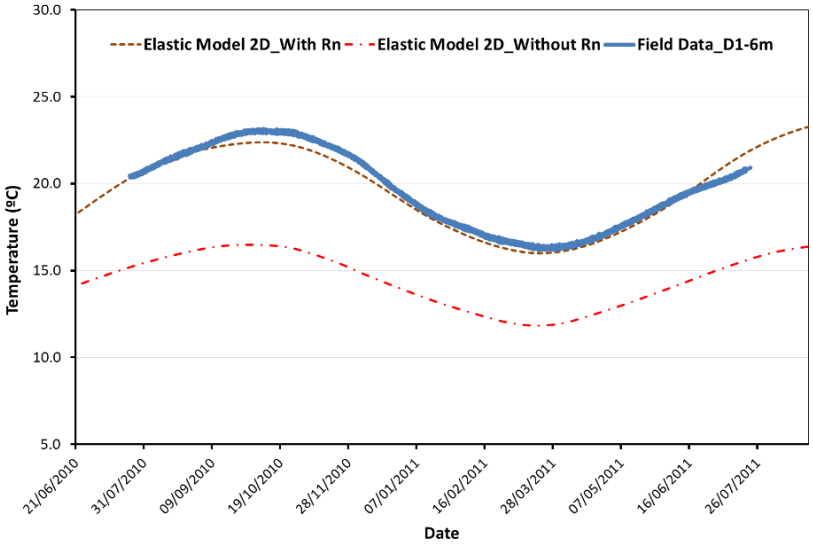

(a)

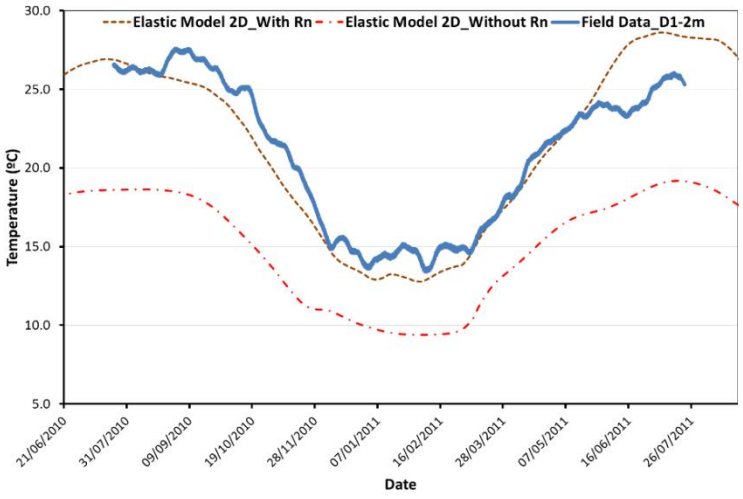

(b)

Figure 5-14. Temperatures at distometer D1- Elastic model 2D with net radiation flux vs Elastic model 2D without net radiation flux ; a) 6 meters into the rock; b) 2 meters into the rock.

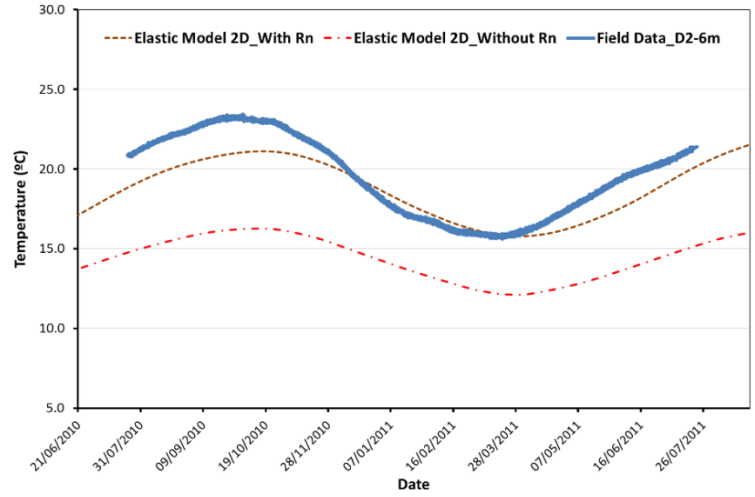

(a)

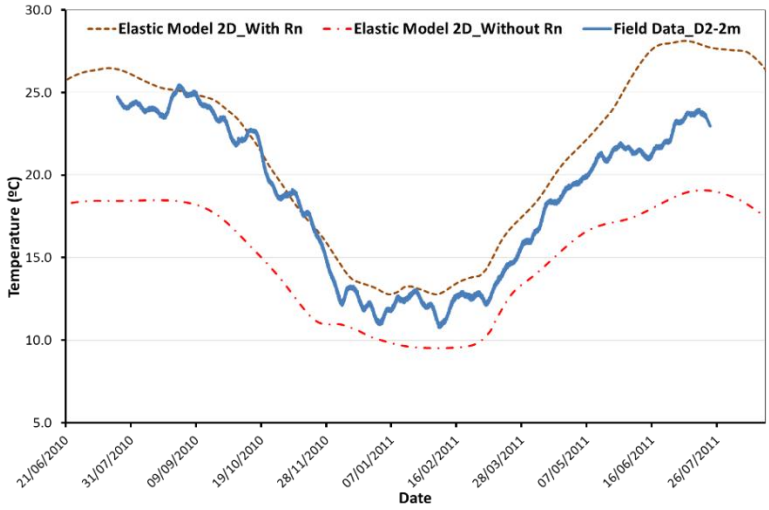

(b)

Figure 5-15. Temperatures at distometer D2- Elastic model 2D with net radiation flux vs Elastic model 2D without net radiation flux ; a) 6 meters into the rock; b) 2 meters into the rock.

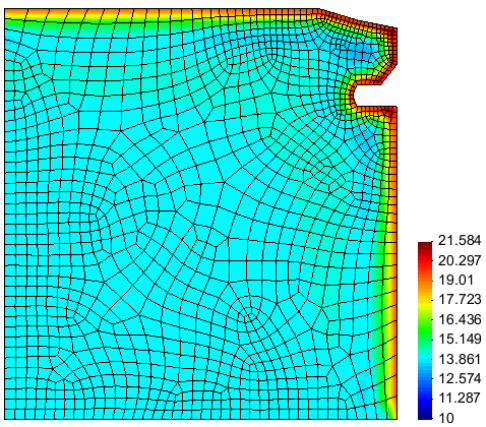

Date: 22/07/2010

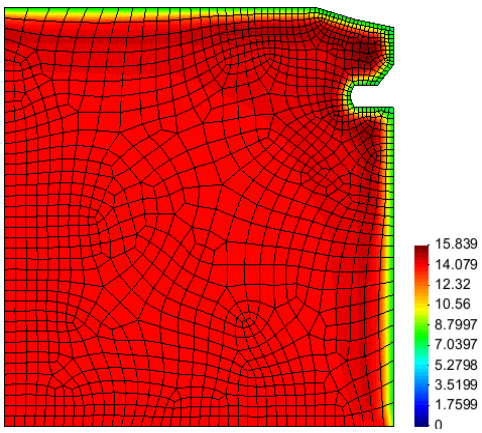

Date: 21/11/2010

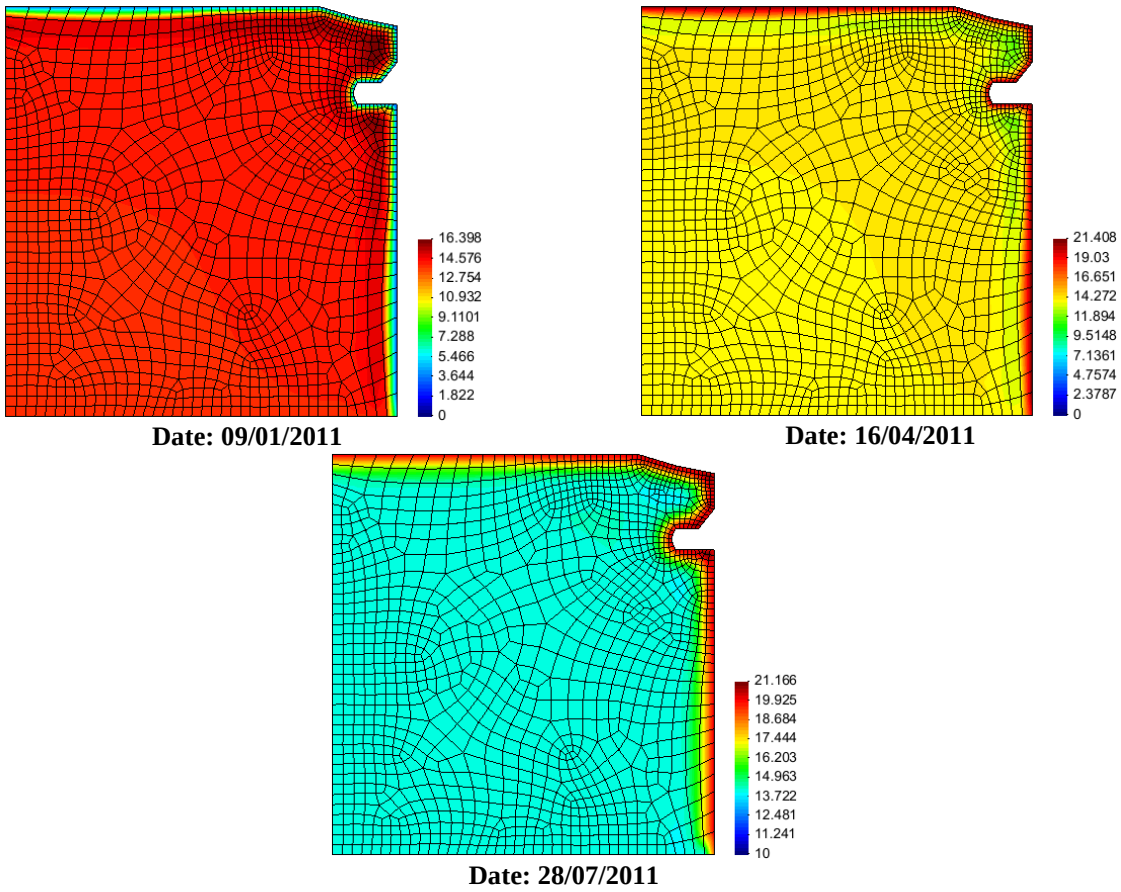

Figure 5-16. Graphical result of temperature - Elastic model 2D without net radiation flux

5.1.3 Elastoplastic model 2D (Hoek-Brown) with net radiation flux

The main disadvantage of the elastic laws is that the stress state isn't limited and irreversible responses can't be modelled. Although the most response of the cliff has a reversible character (except the residual beam within the cavern) is interesting to model the case under the elastoplastic model based in a Hoek & Brown failure criterion explained in the Chapter 4. The experimental information showed that the failure of the rock fits well with the criterion formulated by Hoek & Brown 1980.

The model created is a little bit different to above model with the aim to avoid the local effect in the upper corner. The mesh is composed of 1359 quadrilateral elements and 1433 nodes (very similar to elastic model) and the initial conditions are the same of elastic model mentioned above, considering the net radiation flux in the surface cliff and the external temperature in the cavern. The set of parameters is in the Table 5-2 when the thermal parameters are conserved.

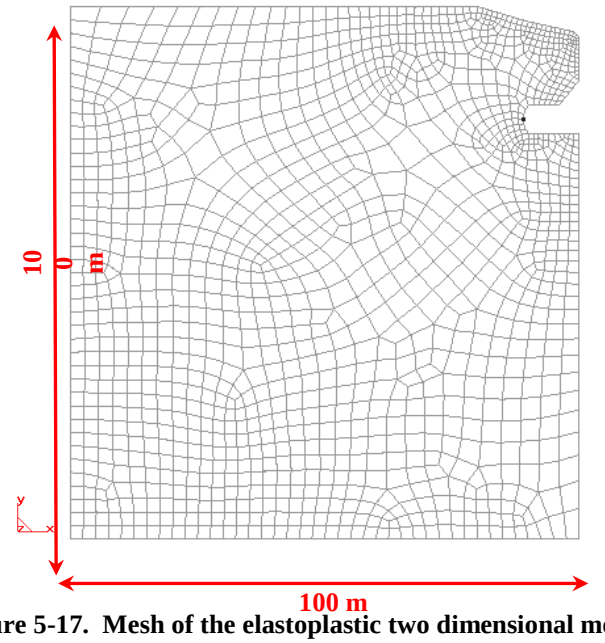

Figure 5-17. Mesh of the elastoplastic two dimensional model

Table 5-2 . Parameters of the elastoplastic model

Parameter	**Values**
Young's modulus	31000 MPa
Poisson's ratio	0.2
Uniaxial compressive strength	46.4 MPa
Tensile strength	5.4 MPa
Coeff. Setting the decrease of uniaxial compressive strength with temperature.	0.075
Brittleness parameter	1
Heat capacity	1200 $J.kg^{-1}.K^{-1}$
Thermal conductivity	2.0 $W.m.K^{-1}$
Thermal linear expansion coefficient	6 10^{-6} $^{o}C^{-1}$

With the results of two dimensional elastic model (with radiation) as a reference computation, the temperatures (see Figure 5-18 and Figure 5-19) and displacements (see Figure 5-20 and Figure 5-21) of this model are presented. As a general observation is that the response of the elastoplastic model is almost equal to the elastic model, with a small difference due to the quite difference between the mesh. The previous postulate means that the actions of thermal strain into the rock are reversible, but it is interesting to review the possible plastic strains at most level superficial and the time evolution of deviatoric stress (Invariant J of deviatoric stress tensor) across the rock.

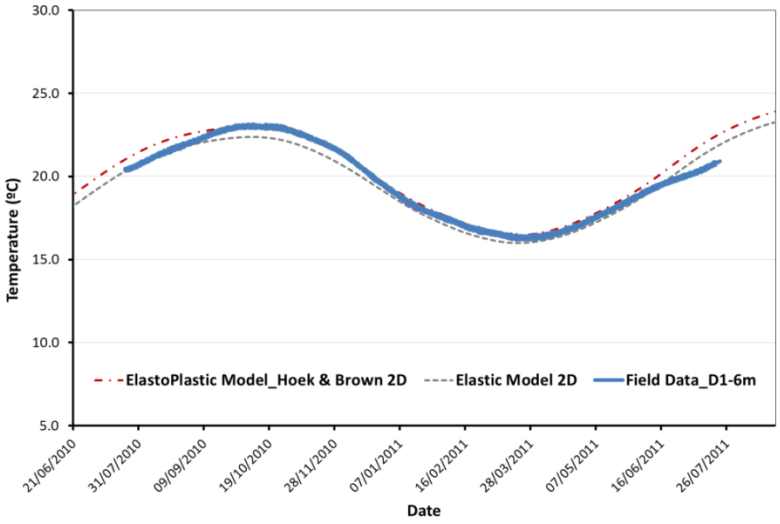

(a)

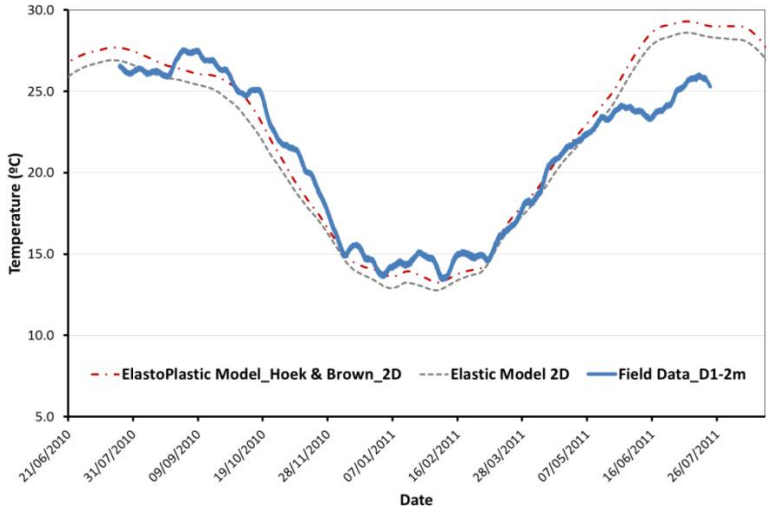

(b)

Figure 5-18. Temperatures at distometer D1 - Elastoplastic model 2D with net radiation flux; a) 6 meters into the rock; b) 2 meters into the rock.

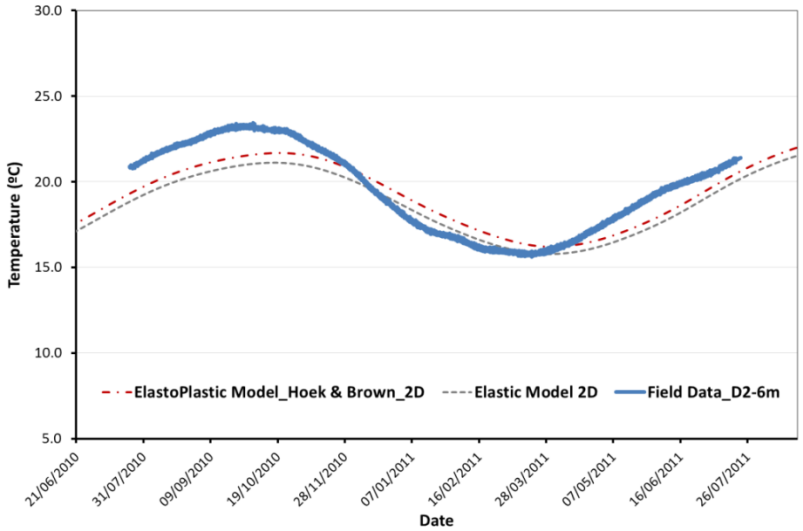

(a)

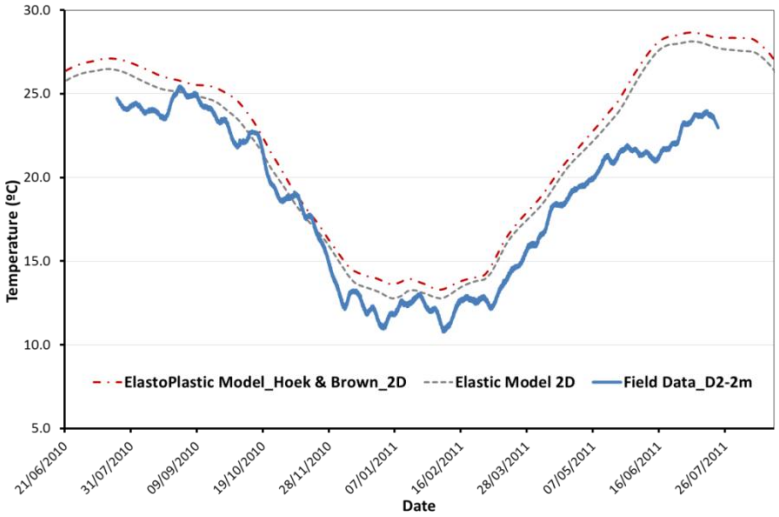

(b)

Figure 5-19. Temperatures at distometer D2 - Elastoplastic model 2D with net radiation flux; a) 6 meters into the rock; b) 2 meters into the rock

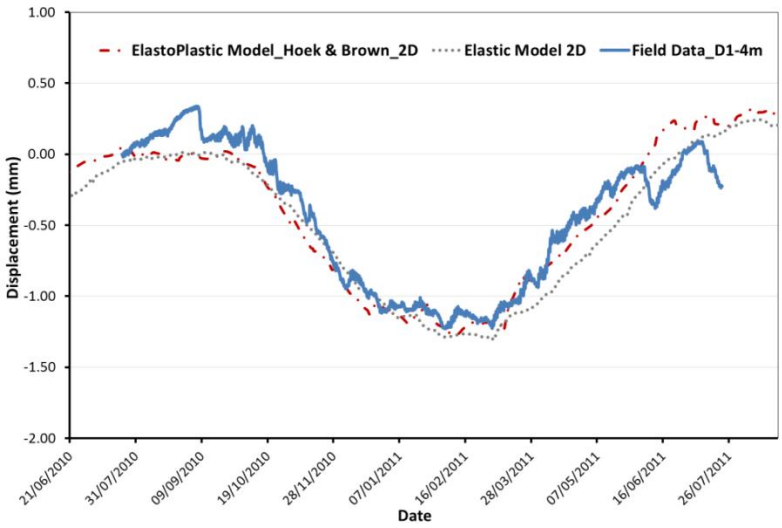

(a)

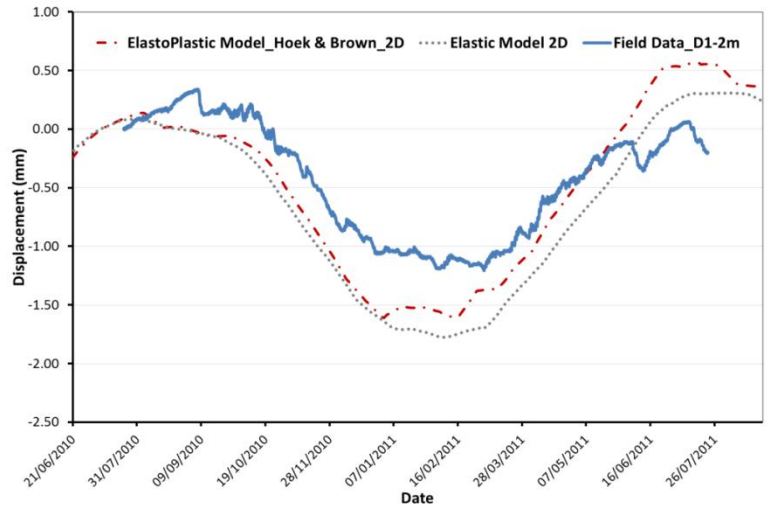

(b)

Figure 5-20. Displacements at distometer D1 - Elastoplastic model 2D with net radiation flux; a) 4 meters into the rock; b) 2 meters into the rock

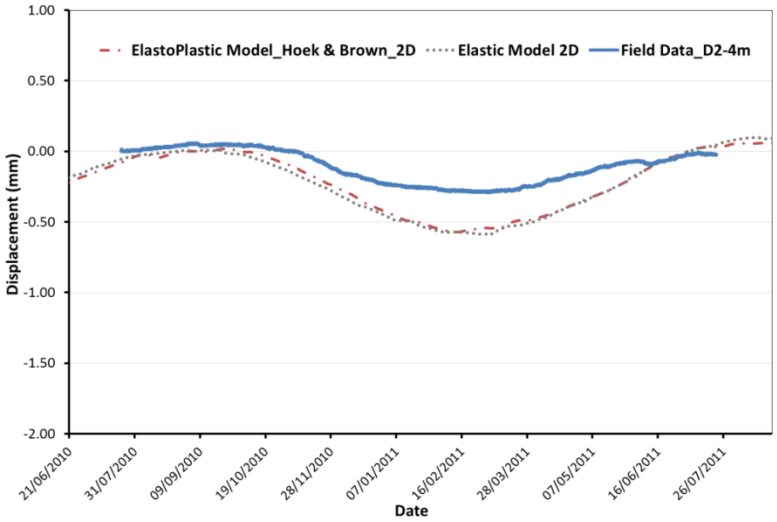

(a)

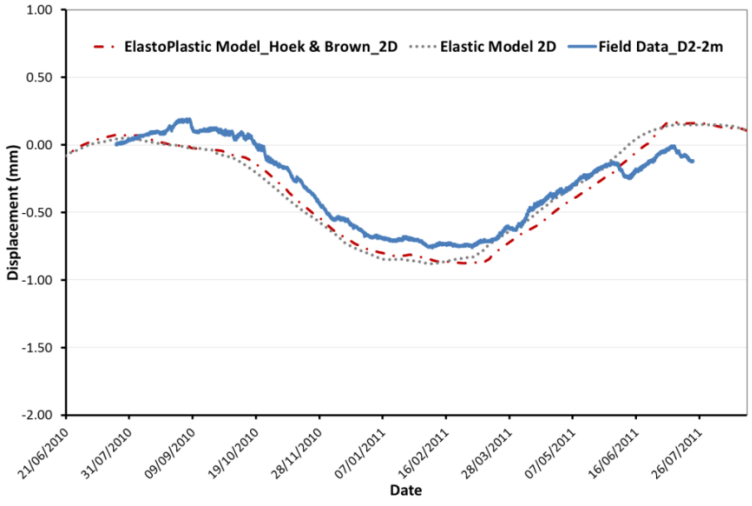

(b)

Figure 5-21. Displacements at distometer D2 - Elastoplastic model 2D with net radiation flux; a) 4 meters into the rock; b) 2 meters into the rock

A review on the plastic strain which is related with the plastic multiplier in the elastoplastic framework, suggests a generation of these on the surface rock-cliff; therefore the atmospheric actions (temperature) can be produce irreversible response on the rock.

The plastic strains located at the rock surface may be related with the flaking phenomenon, although other factors like weathering process by drying/wetting cycles at low confining stress can have influence, taking into account that the surface of the rock is the only site where the hydration due to rains occurs (the infiltration may be very small due to the vertical face of the cliff).

A section of plastic multiplier values along the distometer D1 site shows that the plastic strains are generated until 1.8 meter into the rock, which it is a deep phenomenon and the flaking is more superficial; however it is a dependence of the mesh and the element size (see Figure 5-22and Figure 5-23). Two simple models of 10 x 10 meters were performed and they are

subjected to the net radiation flux with the element size as an only difference between them. From the Figure 5-23, a concluding remark is that the deep of the plastic strains depends of the element size. This dependence is only a geometrical relationship between the element size and the results, because another complex dependence exists, where the element size influences the overall numerical response (i.e. modelling of softening).

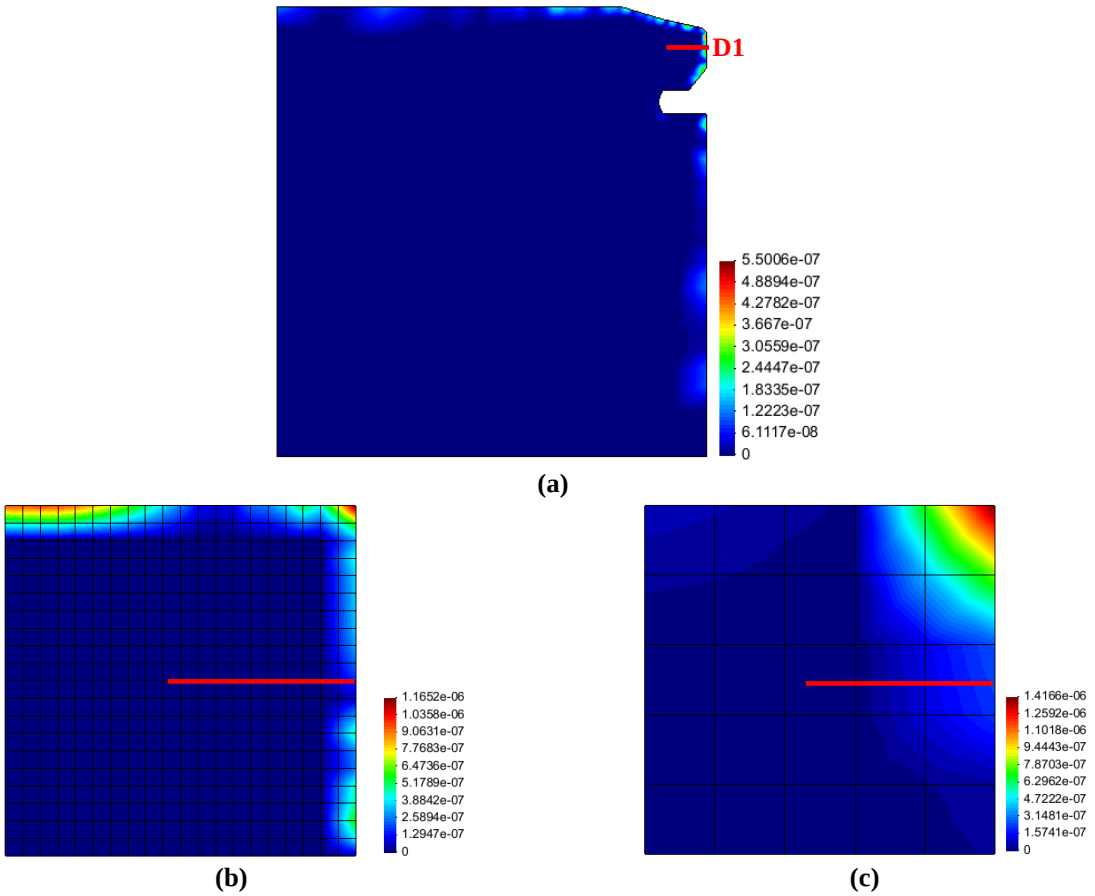

Figure 5-22. Plastic Multiplier - Elastoplastic model 2D with net radiation flux; a) case *La Roque Gageac*; b) Finite Element model with high discretization; c) Finite Element model with low discretization

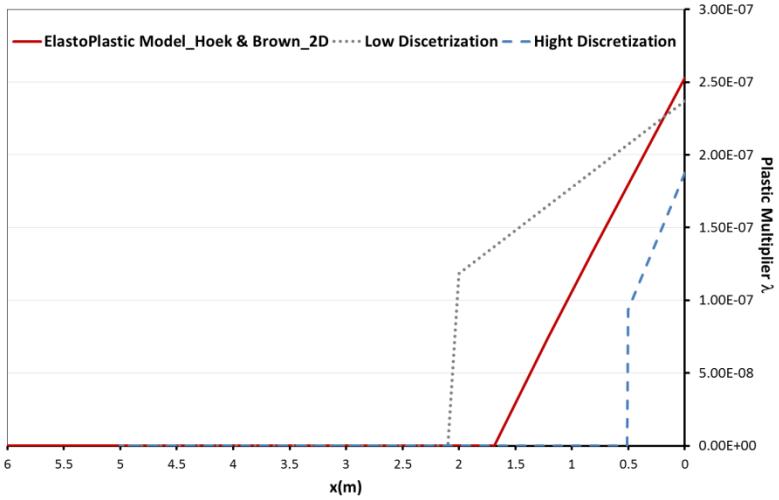

Figure 5-23. Plastic Multiplier along the sections

The Hoek & Brown failure criterion have a deviatoric stress as a measurement to determine the irreversible response and with the above results is necessary to evaluate the time evolution of that measurement (Invariant J) and its relation with the thermal effects. The Figure 5-24 shows the graphical results of the invariant J at different times of year analysed. The variations of deviatoric stress with the thermal cycles are higher at the surface of the cliff and decreases inside the rock (see Figure 5-25). The invariant J (deviatoric stress) presents a higher values when the temperature into the rock is low and due to the relation between the variation of the invariant J and temperature, the delay of values at different deep exist too.

It is possible to conclude that the response of the cliff is elastic, except the superficial flaking phenomena and the residual beam within the cavern.

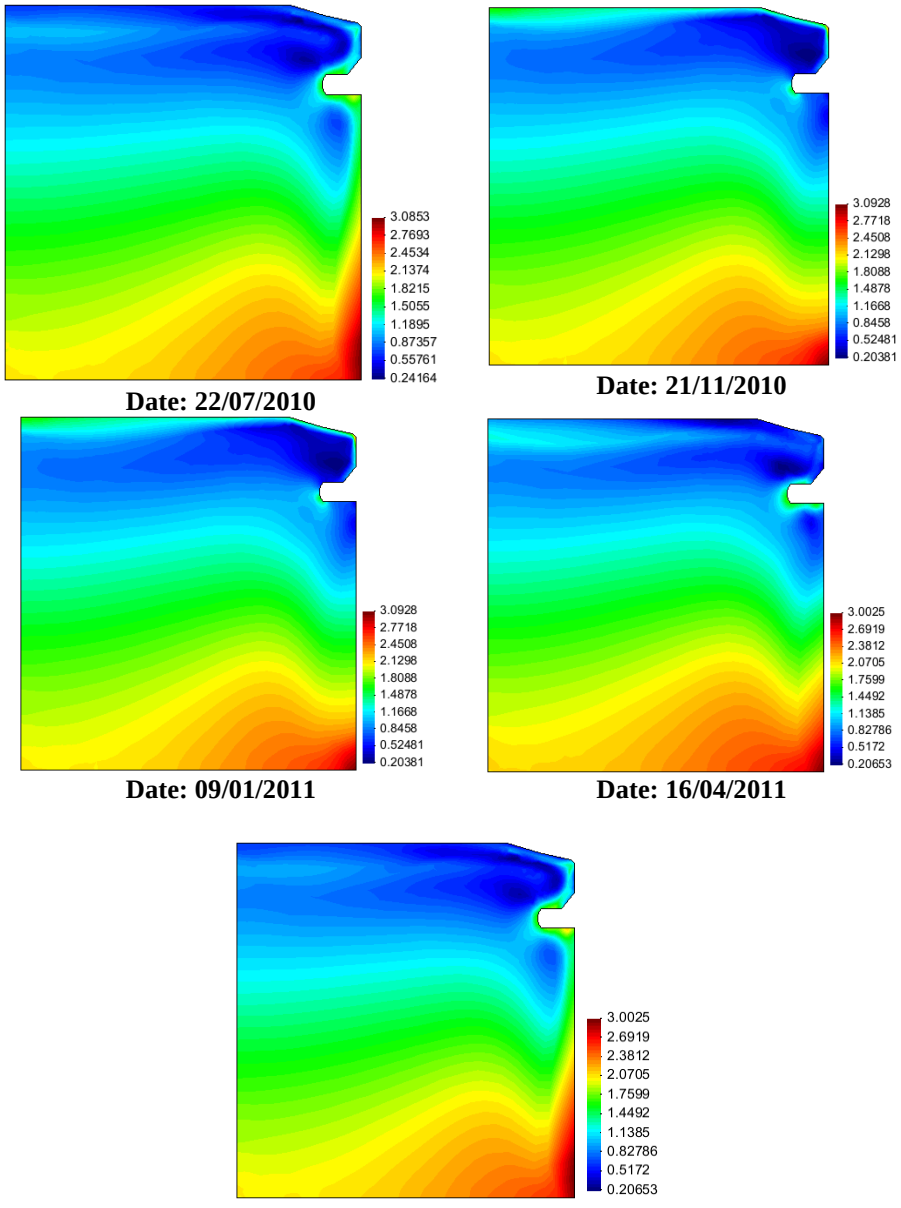

Figure 5-24. Graphical result of Invariant J - Elastoplastic model 2D

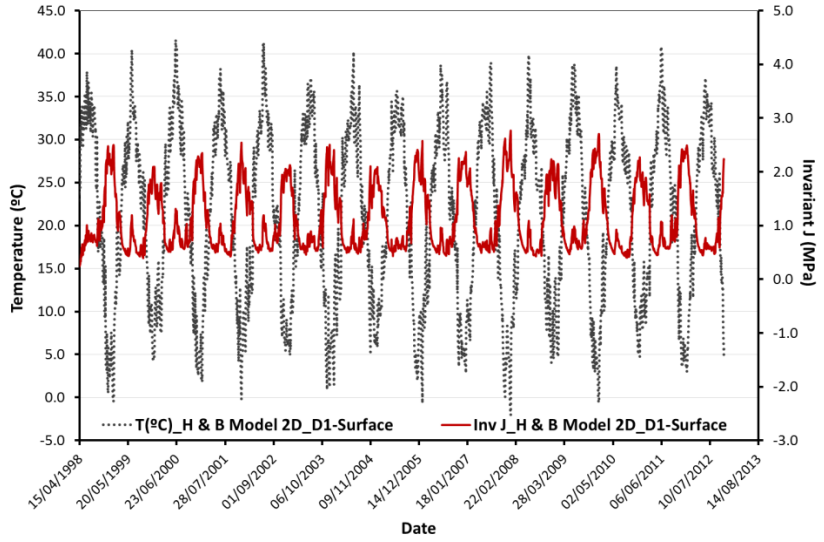

(a)

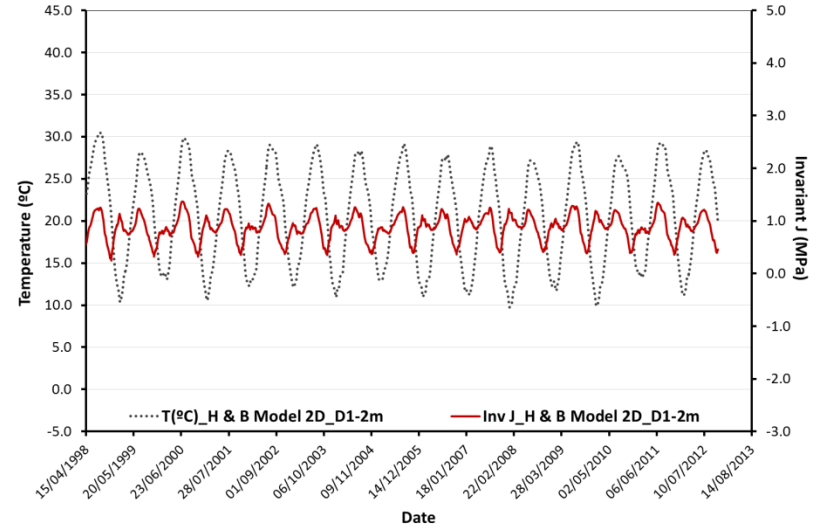

(b)

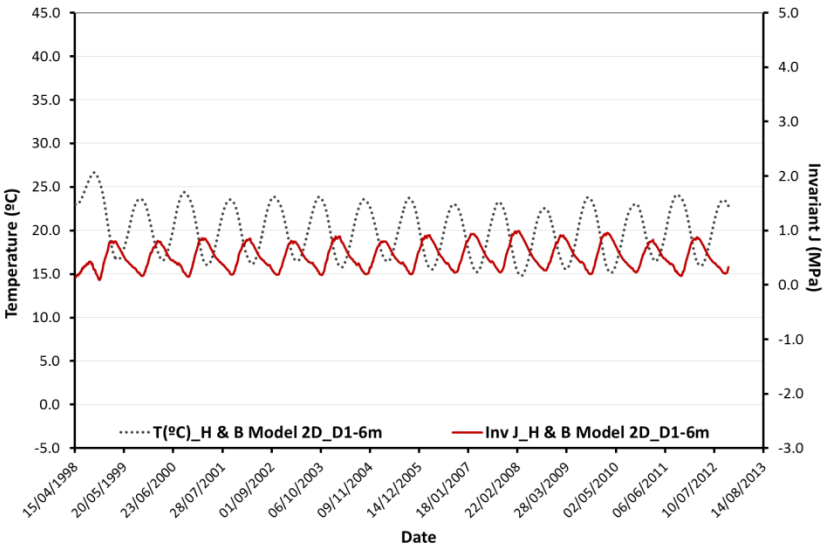

(c)

Figure 5-25. Invariant J calculated in stationary thermal cycles; a) Distometer D1 at surface; b) Distometer D1 at 2m; c) Distometer D2 at 6m; d) Distometer D2 at 6m.

5.1.4 Elastic model 3D with net radiation flux

The interest of creating a three dimensional model is based on the idea to analyse the response of the cavern at different condition to the plain strain, because the arch effect is impossible to evaluate through two dimensional models.

The generation of the arch effect can prove the hypothesis that the roof of the cavern is loaded only by own weight, as mentioned Sofianos, 1996. Likewise, checking that plain strain is a good approximation to the problem can be done.

The shape of the troglodyte cavern can be simplified due to a support located at the middle of the. The real excavation has a length of 36 meter, but at 18 meters a support of rock exist (Figure 5-26) generating a small cavern that contains the residual rock beam within the cavern. Another special characteristic is that the small cavern is divided by the vertical diaclasis at its middle.

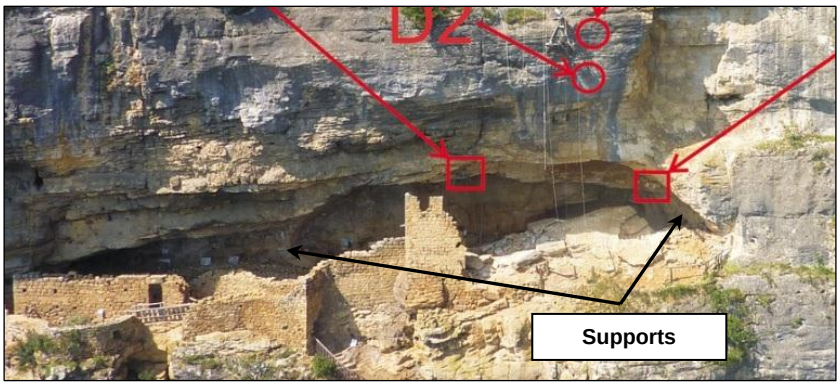

(a)

(b)

Figure 5-26. Real shape of the troglodyte cavern.

The three dimensional model reproduces a small cavern that have a residual rock beam, thus the distance between the supports is 18 meters. The fact that the cavern modeled is symmetric is an important advantage to interpretation work.

The mesh of finite element model is presented in the Figure 5-27 and it is composed by 18771 tetrahedral elements and 3801 nodes, which implies large calculation times. The parameters (thermic and mechanical) are in the Table 5-1 and the boundary and initial conditions are the same that elastic 2D model with the radiation flux.

Again, with the elastic 2d model as a reference computation, the results of this three dimensional (3D) model are shown from the Figure 5-28 to Figure 5-32. A good approximation to the real data is presented by the numerical result of this 3D elastic model and the small differences come from the mesh, which have elements of large size.

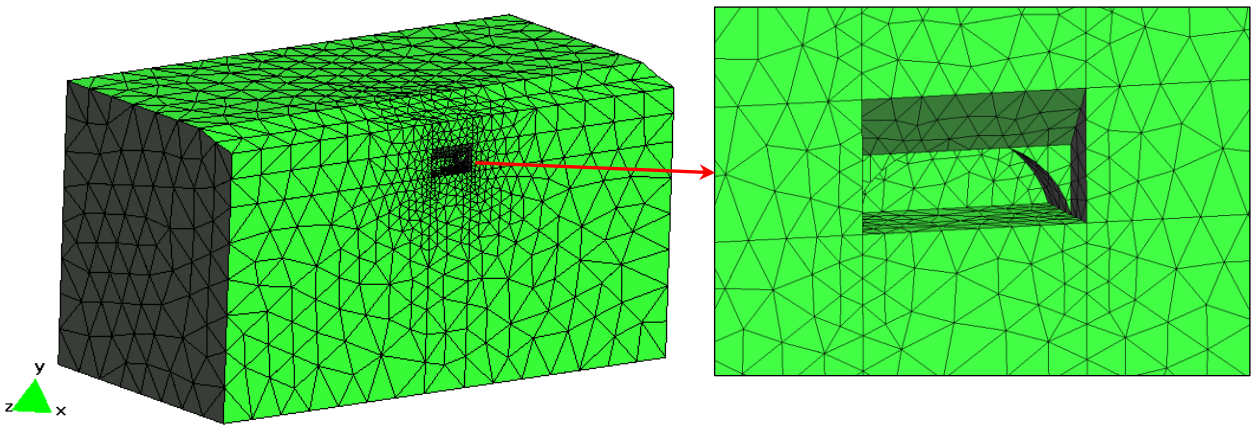

Figure 5-27. Mesh of elastic model 3D.

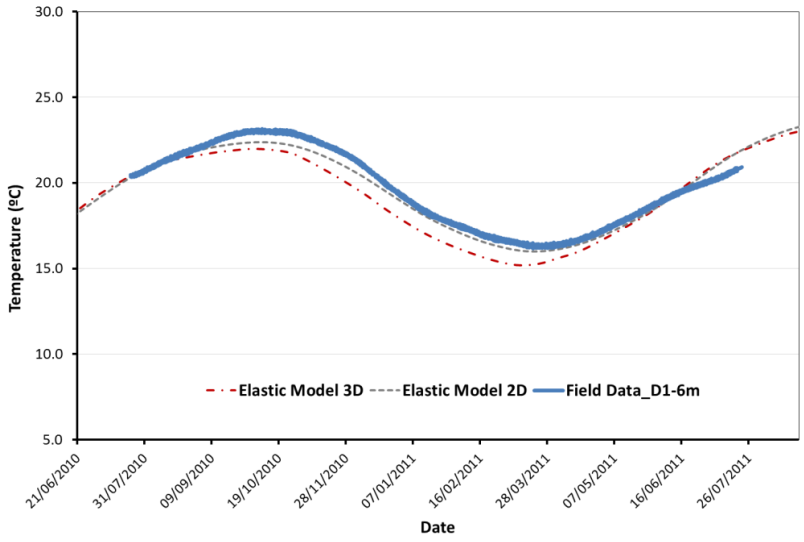

(a)

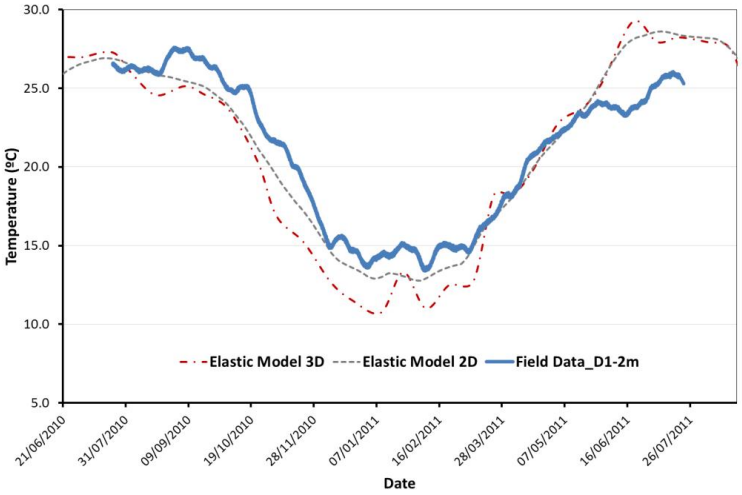

(b)

Figure 5-28. Temperatures at distometer D1- Elastic model 3D vs Elastic model 2D; a) 6 meters into the rock; b) 2 meters into the rock.

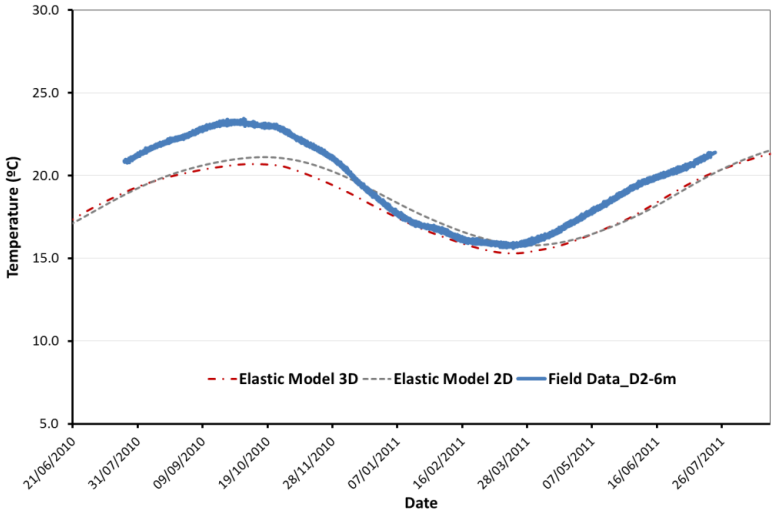

(a)

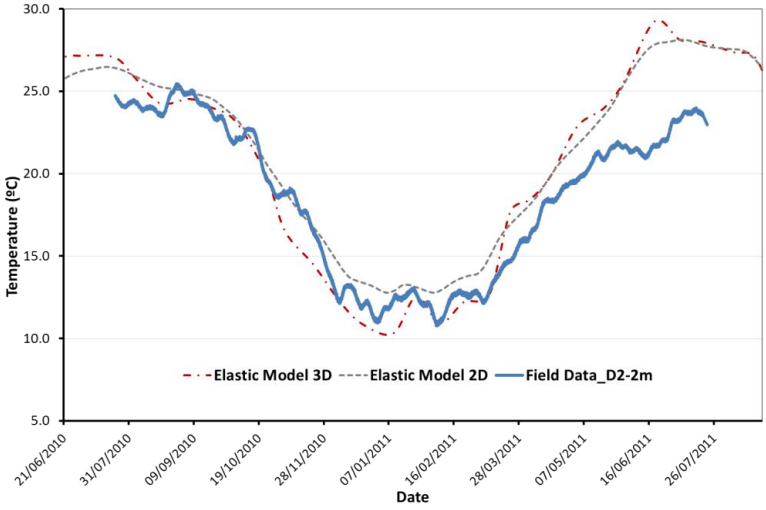

(b)

Figure 5-29. Temperatures at distometer D2- Elastic model 3D vs Elastic model 2D; a) 6 meters into the rock; b) 2 meters into the rock.

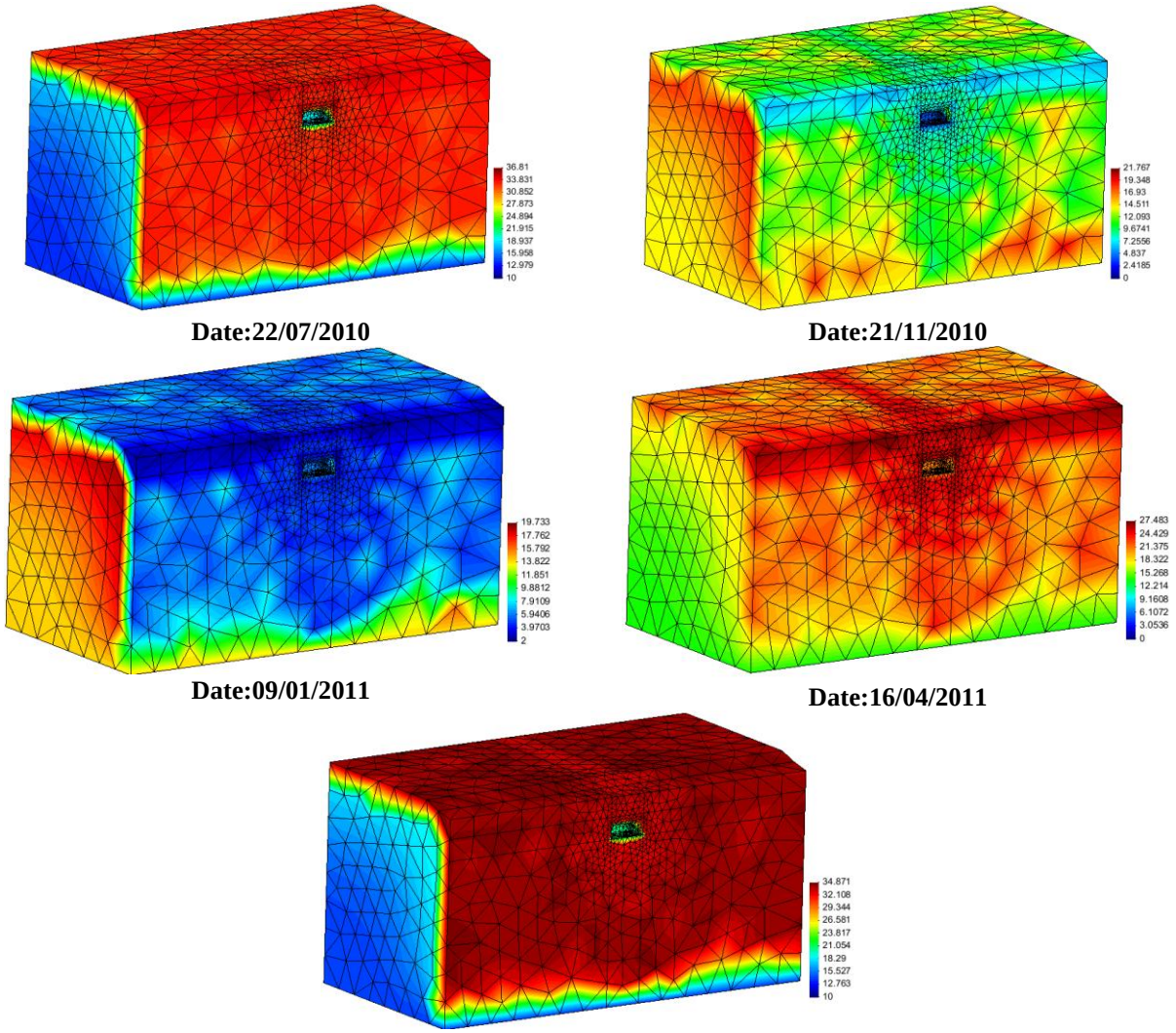

Figure 5-30. Graphical result of temperature - Elastic model 3D with net radiation flux

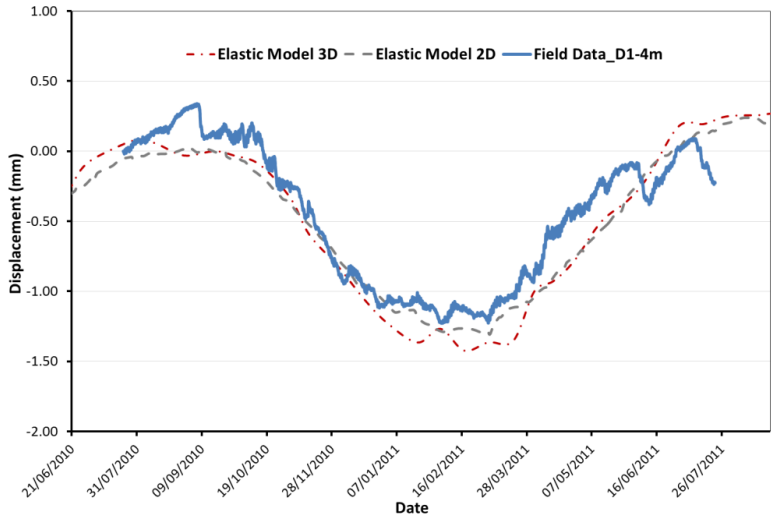

(a)

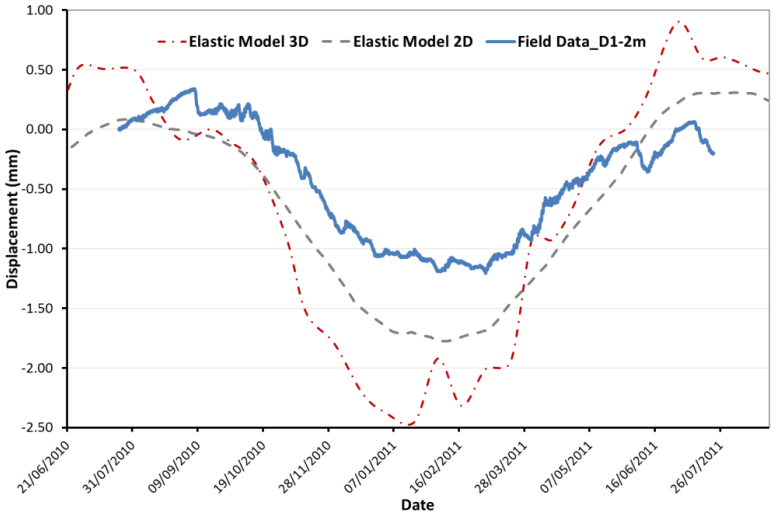

(b)

Figure 5-31. Displacements at distometer D1- Elastic model 3D vs Elastic model 2D; a) 6 meters into the rock; b) 2 meters into the rock.

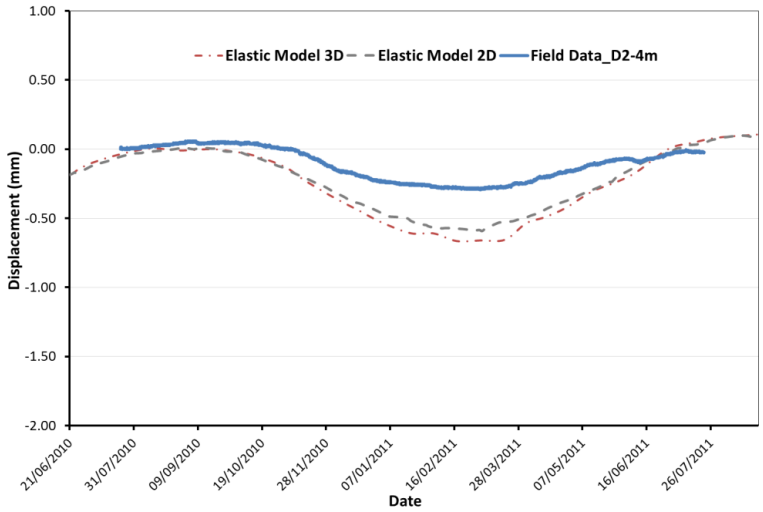

(a)

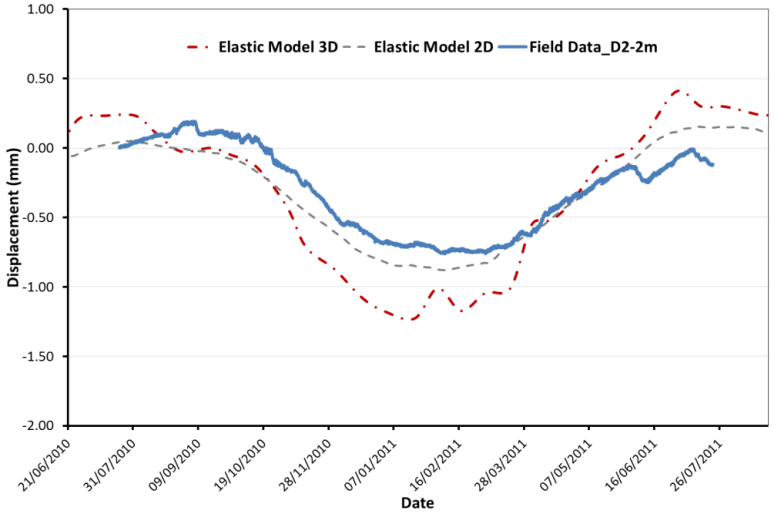

(b)

Figure 5-32. Displacements at distometer D1- Elastic model 3D vs Elastic model 2D; a) 6 meters into the rock; b) 2 meters into the rock.

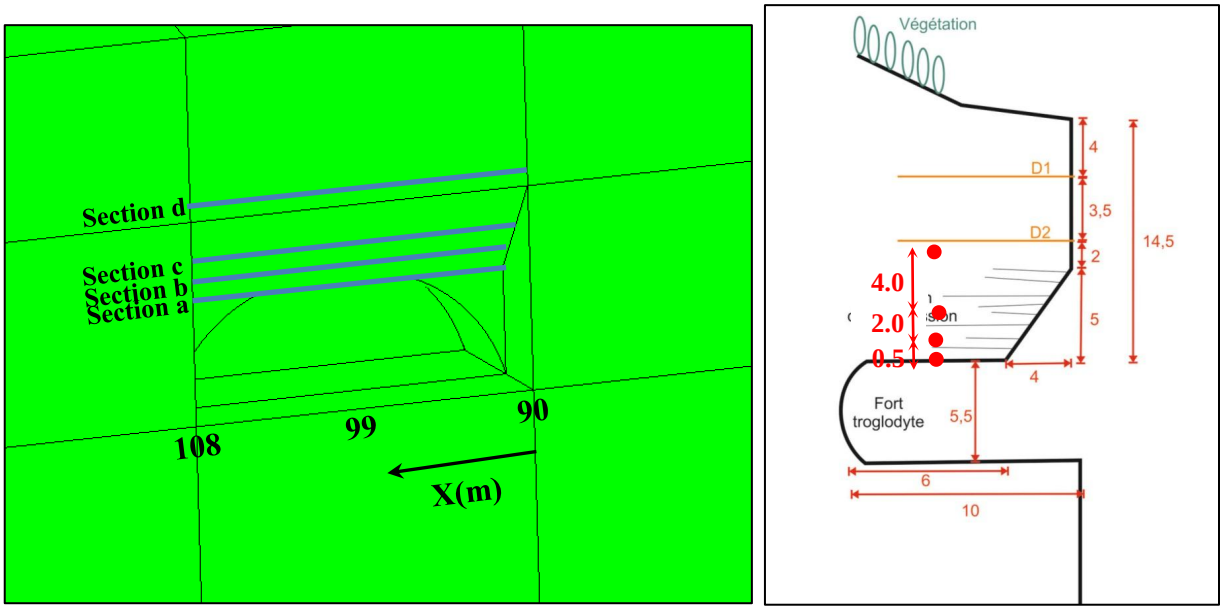

Figure 5-33. Location of the sections a, b, c and d

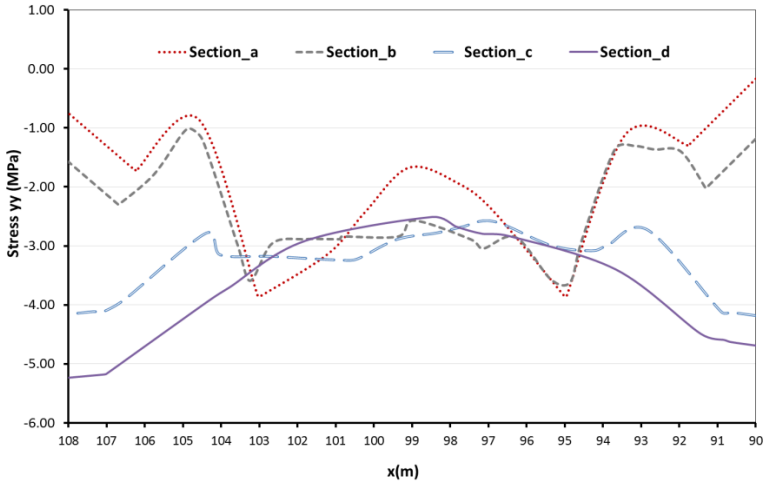

Figure 5-34. Vertical stress (Syy) at sections a, b, c and d.

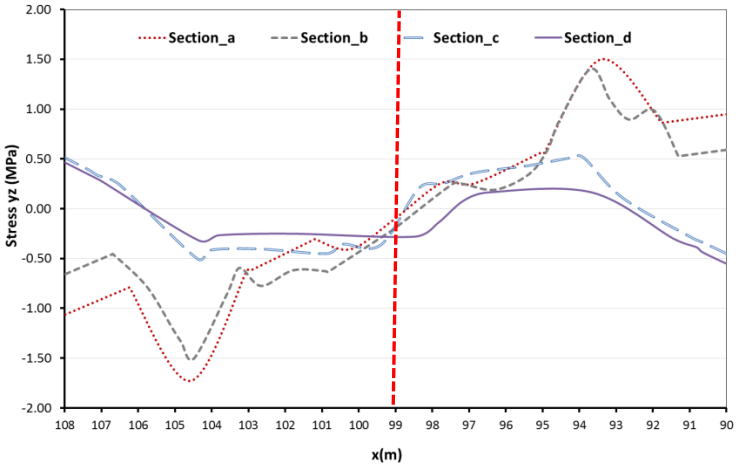

Figure 5-35. Shear stress (Syz) at sections a, b, c and d.

The stress state was evaluated through four horizontal sections above the cavern (Figure 5-33). An interesting behavior is shown by the vertical stress due to the sections a and b has a values less than the sections c and d (negative values means compression); checking the arch effect at the roof of the cavern. It is likely that horizontal discontinuities contributes that the roof is only loaded by own weight.

Respect to the shear stress a symmetric response is obtained with the symmetric axis corresponding to the middle of the cavern (Figure 5-35) and the shear stress tends to disappears away from the cavern.

5.1.5 Roof of the cavern model (Residual Beam)

The above modelling works have been successful reproducing the distometers responses and zones when the response is similar to continuum media (i.e. decompressed zone), however the discontinuities could not be modelled. As mentioned above the distometers gives the responses of a continuum rock when the low temperature generates contractions and the jointmeters provide the measurements of joint formed by rock blocks, therefore the low temperatures generates a contractions in these blocks and finally an aperture is registered by the equipment. To model this behaviour is necessary a special numerical element with zero thickness that allows reproduce the separation of the blocks rock.

As a first approximation to this problem the joint element has an elastic behaviour (Zandarin 2010). It is related with the normal effective stress (σ') and the tangential stresses (τ) to the normal (u_n) and the tangential (u_s) displacement of the joint element using normal (K_n) and tangential stiffness (K_s), respectively. Normal stiffness depends on the opening of the joint, as shown in Eq. 5-1 (see Figure 5-36).

$$\begin{Bmatrix} \sigma' \\ \tau \end{Bmatrix} = \begin{bmatrix} K_n & 0 \\ 0 & K_s \end{bmatrix} \begin{Bmatrix} U_n \\ U_s \end{Bmatrix} \qquad \textbf{Eq. 5-1}$$

$$K_n = \frac{m}{a - a_{\min}}$$

where m is a parameter of the model; a is the opening of the element, and a_{min} is the minimum opening of the element (at this opening the element is closed).

In future works an elastoplastic constitutive laws can be implemented with the goal to reproduce irreversible apertures under external actions (i.e. Gens et al 1990). In the elastoplastic constitutive laws the aperture of joint element changes under cycles of loading/unloading, but this can be related with the thermal cycles.

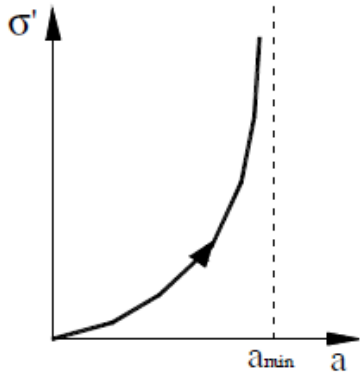

Figure 5-36. Elastic constitutive law of the joint element. Normal stiffness depends on joint opening. Zandarin 2010

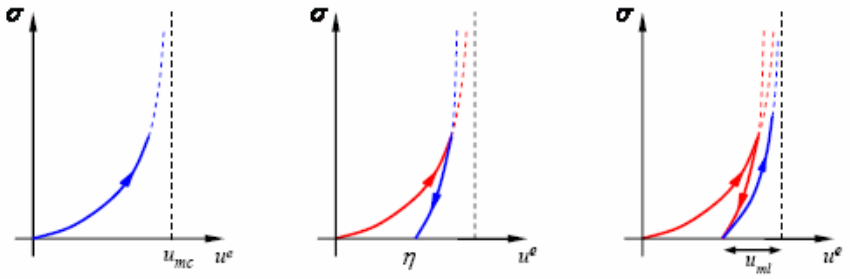

Figure 5-37. Elastic constitutive law. Normal stress vs. aperture for first loading, unloading and reloading respectively (Gens et al., 1990).

A first idea to implement the joint element can be a horizontal arrangement, trying to simulate the roof of the cavern as a beam generated by the decompressed zone (Figure 5-38). However this mechanism is extremely unstable and unrealistic. From the field observation (see Figure 5-39) the residual beam is limited by numerous discontinuities and its modelling is not possible through the section used until now.

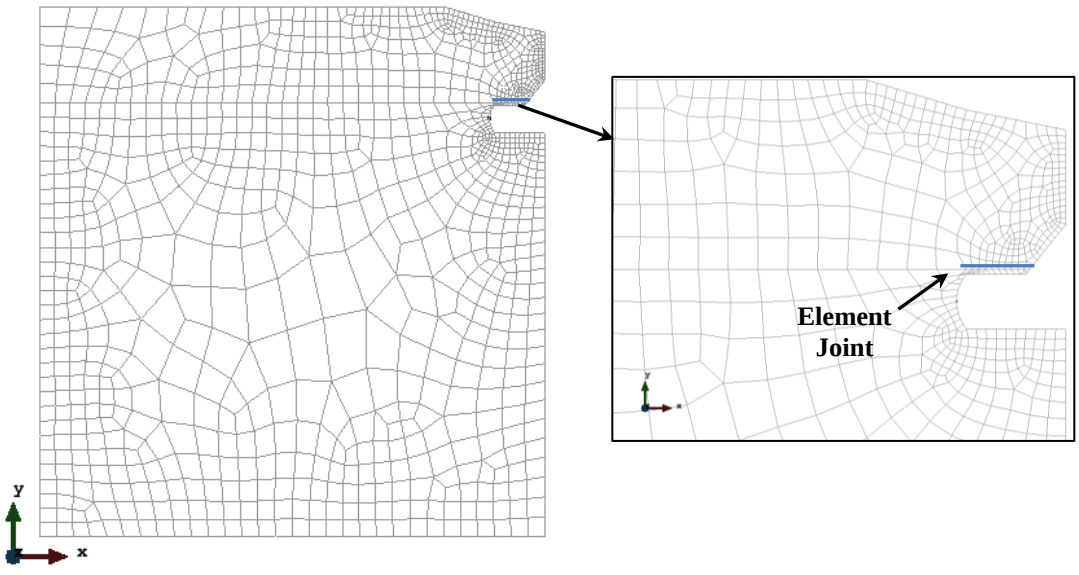

Figure 5-38. Horizontal joint at the roof of the cavern

Figure 5-39. Residual beam arrangement.

The new section should be representative of the main discontinuities arrangement. This section can be a front view of the roof and it can be include the discontinuities measured by the jointmeters J-1, J-2 and J-3 (Figure 5-40).

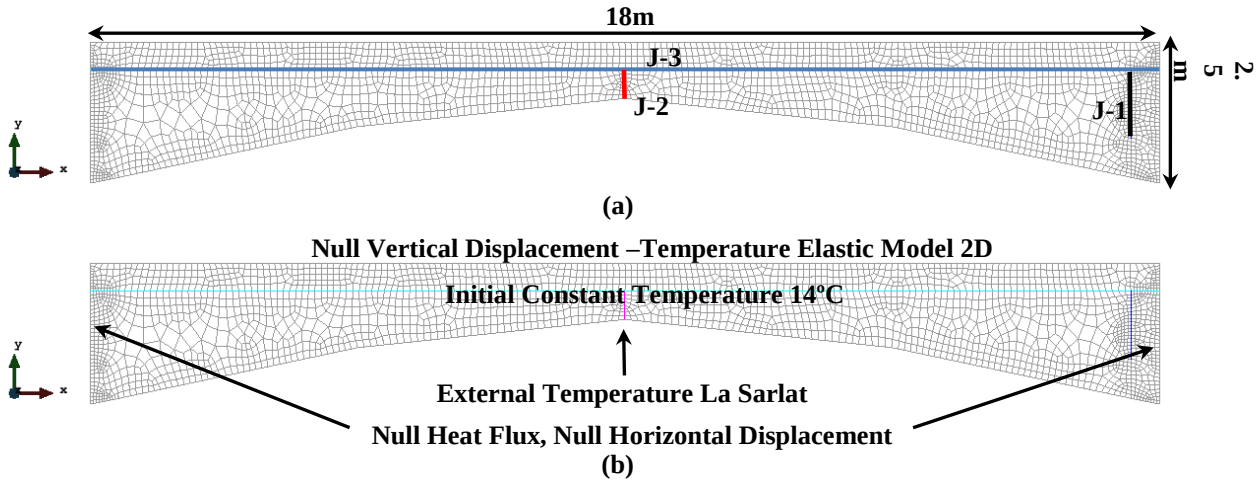

Figure 5-40. Finite element model of roof of the cavern; a) Geometry and joint elements modelled; b) Boundary and initial conditions

Besides the joint elements, the model has a special convention about the initial stress state. The vertical stress corresponds only to the own weight, but the horizontal stress comes of stress at height of the cavern. Due to the cavern is not exposed to the sun light, the temperature imposed at upper and lower limits are presented in the Figure 5-40 and Figure 5-41. The numerical model contained 5 years of computation.

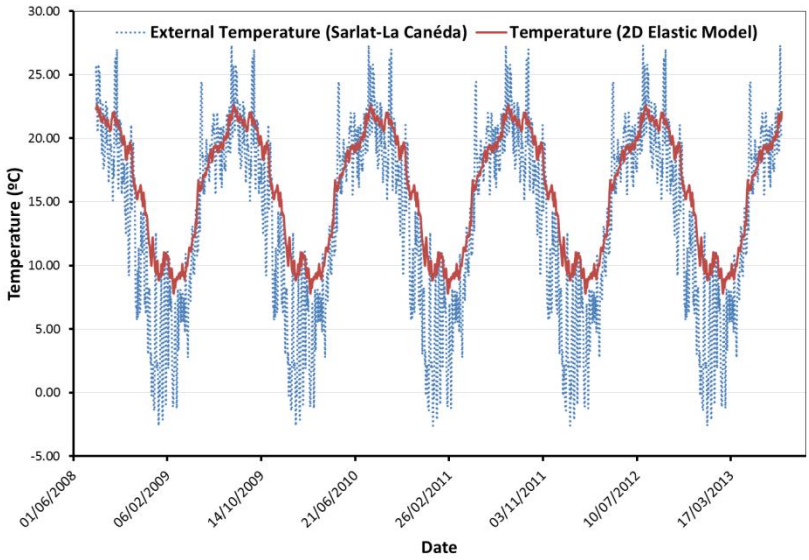

Figure 5-41. Temperature imposed at upper and lower limits of the model

The conduction phenomenon, through the Fourier's laws governs the thermal behaviour of the joint element. Is possible to apply different values of thermal conductivity and heat capacity, taking into account the influence of air, but for this case the thermal parameters are the same of rock (Table 5-3).

The initial normal stiffness parameters have been back-analyzed to adjust the deformations measured in the jointmeters.

The graphical results of temperature evolution are shown in the Figure 5-42 and from the thermal evolution the joint apertures is analysed.

Table 5-3 . Parameters of the elastic model of the roof

Parameters of the rock	**Values**
Young's modulus	31000 MPa
Poisson's ratio	0.2
Heat capacity	1200 $J.kg^{-1}.K^{-1}$
Thermal conductivity	2.0 $W.m.K^{-1}$
Thermal linear expansion coefficient	6 10^{-6} $ºC^{-1}$
Parameters of J-1 and J-2	**Values**
Initial normal stiffness parameters	80
Tangential stifness	3100 MPa
Minimun opening	0.0001m
Initial opening	0.01m
Parameters of J-3	**Values**
Initial normal stiffness parameters	80
Tangential stifness	3100 MPa
Minimun opening	0.0001m
Initial opening	0.01m

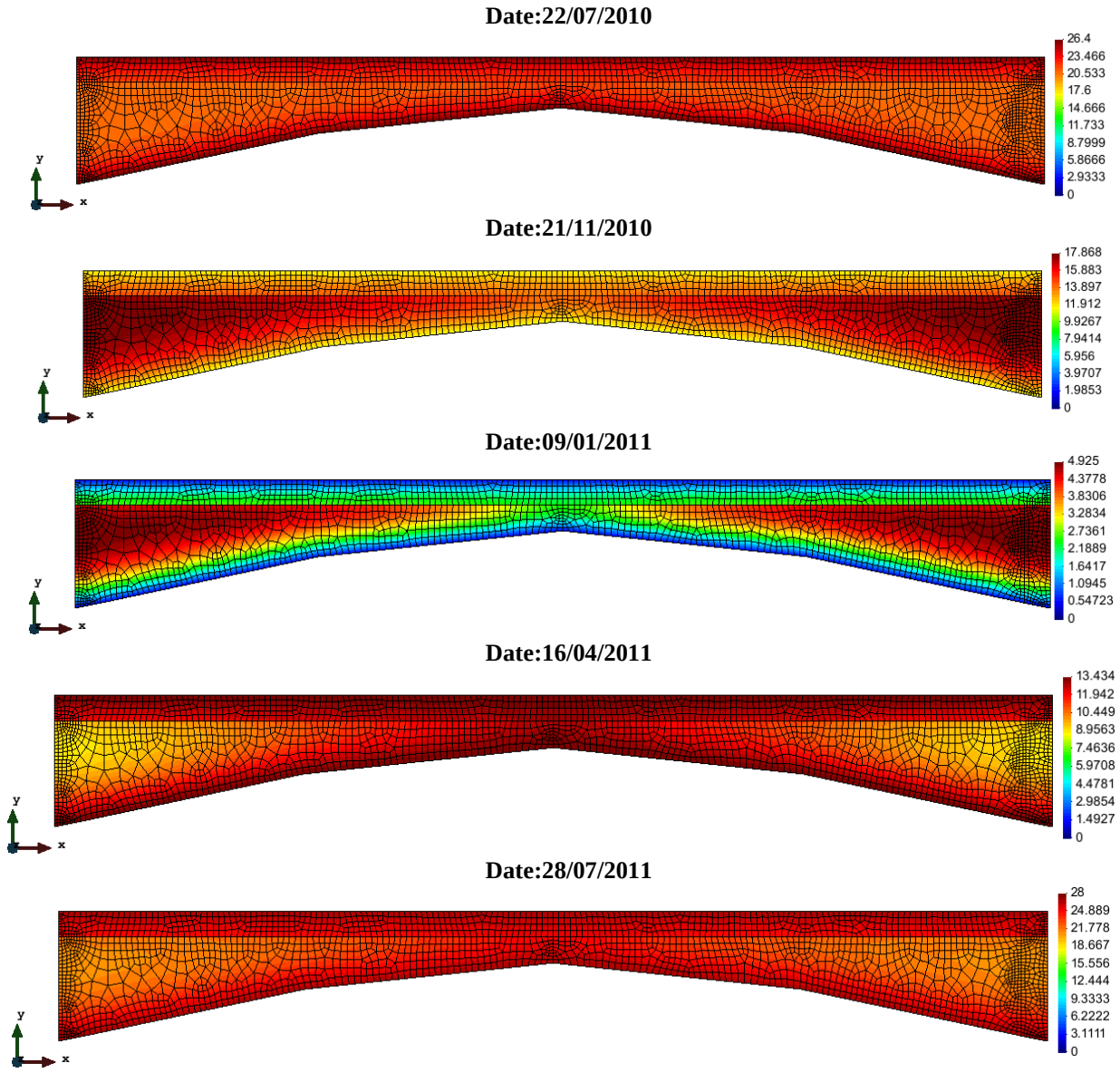

Figure 5-42. Graphical result of temperature - Elastic model of the roof

Figure 5-43 compares the aperture computed by the finite element model with the measurements. A good agreement is observed for jointmeters J-2 and J-3. The difference in jointmeter J-1 is due to the discontinuity modelled has a vertical orientation and this device was removed to the horizontal discontinuity at December 2010 (see Figure 3-14). The convention of negative values as opening increases is conserved.

The evolution of the normal stress on the discontinuities is clearly related to the thermal cycles. As seen in the Figure 5-44, discontinuities J-1 and J-2 suffer tractions when temperature reaches a low value. The aspect is central to the stability of the residual beam due to this traction affects the rock joints within the discontinuities, which guarantee the stability of the element fractured.

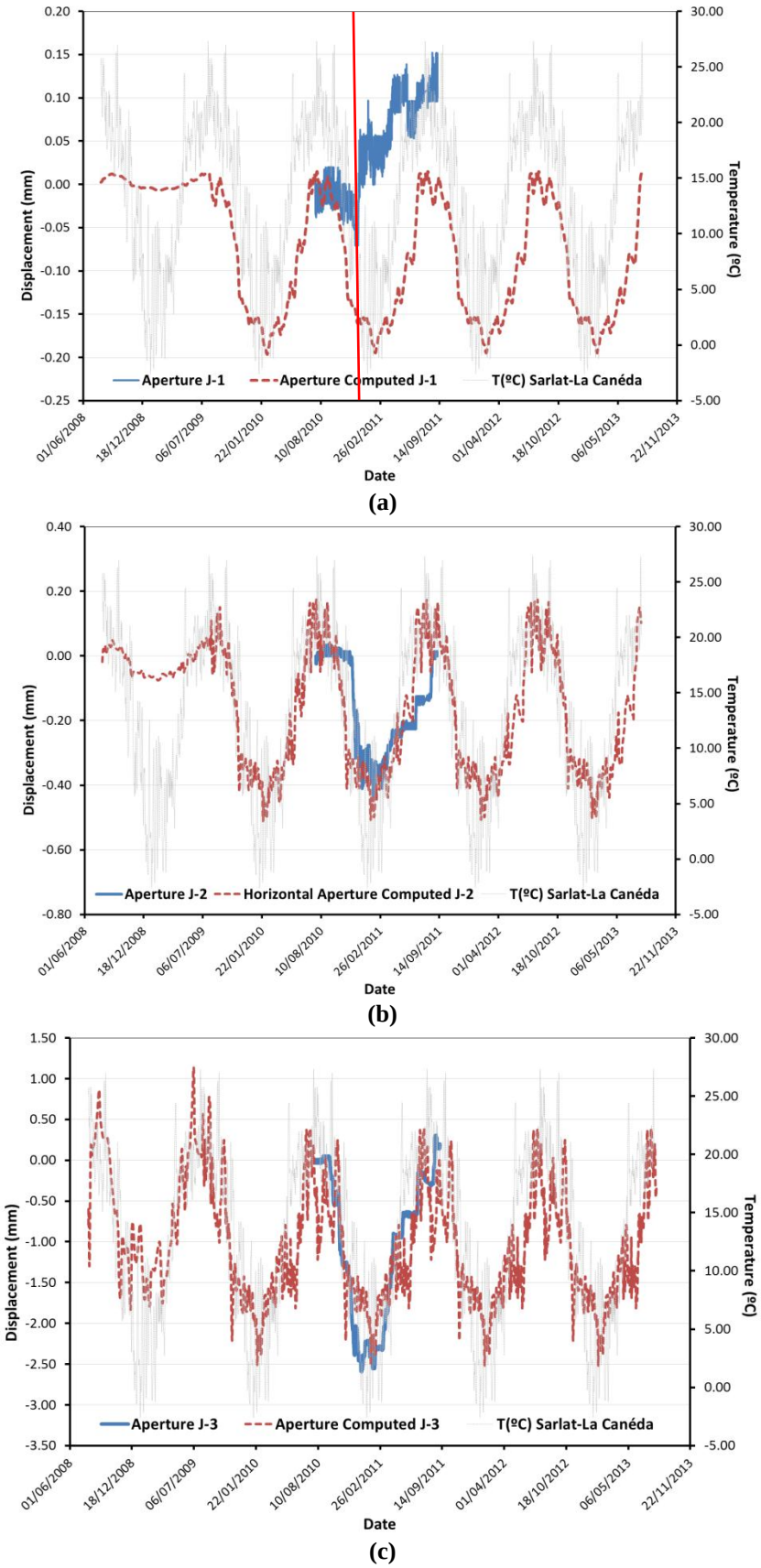

Figure 5-43. Apertures computed in joints; a) Jointmeter J-1; b) Jointmeter J-2; c) Jointmeter J-3

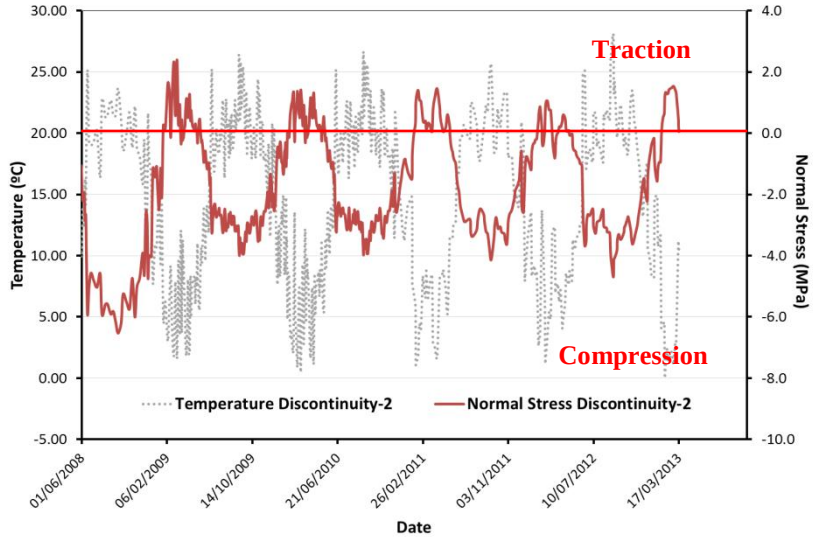

(a)

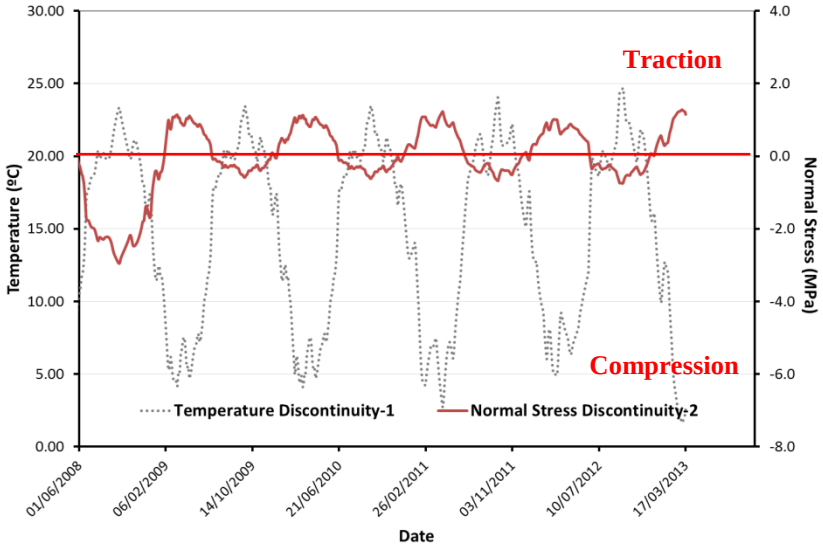

(b)

Figure 5-44. Normal stress computed; a) Jointmeter J-1; b) Jointmeter J-2

5.2 REFERENCES

Olivella, S; Gens, A; Carrera, J; Alonso, E. (1996). *Numerical Formulation for a Simulator (CODE_BRIGHT) for The Coupled Analysis of Saline Media.* Engineering Computations, Vol. 13, No 7, pp. 87-112.

Saaltink, M., Pereira, J.M. & Samat, S. 2012.. Atmospheric Boundary Conditions Module in *CODE_BRIGHT.*

Gens A., Carol I. & Alonso E.E.1990. A constitutive model for rock joints; formulation and numerical implementation. *Computers and Geotechnics*, 9:3–20.

Zandarin, M. T. 2010. Thermo-Hydro-Mechanical analysis of joints-A theoretical and experimental study. *PhD Thesis, Universitat Politècnica de Cataluna.*

CHAPTER 6

CONCLUSIONS AND FUTURE WORKS

6.1 CONCLUDING REMARKS

The case of the cliff at *La Roque Gageac* provides an excellent example of the coupled ground-atmosphere interaction in a geological structure, as the instrumentation system evidences a strong relationship between cycles of external temperature and of internal deformation.

Site investigation realized by the *Laboratoire Régional des Ponts et Chaussées* indicate that the rock cliff presents three levels of risk associated to different volume of materials; the superficial flaking, the residual beam within the cavern and large volume involved in decompression phenomena. It evidences also that the massif presents a low strength as the results of the high porosity of the rock and the presence of karstification cavities and several families of discontinuities.

Several numerical simulations of the response of the cliff have been realized to get insights into the cliff stability. They indicate that:

- The consideration of solar radiation in the model is crucial to capture the temperatures measured in the massif.

- The consideration of a thermo-mechanical coupling only provides results in good agreements with the measurements.

- Although the massif presents a strong heterogeneity, the assumption of a homogeneous material provides a good approximation of the response of the massif. However, the analysis of the response of the beam requires the modelling of the behaviour of the discontinuities that delimit it.

- In the part of the cliff above the cavity, the responses of the rock appear to essentially reversible.

- Irreversible deformation occurs at the two vertical discontinuities that bound the residual rock beam.

6.2 FUTURE DEVELOPMENTS

To obtain a quantitative assessment of risk associated to cliff, the present work requires to be completed along the following lines:

- Implementation of an elastoplastic model for the joint elements in order to model the irreversible displacement measured on the sides of the rock beam and relate it to temperature threshold.

- Realization of thermo-mechanical laboratory tests on the rock samples: measurement of thermal conductivity, coefficient of expansion, and strength at different temperatures.

- Modelling of the differential thermal expansion between the different minerals of the rock to assess the possibility of long-term damage temperature cycles.

- Modelling of flaking process by considering the rock weathering process induced by cycles of temperature and drying/wetting at low confining stress (Pineda *et al.* 2011) with the objective to assess the residual risk related the fall of small blocks.